

Navdeep Kaur Panesar

A Study of quiescent  
prominences using  
SDO and STEREO data



Universitätsverlag Göttingen



Navdeep Kaur Panesar

A study of quiescent prominences using SDO and STEREO data

This work is licensed under a [Creative Commons Attribution-ShareAlike 4.0 International License](https://creativecommons.org/licenses/by-sa/4.0/).



erschienen im Universitätsverlag Göttingen 2014

---

Navdeep Kaur Panesar

A study of quiescent prominences  
using SDO and STEREO data



Universitätsverlag Göttingen  
2014

## Bibliographische Information der Deutschen Nationalbibliothek

Die Deutsche Nationalbibliothek verzeichnet diese Publikation in der Deutschen Nationalbibliographie; detaillierte bibliographische Daten sind im Internet über <http://dnb.ddb.de> abrufbar

Dissertation for the award of the degree “Doctor rerum naturalium” (Dr.rer.nat.)  
of the Georg-August-Universität Göttingen within the doctoral program PROPHYS  
of the Georg-August University School of Science (GAUSS)

Thesis committee

Prof. Dr. Ansgar Reiners, Institut für Astrophysik, Georg August Universität Göttingen, Germany  
Dr. Davina Innes, Max-Planck-Institut für Sonnensystemforschung, Göttingen, Germany

Date of the oral examination: 19.12.2013

*Address of the Author*

e-mail: [panesar@mps.mpg.de](mailto:panesar@mps.mpg.de)  
[navdeep\\_panesar@yahoo.co.in](mailto:navdeep_panesar@yahoo.co.in)

This work is protected by German Intellectual Property Right Law.  
It is also available as an Open Access version through the publisher’s homepage and the Online Catalogue  
of the State and University Library of Goettingen (<http://www.sub.uni-goettingen.de>).  
The conditions of the license terms of the online version apply.

Set and layout: Navdeep Kaur Panesar

Cover: Franziska Lorenz

Cover picture: A huge solar tornado observed by the Solar Dynamic Observatory (SDO)  
on 25 September 2011 with surrounding coronal cavity.

© 2014 Universitätsverlag Göttingen  
<http://univerlag.uni-goettingen.de>  
ISBN: 978-3-86395-158-0

# **A Study of quiescent prominences using SDO and STEREO data**

Dissertation  
for the award of the degree

“Doctor rerum naturalium” (Dr.rer.nat.)

of the Georg-August-Universität Göttingen

within the doctoral program PROPHYS  
of the Georg-August University School of Science (GAUSS)

submitted by

**Navdeep Kaur Panesar**

from Ludhiana, India

Göttingen, 2013

### Thesis Committee

Prof. Dr. Ansgar Reiners

Institut für Astrophysik, Georg-August-Universität Göttingen, Germany

Dr. Davina Innes

Max-Planck-Institut für Sonnensystemforschung, Göttingen, Germany

### Members of the Examination Board

Reviewer: Prof. Dr. Ansgar Reiners

Institut für Astrophysik, Georg-August-Universität Göttingen, Germany

Second Reviewer: Prof. Dr. Manfred Schüssler

Max-Planck-Institut für Sonnensystemforschung, Göttingen, Germany

Further members of the Examination Board:

Prof. Dr. Ulrich R. Christensen

Max-Planck-Institut für Sonnensystemforschung, Göttingen, Germany

Prof. Dr. Stefan Dreizler

Institut für Astrophysik, Georg-August-Universität Göttingen, Germany

Prof. Dr. Joerg Buechner

Max-Planck-Institut für Sonnensystemforschung, Göttingen, Germany

Prof. Dr. Hardi Peter

Max-Planck-Institut für Sonnensystemforschung, Göttingen, Germany

Date of the oral examination: 19.12.2013



# Contents

<b>Abstract</b>	<b>5</b>
<b>1 Solar prominences</b>	<b>7</b>
1.1 The Sun . . . . .	7
1.1.1 What are Prominences? . . . . .	8
1.1.2 Morphological characteristics . . . . .	9
1.2 Magnetic structure of prominences . . . . .	13
1.2.1 Filament channels . . . . .	15
1.2.1.1 Coronal arcade . . . . .	16
1.2.2 Coronal/prominence cavities . . . . .	17
1.2.3 Stability and equilibrium . . . . .	18
1.2.3.1 Force free fields . . . . .	19
1.3 Magnetic solar cycle of the Sun . . . . .	19
1.3.1 Sunspots . . . . .	19
1.3.1.1 The behaviour of the sunspot bipoles . . . . .	19
1.3.2 Solar dynamo . . . . .	20
1.3.3 Flux emergence . . . . .	21
1.4 Prominence models . . . . .	23
1.5 Prominence eruption . . . . .	27
1.6 Outline of the thesis . . . . .	28
<b>2 Instruments and data analysis techniques</b>	<b>31</b>
2.1 The SDO . . . . .	31
2.1.1 SDO orbit . . . . .	33
2.1.2 SDO/AIA . . . . .	34
2.1.3 SDO/HMI . . . . .	35
2.2 The STEREO . . . . .	36
2.2.1 SECCHI/EUVI . . . . .	37
2.3 Data analysis techniques . . . . .	40
2.3.1 Background removal . . . . .	41
2.3.2 Feature identification . . . . .	42
2.3.2.1 SDO grid lines on the STEREO images . . . . .	44
2.3.2.2 Tie-pointing method . . . . .	44

<b>3</b>	<b>Structure and evolution of a polar crown prominence/filament system</b>	<b>47</b>
3.1	Introduction . . . . .	47
3.2	Observations and data analysis . . . . .	51
3.2.1	SDO/AIA data . . . . .	51
3.2.2	STEREO/EUVI data . . . . .	51
3.2.3	SDO/HMI and GONG observations . . . . .	51
3.3	Overview . . . . .	53
3.3.1	Structure of the filament channel . . . . .	53
3.3.2	Footpoints of the prominence . . . . .	56
3.3.3	Evolution on 14 February . . . . .	59
3.3.3.1	Eruption leading to cavity dimming . . . . .	60
3.3.3.2	Breaking of filament . . . . .	61
3.4	Flow patterns in the prominence . . . . .	61
3.5	Discussion . . . . .	65
<b>4</b>	<b>Activation of a tornado-like prominence</b>	<b>73</b>
4.1	Introduction . . . . .	73
4.2	Observations . . . . .	76
4.3	Overview . . . . .	78
4.3.1	The three flares . . . . .	78
4.4	Discussion . . . . .	84
4.4.1	Mathematical Illustration of the Hudson Effect . . . . .	87
<b>5</b>	<b>Thermal stratification of a prominence using DEM</b>	<b>89</b>
5.1	Introduction . . . . .	89
5.1.1	AIA response function . . . . .	93
5.2	Observations and Data analysis . . . . .	93
5.2.1	DEM parametrization . . . . .	96
5.3	Results and Discussion . . . . .	96
5.3.1	DEM for prominence-cavity system . . . . .	97
5.3.1.1	Peak temperature map of the prominence-system . . . . .	97
5.3.1.2	Peak emission measure of the prominence-system . . . . .	97
5.3.2	Comparison of the temperature maps with intensity images . . . . .	98
<b>6</b>	<b>Summary and outlook</b>	<b>107</b>
	<b>Bibliography</b>	<b>111</b>
	<b>Publications</b>	<b>131</b>
	<b>Acknowledgements</b>	<b>133</b>
	<b>Curriculum Vitae</b>	<b>135</b>

# Abstract

Solar prominences are spectacular features on the Sun. They have been investigated for many decades, but the structure and dynamics of prominences is still not fully understood. They are highly dynamic and relatively cool compared with the surrounding corona. On the solar limb, they appear as a huge sheet of plasma. They are known as filaments when observed as dark, thin ribbon-like structures on the solar disk. Prominences usually lie above the magnetic polarity inversion lines. They are mainly of two types: Active region prominences, which are found near the active regions, and quiescent prominences (QP), which are found between the diffused active region boundaries. QPs are more stable than the active region prominences. Polar crown prominences (PCP) are high latitude quiescent prominences. They often appear as chains of chromospheric plasma and thick pillars. Some theoretical models have been proposed to explain the magnetic structure and stability of prominences. High resolution observations are needed, however, for the better understanding of prominence structure and verifying theoretical models. In the beginning, they were mainly observed in  $H\alpha$  line at  $6563\text{\AA}$  but now prominences are more often observed in extreme ultra violet (EUV) wavelengths. This allows the researchers to study a broader range of prominence characteristics. With the launch of the Solar Dynamic Observatory (SDO), we have excellent high resolution images for the study of structure and dynamics of prominences.

This thesis mainly focuses on the study of quiescent prominences. The structure and flows of quiescent prominences have been investigated. For this purpose, SDO images with high spatial and temporal resolution have been used. The Solar Terrestrial Relations Observatory (STEREO) data has been combined with the SDO data to infer the three-dimensional geometry of prominences when the spacecraft were roughly 90 degrees to the Earth-Sun line. This separation angle is extremely useful to study prominences which are observed by SDO on limb and simultaneously seen as filaments on the solar disk from the STEREO-Ahead spacecraft. Two different types of quiescent prominences are investigated; one polar crown prominence and the other rather active, tornado-like quiescent prominence.

The structure and evolution of the PCP is investigated in detail. It is found that the prominence pillars are separated by many tens of Mm. They are connected with each other by dynamic bridges of cold and hot plasma, that can be seen in  $304/171\text{\AA}$  images. The SDO images show strong upflows in the prominence pillars and indicate the presence of a coronal cavity. The STEREO-A disk images show a region of reduced emission in the filament channel that coincides the coronal cavity. The STEREO-A timeseries images show no variation in the region of reduced emission which may be an additional signature of the cavity on the disk. Several small-scale brightenings in the filament channel are observed. The arrival of diffused active region positive flux plays an important role in the

filament channel evolution. The merging of diffused positive flux in the filament chain results in several small-scale brightenings which inject plasma upwards. The observed scenario is in agreement with the flux linkage model of PCP. Persistent flows are observed in the prominence pillars with an average velocity of  $15.5 \text{ km s}^{-1}$ , which is roughly the estimated sound speed in the prominence.

An interesting prominence tornado was observed by SDO on 25 September 2011. The triggering mechanism of the tornado prominence is investigated. For this purpose, the SDO and STEREO-A data were used. With the help of the two-views of the prominence, the event was studied in detail. An active region was observed near the prominence-cavity system which produced multiple flares. The flares were suspected to influence the prominence-cavity system. It was noticed that there were three M-class flares and they were associated with EUV waves. The SDO images showed strong oscillations in the prominence after the first flare. An arm-like extension of prominence plasma was observed after the second flare. The third flare was the strongest one. It triggered the tornado and also produced a strong EUV wavefront that swept over the filament channel. A simple model is suggested in which the active region field contracts after the flare due to the loss of free magnetic energy, resulting in a decrease of magnetic pressure at the flare site. Subsequently, the neighbouring prominence cavity expanded towards the active region due to its higher magnetic pressure than the active region. Thus, the prominence grew in height and started to rotate faster, appearing as a tornado at the top.

In addition, the thermal structure of the tornado-like prominence and neighbouring active region was investigated by analysing emission in six of the seven EUV channels from the SDO. As expected, the core of the active region shows the highest temperature of  $\sim 8 - 10 \text{ MK}$ . The cavity is slightly cooler than the active region corona.

Thus, the detailed structure and dynamics of two quiescent prominences have been studied in the thesis. These observational investigations led to our understanding in some aspects of quiescent prominences, which could be useful constraint for theoretical prominence models.

# 1 Solar prominences

## 1.1 The Sun

The Sun is the nearest star to our Earth. It is a G2V star in our galaxy. It is situated on the main sequence of the Hertzsprung-Russell (HR) diagram (Fig. 1.1) which suggests a surface temperature of  $\sim 5500$  K (Phillips 1992). The Sun has luminosity  $L_{\odot} = 3.85 \times 10^{33}$  ergs $^{-1}$ , mass  $M_{\odot} = 1.99 \times 10^{33}$  g, and radius  $R_{\odot} = 696$  Mm. The outer solar atmosphere can be divided into three main layers - photosphere, chromosphere and corona. The internal structure of the Sun is divided into three main layers - the core is the central part, then there is the radiation zone and above that there is the convective zone, which is just below the photosphere. The energy is generated in the core which results in a temperature of 15 MK. From the core, the energy is transported to the visible surface of the Sun - the photosphere, by radiation and convection. Above the photosphere, the temperature decreases slightly to a thin temperature minimum layer. The temperature then increases in the chromosphere and then further increases and reaches up to a few million Kelvin ( $\sim 5$  MK) in the corona (see Fig. 1.2, for more details see following papers: Aschwanden (2004) and Gary et al. (2007)). This drastic change in the temperature occurs above 1000 km from the photosphere. It is still an interesting puzzle in solar physics why the temperature of the solar corona is a million Kelvin higher than the solar surface.

The solar corona is highly inhomogeneous. The electron density in the solar corona is much lower than in the photosphere (Fig. 1.2). It is in the range of  $\approx 10^9$  cm $^{-3}$  at the base of the corona above quiet regions (Aschwanden 2004). An important parameter, plasma- $\beta$ , is low in most parts of the corona. The plasma  $\beta$  parameter is defined as the ratio of the gas pressure ( $P_{gas}$ ) to the magnetic pressure ( $P_{mag}$ ). The value of plasma- $\beta$  is less than unity in the corona which means that the magnetic pressure dominates over the gas pressure (Gary 2001).

Plasma- $\beta$  is given as:

$$\beta = \frac{P_{gas}}{P_{mag}} = \frac{p}{(B^2/8\pi)}, \quad (1.1)$$

where  $P_{gas}$  is the gas pressure, for simplicity and consistency we denote it as  $p$ ,  $B$  is the magnetic field strength. The plasma- $\beta$  parameter strongly depends upon the magnetic field at different heights in the corona. In absence of direct measurements of coronal magnetic field, it can be estimated with the help of the extrapolation of the photospheric magnetic field (Wiegelmann and Sakurai 2012) and remote sensing techniques (Lin et al. 2004, Tomczyk et al. 2008). These measurements indicate a magnetic field of 10 Gauss in the quiet Sun at the height of 70 Mm, whereas the gas pressure ( $2\pi nkT$ ) is 0.3 dyne cm $^{-2}$  (approximate values  $T = 1.1$  MK,  $n_e = 1 \times 10^9$  cm $^{-3}$ ). With these values we can estimate

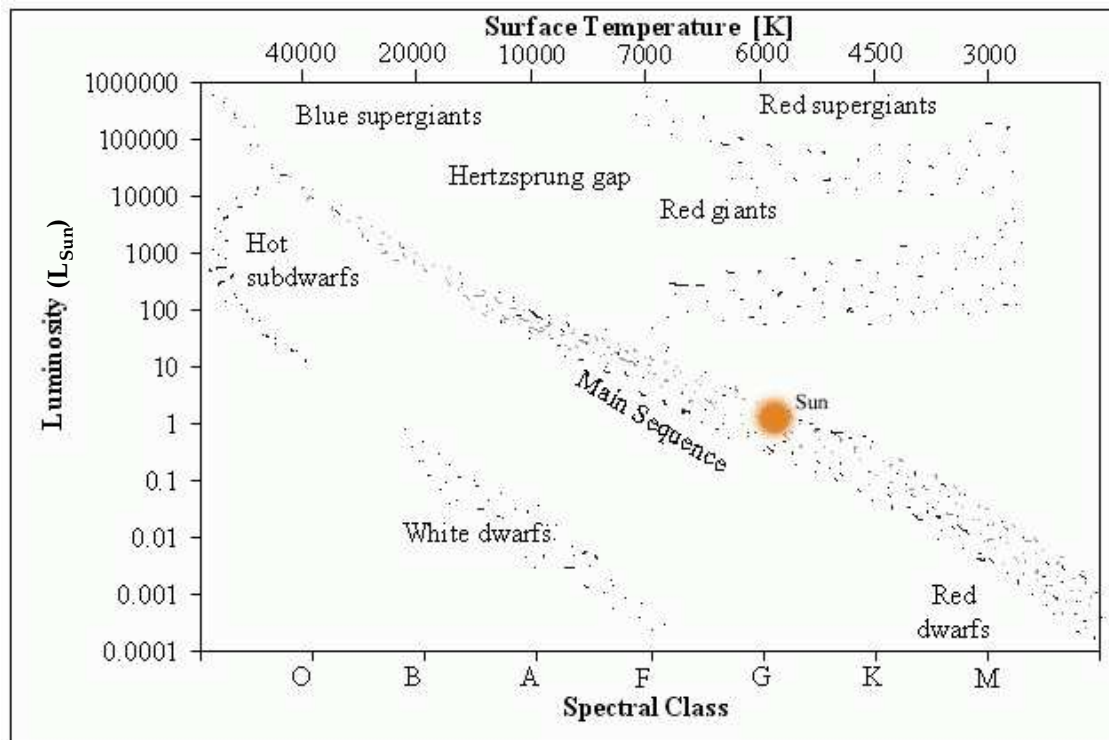


Figure 1.1: The Hertzsprung-Russell diagram relates the brightness of a star to its temperature. The Sun is a G2 spectral type star located in the main sequence. Courtesy - <http://www.diracdelta.co.uk/science/source/y/e/yellow>

$\beta \approx 0.07$ . This small value of  $\beta (\ll 1)$ , implies that the corona is magnetically dominated.

### 1.1.1 What are Prominences?

Prominences are fascinating, large-scale 'arch-shaped' coronal magnetic structures on the Sun. They were first observed on the solar limb during the total solar eclipses and recognized in terms of 'lunar clouds' or 'hole in the moon'. Secchi (1872) reported the prominences as 'a burning hole' in it. He was the first who stated the phenomenon of prominences and also divided the prominences into sub-classes - active and quiescent prominences. In recent years, prominences have been an interesting topic of research in solar physics. They are divided into many subgroups, according to their observed properties (Pettit 1919, 1932, 1943) e.g. active region prominences (ARP), intermediate prominences, quiescent prominences (QP), polar crown prominences (PCP) and tornado-like prominences.

Prominences are relatively cool and dense material, reaching up to the height of several hundreds of kilometers in the hotter solar corona (Hirayama 1985, Tandberg-Hanssen 1995, Mackay et al. 2010, Labrosse et al. 2010). They are known as filaments when observed as a dark feature against the bright solar disk (Zirin 1988) (see Fig. 1.4, top panel, filaments (QP, PCP) are indicated with the white arrows on solar disk). Filaments have long been studied as absorption features on the solar disk with spectroheliograms (Hale and Ellerman 1903, Deslandres 1909). They are known as prominences when they are

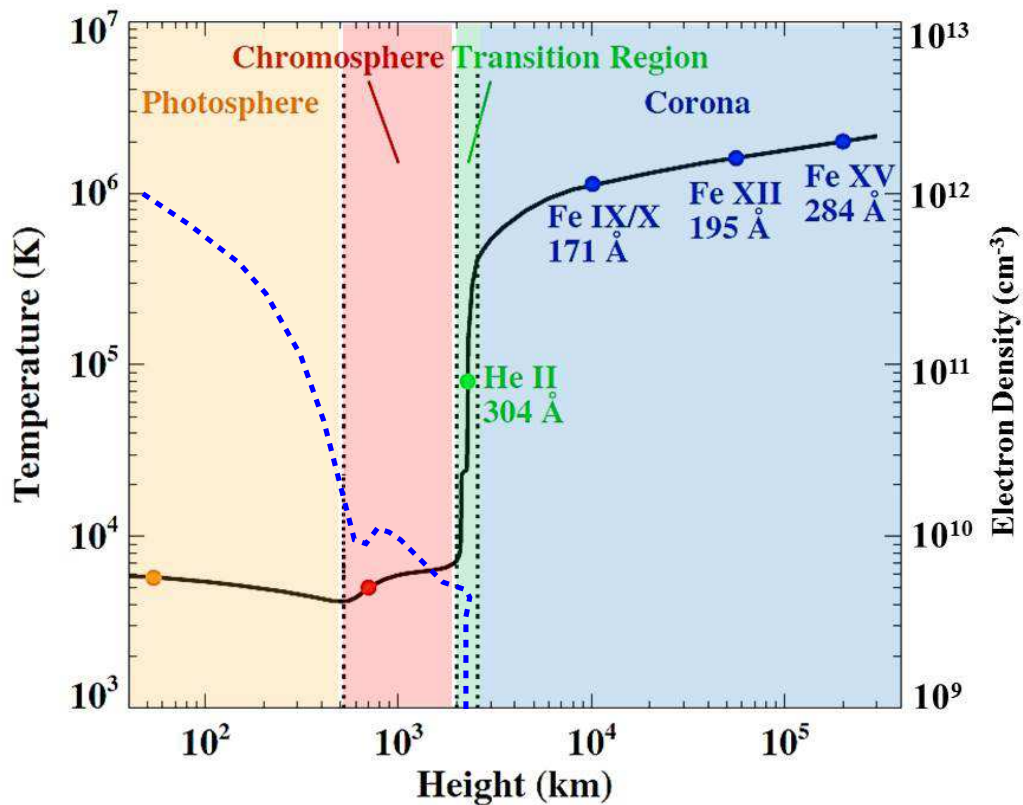


Figure 1.2: Variation of temperature and density with height from photosphere to corona. Image is taken from Yang et al. (2009).

seen above the solar limb, as shown in Fig. 1.3, where the prominences (ARP, QP) are pointed with an arrow. One should notice that both - the prominence and the filaments are the same phenomena, but their different names are due to their different observed positions and properties. Even though prominences are embedded in the hotter corona, their density is a hundred times larger and temperature is a hundred times lower than the surrounding coronal density and temperature values respectively. An unsolved question is how the denser prominence material is sustained in the low density corona.

### 1.1.2 Morphological characteristics

Prominences are divided into several sub groups as also mentioned above. These subdivisions depend upon their observed properties. In the following, we describe the different types of prominences:

- *Active Region Prominences:* Active region prominences (ARP) are mainly found in and around the active regions (sunspots) of the Sun. They are relatively more unstable, are shorter in length ( $\sim 10$  Mm), and high magnetic field strength (20 to 70 G) than the quiescent prominences. They are very dynamic, mostly associated with flares and Coronal mass ejections (CME). They are also known as the precursors of quiescent prominences (Tandberg-Hanssen 1995). Formation of the active

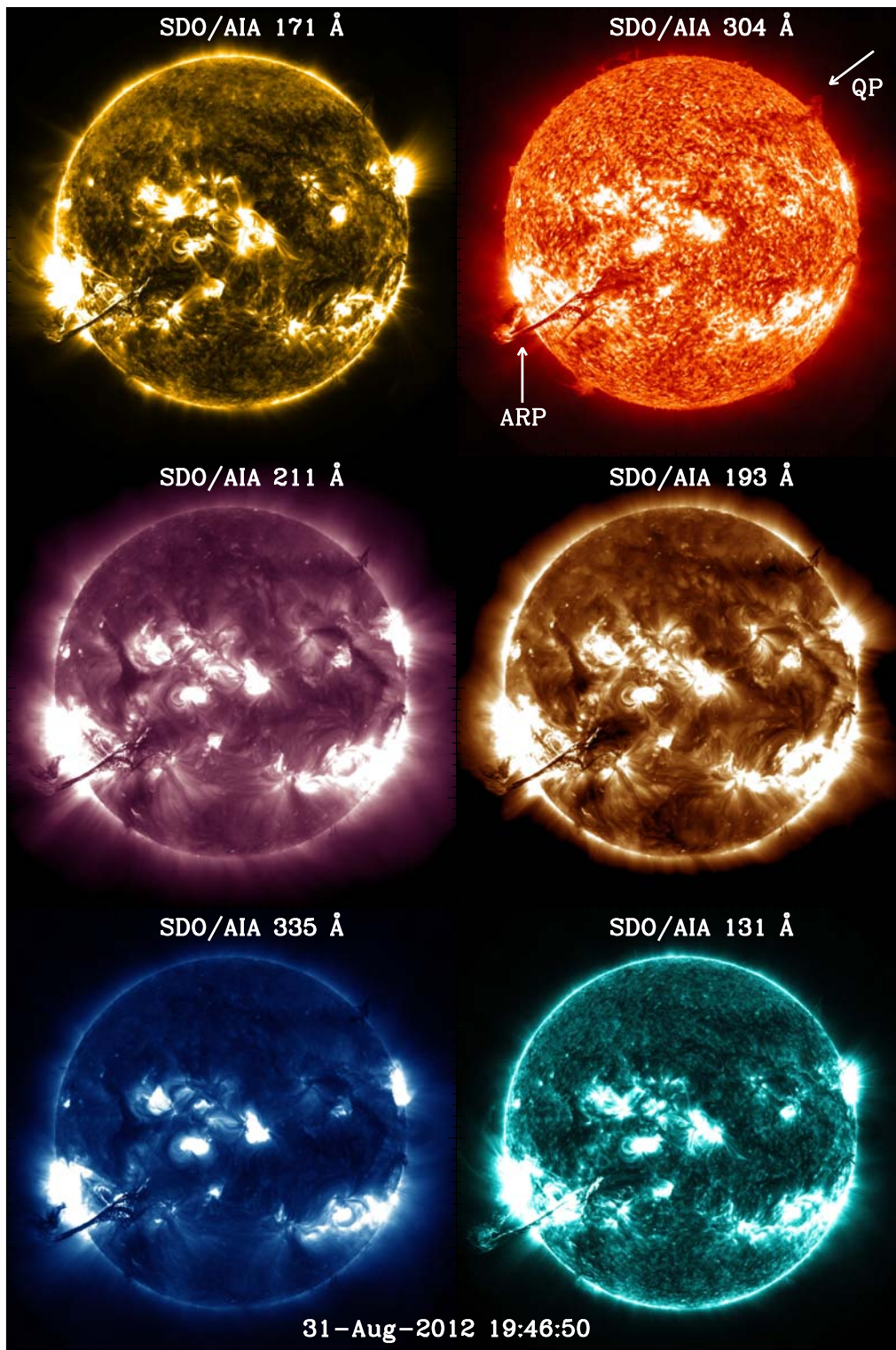


Figure 1.3: Active region prominence and quiescent prominence (ARP, QP) observed by SDO on 31-Aug-2012 in six different AIA filters. ARP and QP are indicated by arrows at SE and NW solar limb.



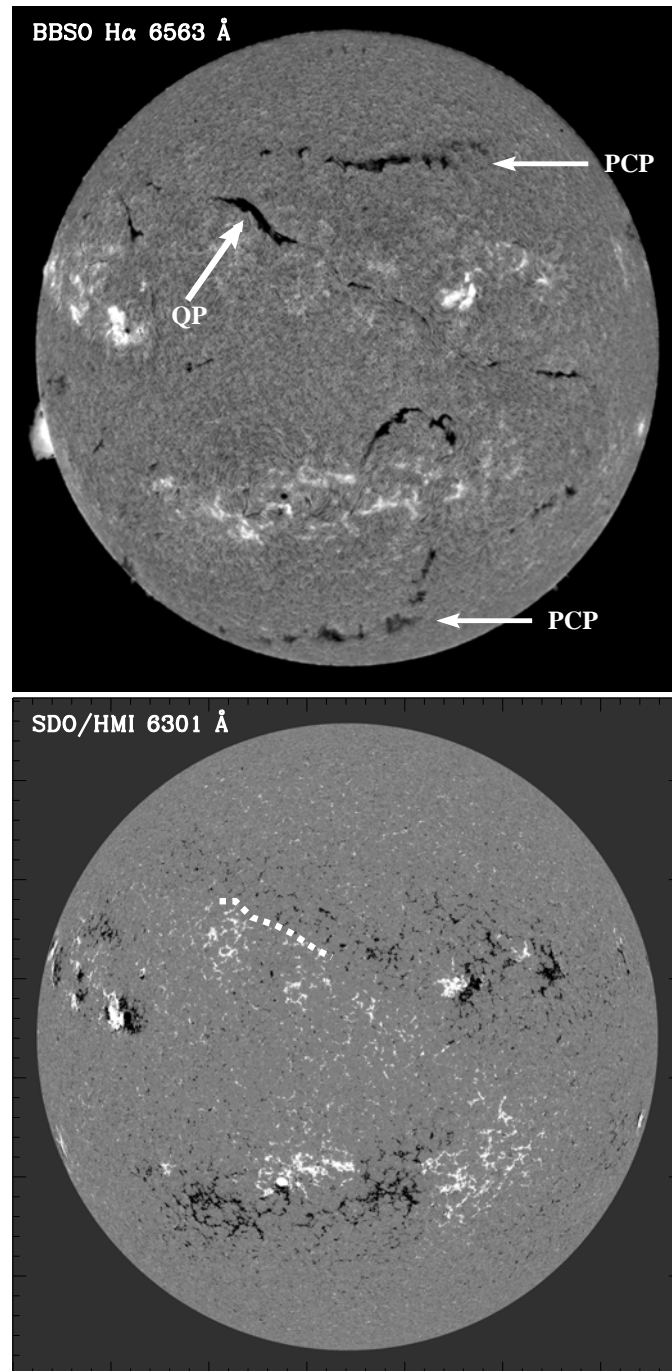


Figure 1.4: Top panel - A full disc image of the Sun in  $H\alpha$  from Big Bear Solar Observatory (BBSO). Arrows point to the quiescent filament/prominence (QP) and polar crown prominences (PCP) on the solar disk. Bottom panel shows the SDO/HMI photospheric magnetogram, in which white and black colour patches represent the positive and negative magnetic polarities. The filament is located between the two different magnetic polarities. The white dashed line roughly outlines the position of polarity inversion line (PIL) of QP. Both images are taken on 27 August 2012 at the same time - 16:50 UT.



Figure 1.5: An image of a well known huge vertical sheet-like quiescent prominence, which was observed by the BBSO in  $H\alpha$  filter in 1970.

region prominences is not clearly understood. The numerical simulations suggest that when a flux rope has fully emerged, reconnection will occur which may reconfigure the emerged flux rope. During this process the reconnection will inject the prominence plasma into the corona (Manchester et al. 2004, Magara 2006, Archontis and Török 2008, Fan 2009). Fig. 1.3 shows a huge active region prominence on the SE solar limb in different SDO/AIA filters.

- *Quiescent Prominences:* The quiescent prominences (QP) are found in the quiet Sun, away from the active regions, between the diffused active region flux (Zirker et al. 1997), as shown in Fig. 1.3 and marked with an arrow (QP). Another example of quiescent filament is shown in Fig. 1.4 in  $H\alpha$  along with the Solar Dynamic Observatory/Helioseismic and Magnetic Imager (SDO/HMI) image which shows the underlying photospheric magnetic flux. It has been reported that the quiescent prominences are formed in the multiple bipolar magnetic interaction regions (Mackay et al. 2008b). Therefore, the number of quiescent prominences depends upon the solar cycle, more number of quiescent prominences are seen around the solar maximum and during the declining phase of the solar activity. They are long lived and can live from several days to months (Kuperus and Tandberg-Hanssen 1967). They are enormous vertical sheet-like structures above the solar surface (as shown in Fig. 1.5), having a length of 60-600 Mm and height of 15-100 Mm (Tandberg-Hanssen 1995). Some other important parameters of the quiescent prominences are shown in Table. 1.1.
- *Polar Crown Prominences:* Polar crown prominences (PCP) can be seen in the northern and southern hemispheres of the Sun in Fig. 1.4. Polar crown prominences are the sub-class of quiescent prominences. They occur in the quiet Sun regions during solar minimum and are found more towards the polar regions as the activity increases (Waldmeier 1957, 1973, Mouradian and Soru-Escout 1994, Minarovjech et al. 1998b, Ambrož and Schroll 2002). They are commonly seen

between the boundary of dispersed active region flux and the coronal hole. Polar crown prominences are composed of multiple threads, which appear as pillars with typical lengths of 3-20 Mm (Lin et al. 2003b, Heinzel and Anzer 2006, Gunár et al. 2007, 2008, Berger et al. 2008). They mostly appear as a crown on the poles, sometimes as a complete ring. The dynamics of a polar crown prominence is discussed in detail in Chapter. 3 (Panesar et al. 2014a).

- *Intermediate Prominences*: Another class is the intermediate prominence. They can be seen between the quiet region and active region or share properties of both (active and quiescent) types of prominences (Engvold 1998). Sometimes they may also form between multiple bipolar regions similar to quiescent prominences.
- *Tornado Prominences*: Another interesting type of prominence is the tornado-like prominence which appears as vertical spiral structure on the solar limb and reaches up to a height of several thousands of km in the corona (an image is shown in Chapter. 4). Tornado-like activity was first shown and presented by Pettit (1919, 1925). He suggested that the tornadoes appear as either tightly wound flux ropes or vertical open spirals (Pettit 1932, 1941, 1943, 1946, 1950). Generally the width and height of tornado-like prominences are from 5 to 22 Mm and from 25 to 100 Mm respectively (Pettit 1943, Li et al. 2012). Tornado-like prominences have always been very interesting phenomena on the Sun because of their observed noticeable helical magnetic structures and dynamics (Panesar et al. 2013, 2014b). Nowadays they are frequently observed because of the availability of both temporal and spatial high-resolution observations from Solar Dynamic Observatory (SDO). We have also studied a quiescent tornado-like prominence in this thesis work, which is presented in Chapter. 4.

*Active-type Prominences*: Eruptive, sprays, loops and surges are active prominences (Severny 1950, Severny and Khoklova 1953, de Jager 1959, Zirin 1966). They are different than the active region prominences because they are mainly related to the sunspots. They are quite eruptive and show the fast changes (Tandberg-Hanssen 1995). They are formed as a result of flux emergence (Lites and Low 1997, Okamoto et al. 2009), and easily erupt (within a few minutes to hours).

## 1.2 Magnetic structure of prominences

Prominences are found in the chromosphere or in the lower corona. They are located above the magnetic neutral line/polarity inversion line (PIL) of the photospheric magnetic field (Babcock and Babcock 1955, Zirker 1989). The polarity inversion line is the line which separates the two opposite magnetic polarities (Martin 1973b). In Fig. 1.4, a PIL is roughly highlighted by a white dashed line between the negative and positive photospheric magnetic flux, associated with H $\alpha$  filament shown in the upper panel of Fig. 1.4 (indicated with an arrow).

The fine structures of filaments are known as threads and they can be clearly visible in high resolution observations, one example is shown in Fig. 1.6. Engvold (1976) studied the filaments structure in H $\alpha$  and observed that they are made up of fine threads and knots.

Table 1.1: Physical parameters of quiescent prominences. Values are adapted from Tandberg-Hanssen (1995), Patsourakos and Vial (2002), Aschwanden (2004), Lin et al. (2005a,b)

Parameter	Values
Temperature	5,000 - 15,000 K
Number density	$10^{10}$ - $10^{12}$ cm <sup>-3</sup>
Magnetic field strength	4 - 20 G
Gas pressure	0.6 dyne cm <sup>-2</sup>
Prominence length	60 - 600 Mm
Prominence height	15 - 100 Mm
Prominence width	4 - 30 Mm
Fine structure length	3 - 15 Mm
Fine structure width	0.1 - 0.5 Mm

They have a lifetime of more than one hour. Lin et al. (2008a) found that all filaments observed in high resolution images are made up of fine threads. The filament threads are aligned along the filament spine with a width of 200 km (Lin et al. 2005b,a, 2007, 2008b, 2009).

The short threads have also been observed in H $\alpha$  images of quiescent prominences (Malherbe 1989, Martin 1998a, Pécseli and Engvold 2000). The vertical threads in the quiescent prominences are reported by Chae et al. (2008), Berger et al. (2008), whereas the active region prominences are made up of relatively longer threads (Fig. 1.6).

The filament body mainly consists of 3 structural components : a spine, barbs and two extreme ends (Mackay et al. 2010).

- *Spine*: The main long and horizontal body of the filament is known as a spine. It runs along the top of the filament. Therefore, it lies above the magnetic polarity inversion line (see Fig. 1.7, a spine is marked by an arrow).
- *Barbs*: Barbs protrude from the sides of the spine of the filament, either on the right or the left side and they make an acute angle with respect to the filament (Martin et al. 1992). They are clearly seen in high resolution images (e.g. see Fig. 1.7). When the prominence is viewed close to the limb, barbs are seen to extend down from the spine towards the photosphere (Lin et al. 2008a). They never extend in the perpendicular direction to the spine but always make some angle. They are supposed to provide support to the filament/prominence system (Engvold 1998). Sometimes in the polar crown prominences, the spine is not clearly visible, only the barbs are seen as vertical dense pillars and such filaments are known as feet-dominated filaments (Schmieder et al. 2010, Dudík et al. 2012).

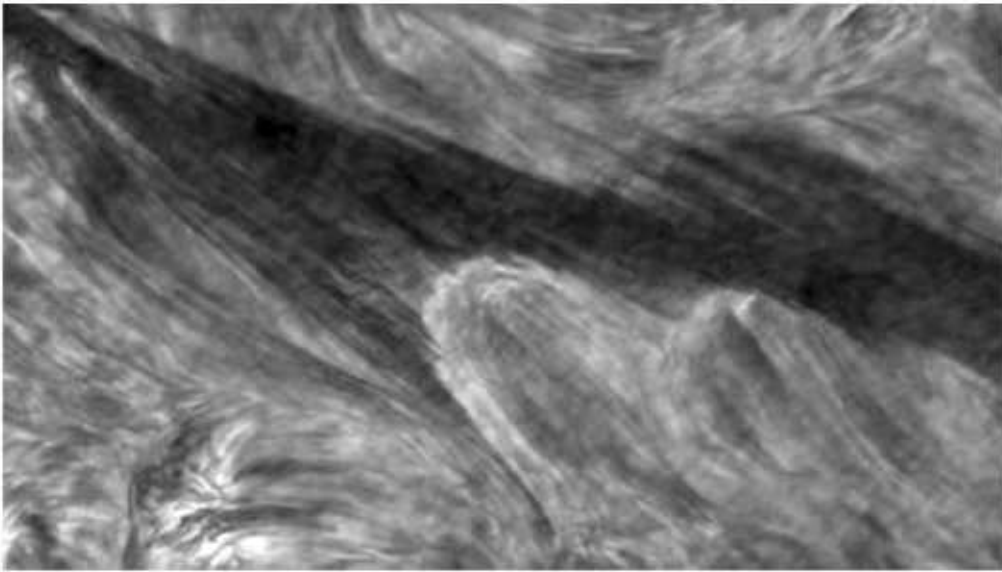


Figure 1.6: High resolution  $H\alpha$  image of the filament thread on 26 August 2003 observed by the 1-meter Swedish Solar Telescope. Image is taken from Lin et al. (2005b).

- *Extreme ends*: The beginning and end points of the filaments are known as two extreme ends. All these structural parts of the filaments are composed of fine threads which are easily observed in the quiescent prominences.

In Fig. 1.7, we can see that some barbs extend to the left side and other's are extending to the right side. This property of the barbs is known as chirality of the filaments. Based on the direction of the barbs, filaments can be classified as right bearing or left bearing. For example, the barbs which are right bearing, are classified as dextral filaments and the left bearing are sinistral barbs (Martin et al. 1994, Priest et al. 1996, McAllister et al. 2002, Schmieder et al. 2004). Martin et al. (1994), argue that the barbs are connected to the parasitic (main polarity) or minority polarity region (Martin et al. 1994, Martin 2003). Day to day movement of the barbs according to the changes in the parasitic polarity are showed by Aulanier and Demoulin (1998), Wang (1999, 2001), Lin et al. (2005a), Chae et al. (2005). Fig. 1.8 shows a schematic diagram of dextral and sinistral filaments. In the sketch, if we go from filament axis to barbs through an acute angle and the direction is clockwise, then the chirality of the filament is dextral and if it is in counter clockwise direction then it is known as sinistral chirality.

### 1.2.1 Filament channels

To understand the magnetic structure of the filaments and filament formation, it is important to discuss first about the filament channel because the filaments always form in filament channels (Gaizauskas et al. 1997). The filament channel is a region in which chromospheric fibrils are aligned along the PIL (Martres et al. 1966, Martin 1998a). The fibrils are the dark regions seen to be associated with the ends of a plage or plagette (Howard and Harvey 1964), for more details on fibrils see papers by Foukal (1971b,a). Gaizauskas (1998) was the first who discussed the formation of filaments in the filament

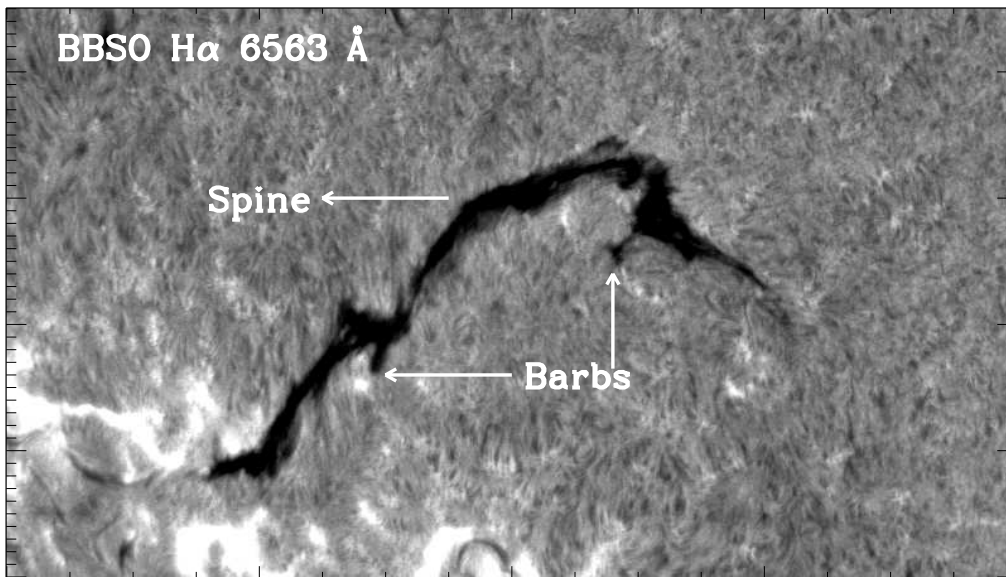


Figure 1.7: A filament observed by the BBSO in  $H\alpha$  filter on 04 August 2012 at 16:41:34. A spine and barbs are indicated by arrows.

channel. The filament channels form between the newly emerged active region flux and decaying active region flux. When the horizontal field of emerging flux region comes into contact with the decaying active region flux, a non potential field between both regions creates a filament channel. Gaizauskas (1998) also reported that the filament channel forms a few days prior to the filament formation. A filament channel is fully developed and ready to form a filament when there is no chromospheric fibril crossing the PIL (Martin 2003). Recent observations by Wang and Muglach (2007) show that initially the fibrils are normal to the PIL, but before the formation of the filament channel, they align along the PIL in opposite directions. It is not essential that every filament channel contains filaments or every PIL develops a filament channel. One of the necessary conditions for filament formation is the flux convergence and flux cancellation near the polarity inversion line, discussed in detail in Section. 1.4. Such type of scenario for the filament formation is shown by Gaizauskas (2002). Another important condition is magnetic shear in field lines between the bipolar regions as shown in Fig. 1.14. Field lines become non-potential due to the shear or surface motion towards the PIL leading to a suitable environment for the filament formation (Mackay and Gaizauskas 2003). Filaments appear only when there is a sufficient mass deposited in the filament channel.

### 1.2.1.1 Coronal arcade

Every filament has a coronal arcade. Coronal arcade is simply the magnetic field lines above the filaments where the footpoints are anchored in the opposite polarity of photospheric magnetic fields. It can be visible above prominences during the total solar eclipses (Martin 1998b). The coronal arcade is important for stability of the cold prominence plasma in the prominence/filament system (Hudson 2000, Gibson and Fan 2006, Gibson et al. 2010). Usually there is a dark and low density coronal region between the prominence and coronal arcade (Waldmeier 1970), known as coronal cavity (see Section 1.2.2).

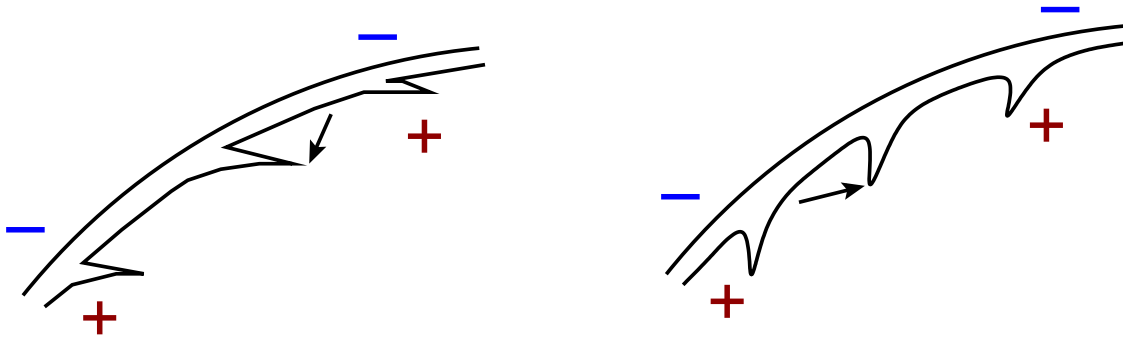


Figure 1.8: A sketch of the two different possible orientation of filaments. Left panel: shows dextral filament, arrow points clockwise direction via acute angle from filament axis to the barbs. Right panel: shows sinistral filament, arrow points counter clockwise direction via acute angle from filament axis to the barbs. Sketch is adapted from Martin (1998b).

The arcade is potential and surrounds both the prominence and cavity system (Low 1994, Low and Hundhausen 1995).

### 1.2.2 Coronal/prominence cavities

Prominences are often seen to be associated with coronal cavities (Tandberg-Hanssen 1995, Hudson et al. 1999b, Habbal et al. 2010, Schmit and Gibson 2011). Cavities are the upper coronal parts of filament channels, observed in white light, soft X-rays and EUV images (Gibson et al. 2006). They appear to be darker than the surrounding corona and extend larger in height than the prominences (Saito and Tandberg-Hanssen 1973). The cavities are situated at the base of the coronal helmet streamers (Low 1996, Engvold 1998). The temperature of cavities is comparable to the coronal temperature (Kucera et al. 2012) and the measured densities of the cavities are slightly less than half the density of the surrounding streamer (Fuller and Gibson 2009). It has been reported that the cavities overlie the PIL, with or without filaments (Vaiana et al. 1973, McIntosh et al. 1976, Serio et al. 1978).

Above quiescent prominences, cavities are long lived. Their structure changes slowly with time and sometimes they partly erupt with CMEs (Maricic et al. 2004, Vrsnak et al. 2004, Gibson and Fan 2006, Su et al. 2006, Liu et al. 2007, Tripathi et al. 2007, 2009). Polar crown prominence cavities are the most stable ones. Gibson et al. (2006) found that the polar crown prominence cavities last for several days and months (up to 8 solar rotations). They are not always visible throughout their lifetime because the visibility of cavities depends upon the orientation of the filament channel and obscuring features (e.g. AR loops) along the line-of-sight.

Coronal cavities give the clue that the filament channel is a part of a large magnetic structure, which may extend to the heights of several hundreds of km above the quiescent prominence. Fig. 1.9 is the STEREO-B 195 Å EUV image of a coronal cavity that is above a polar crown prominence: the dark and dim region of cavity is shown with the arrows.

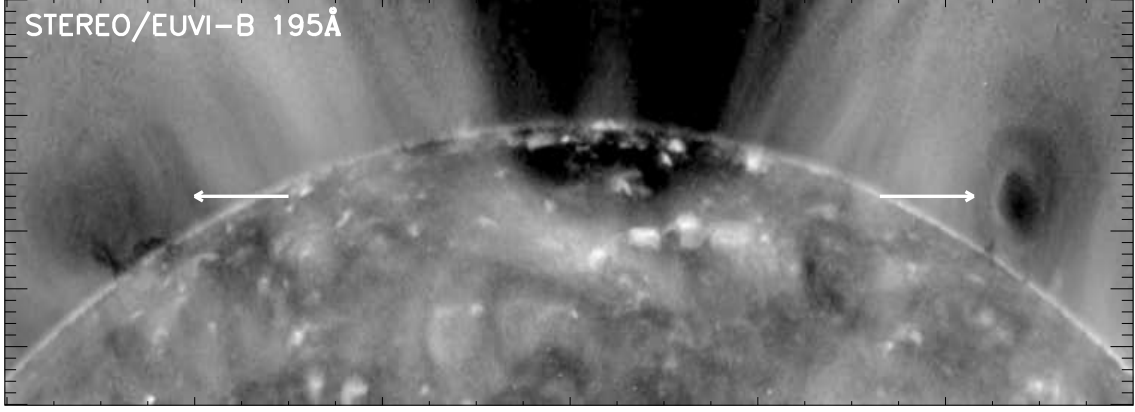


Figure 1.9: Coronal cavities, observed by the STEREO-Behind in 195Å filter on NE and NW solar limb, taken on 06-February-2011 at 19:23:36 UT. Both cavities are indicated by arrows.

### 1.2.3 Stability and equilibrium

Dense prominence plasma requires to be stabilized against the gravitational force. The equilibrium structure inside the prominence plasma was first discussed by Kippenhahn and Schlüter (1957). They explained the stability by magnetohydrostatic equilibrium equation:

$$\mathbf{j} \times \mathbf{B} - \nabla p + \rho \mathbf{g} = 0, \quad (1.2)$$

which indicates an equilibrium between the Lorentz force ( $\mathbf{j} \times \mathbf{B}$ ), the gas pressure gradient  $\nabla p$  and the gravitational force  $\rho \mathbf{g}$ . Where  $\rho$  is the density and  $\mathbf{g}$  is gravity which is towards the center of the Sun. The electric current density  $\mathbf{j}$  can be defined as:

$$\mathbf{j} = \frac{1}{4\pi}(\nabla \times \mathbf{B}), \quad (1.3)$$

$\mathbf{B}$  is the magnetic field, We can rewrite Equation 1.2 by inserting Equation 1.3 into 1.2:

$$(\nabla \times \mathbf{B}) \times \frac{\mathbf{B}}{4\pi} - \nabla p + \rho \mathbf{g} = 0 \quad (1.4)$$

where the first term, the Lorentz force ( $\mathbf{F}$ ) can be split into two terms (Priest 1982) also see (Tiwari 2012)

$$\mathbf{F} = \frac{(\mathbf{B} \cdot \nabla)\mathbf{B}}{4\pi} - \frac{\nabla(\mathbf{B} \cdot \mathbf{B})}{8\pi}. \quad (1.5)$$

In equation 1.5, the first term represents the magnetic tension force. This is the force which appears when the magnetic field lines are curved. This magnetic tension force supports the prominence weight against the gravity (Priest et al. 1989, Cartledge et al. 1996, Cartledge and Titov 1996). It depends on the curvature of the field lines, the smaller the radius of curvature, the stronger will be the tension force (Hillier and van Ballegooijen 2013). The second term represents the gradient in magnetic pressure, i.e. the force due to the magnetic pressure.



### 1.2.3.1 Force free fields

Outside prominences, where gravity can be neglected and magnetic pressure dominates over gas pressure e.g. in the solar corona, the field is known as force-free. It follows the magneto-static condition i.e. the Lorentz force is zero (Lüst and Schlüter 1954, Chandrasekhar and Kendall 1957, Chandrasekhar 1961, Jette 1970, Parker 1979c, Low 1982, Aschwanden 2004),

$$\mathbf{j} \times \mathbf{B} = 0. \quad (1.6)$$

Alternatively, we can also write:

$$(\nabla \times \mathbf{B}) \times \mathbf{B} = 0. \quad (1.7)$$

This will lead Equation 1.5 to zero. Thus, in that case the magnetic tension force and gradient of magnetic pressure should balance each other. The corona is generally force-free because the gas pressure and gravity terms are ignorable (Gold 1964b,a) and therefore Equation 1.7 is satisfied from Equation 1.4. The above Equation 1.6 also means that either the current is zero (potential field) or current and magnetic field are parallel to each other in the force-free condition.

## 1.3 Magnetic solar cycle of the Sun

The Sun's magnetic field is an important property of the Sun. There is an 11 year solar activity cycle. It was first discovered by Schwabe (1844). The solar activity can be traced from the variable features on the Sun e.g: sunspots, prominences, in addition to the number of flares (Zirker et al. 1997). In this section, we will discuss about the solar magnetic cycle and related prominence activity.

### 1.3.1 Sunspots

Sunspots play a major role in the manifestation of solar activity. From the sunspot number, we can see how active the Sun is (for more details see review by Solanki (2003) and papers by Parker (1979b,a)). The Sun has a well-known 11 year sunspot cycle. In the beginning of the solar cycle, sunspots emerge at a higher latitude and as the cycle progresses, the emergence regions migrate towards the equator. This creates a butterfly-shaped pattern every 11 years, as shown in Fig. 1.10. Shimojo et al. (2006) found that the variation in the prominence activity is related to the sunspot activity during a solar cycle.

#### 1.3.1.1 The behaviour of the sunspot bipoles

Sunspots usually appear on the solar surface in the form of bipolar groups. Bipolar sunspot pairs make a small tilt angle with respect to the equator. In the beginning of the solar cycle, more tilt is present in the sunspots observed at the higher latitudes. As the emergence sites move towards the equator tilt decrease between them. This behaviour of bipoles is known as Joy's law (Hale et al. 1919).

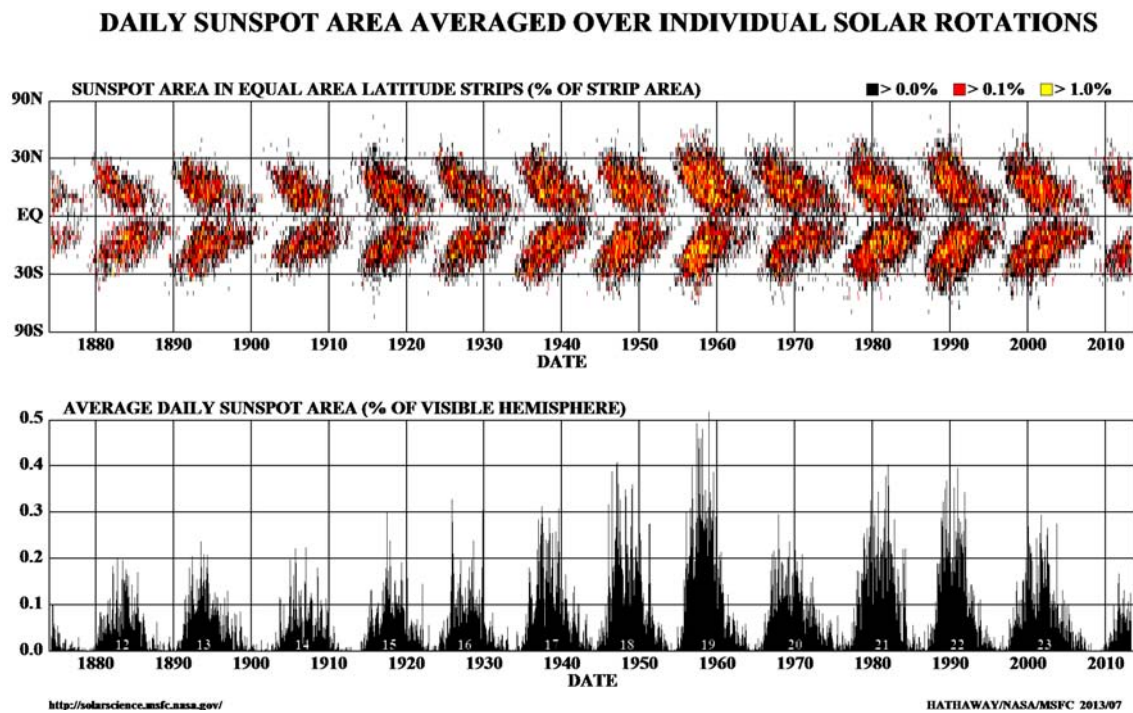


Figure 1.10: Top panel shows the Butterfly diagram and bottom panel shows the average daily sunspot area. Credit - D. Hathaway (<http://solarscience.msfc.nasa.gov>).

Hale and Nicholson (1925) observed that the leader is usually one polarity in one hemisphere whereas the leader of the other hemisphere is the opposite polarity. The leader sunspot is always nearer to the equator and it has the same polarity as the polar region of the respective hemisphere. The magnetic polarity of leaders/followers remains the same for one solar cycle. In the next solar cycle, the polarity order changes its sign. This is known as Hale's polarity law. The polarity comes to its original pattern after two solar cycles, which is known as the 22-year magnetic cycle of the Sun. This behaviour of solar magnetic field was first explained by Parker (1955b) and Babcock (1961) and further by Simon and Leighton (1964), Leighton (1969).

### 1.3.2 Solar dynamo

Parker (1955b) was the first to describe the solar dynamo process. Fig. 1.11 shows how the magnetic field is driven in the Sun. Fig. 1.11a,b shows that the poloidal magnetic field gets sheared at the bottom of the convective zone and the toroidal field is produced (Parker 1955a). This is due to the differential rotation, the rotation rate is faster at the equator and slower at the higher latitudes of the Sun. The toroidal magnetic field gets amplified and rises up through the convective zone due to magnetic buoyancy (Fig. 1.11c). The loops rise up to the surface to form the bipolar magnetic regions of opposite polarity as shown in Fig. 1.11 (d-f). At this stage, sunspots follow the Hale's polarity law after emerging from the photosphere, as explained before. Fig. 1.11 (g) shows that the meridional circulation (yellow circulations) at the surface drives the magnetic flux towards the polar region, where it cancels with the existing polar flux. Eventually the dominant polarity at the pole

is reversed. The flux is continually conveyed downward to the convective zone, towards equator. The field carried down depends on the polar field so when it changes sign so does the underneath field (Fig. 1.11 h). The newly reversed poloidal field again turns into toroidal field due to the differential rotation and a new solar cycle begins, as shown in Fig. 1.11 i.

The poleward migration of the zone of polar crown prominences can be seen in every solar cycle (Waldmeier 1973, Zirker et al. 1997). In the beginning of a solar cycle (solar minimum), the dominant zone of the filaments are found on the mid-latitudes ( $\sim 45^\circ$ - $50^\circ$ ), then the formation zone migrates to the polar regions. This process takes many years ( $\sim 5$  years) (Waldmeier 1973). They disappear during the polar polarity reversal, (Hyder 1965, Mouradian and Soru-Escout 1994, Webb 1998). Filament channels are commonly seen to link with each other by flux convergence and cancellation processes, to make a long chain of filaments (as shown in Fig. 1.15). The long chain of filaments are pushed polewards by the newly emerging flux at the lower latitudes or due to the meridional flows (Waldmeier 1957, Zirker et al. 1997).

More quiescent prominences are seen during the peak of the solar cycle (close to the solar maximum) at mid-latitudes between two separate magnetic bipoles (between diffused active region and active region flux). Mackay et al. (2008b) observed that 92% of quiescent and intermediate filaments were formed between the multiple bipole magnetic interaction region during the solar maximum. Such type of observations indicate that the maximum number of quiescent prominences are related to the solar activity due to more amount of the flux emergence in the solar maximum than the minimum. In the next section, we will discuss about the flux emergence process.

### 1.3.3 Flux emergence

As discussed in the previous section, we know that the magnetic field on the Sun is generated by the dynamo action. Sunspots emerge below the solar surface within the convection zone due to the Sun's differential rotation (Zwaan 1985, 1987). Magnetic buoyancy is an important driver for the flux emergence (Shibata et al. 1989). It plays an important role to lift the flux ropes to the solar surface. According to Parker's theory (Parker 1955a),

$$p_e = p_i + p_m \quad (1.8)$$

where  $p_e$  is the external gas pressure outside the flux tube which is equal to the sum of the internal gas pressure ( $p_i$ ) and the magnetic pressure ( $p_m$ ) within the flux tube. In this case magnetic field outside the flux tube is assumed to be negligible. The magnetic pressure and the internal gas pressure inside the tube is balanced by the external gas pressure:

$$p_e = p_i + \frac{B^2}{8\pi} \quad (1.9)$$

The buoyancy will take place when  $p_i < p_e$ . The magnetic pressure term is always positive thus satisfy  $p_i < p_e$ . This means that a flux rope is lighter than the surrounding and it rises above the photosphere. In this manner, the toroidal field rises buoyantly from the convection zone and appears as a bundle of field lines. Such regions emerge as a sunspot with equal flux of both polarities (Babcock and Babcock 1955). The emergence of a bipolar flux region as a bundle of vertical magnetic field lines is discussed by Thomas and

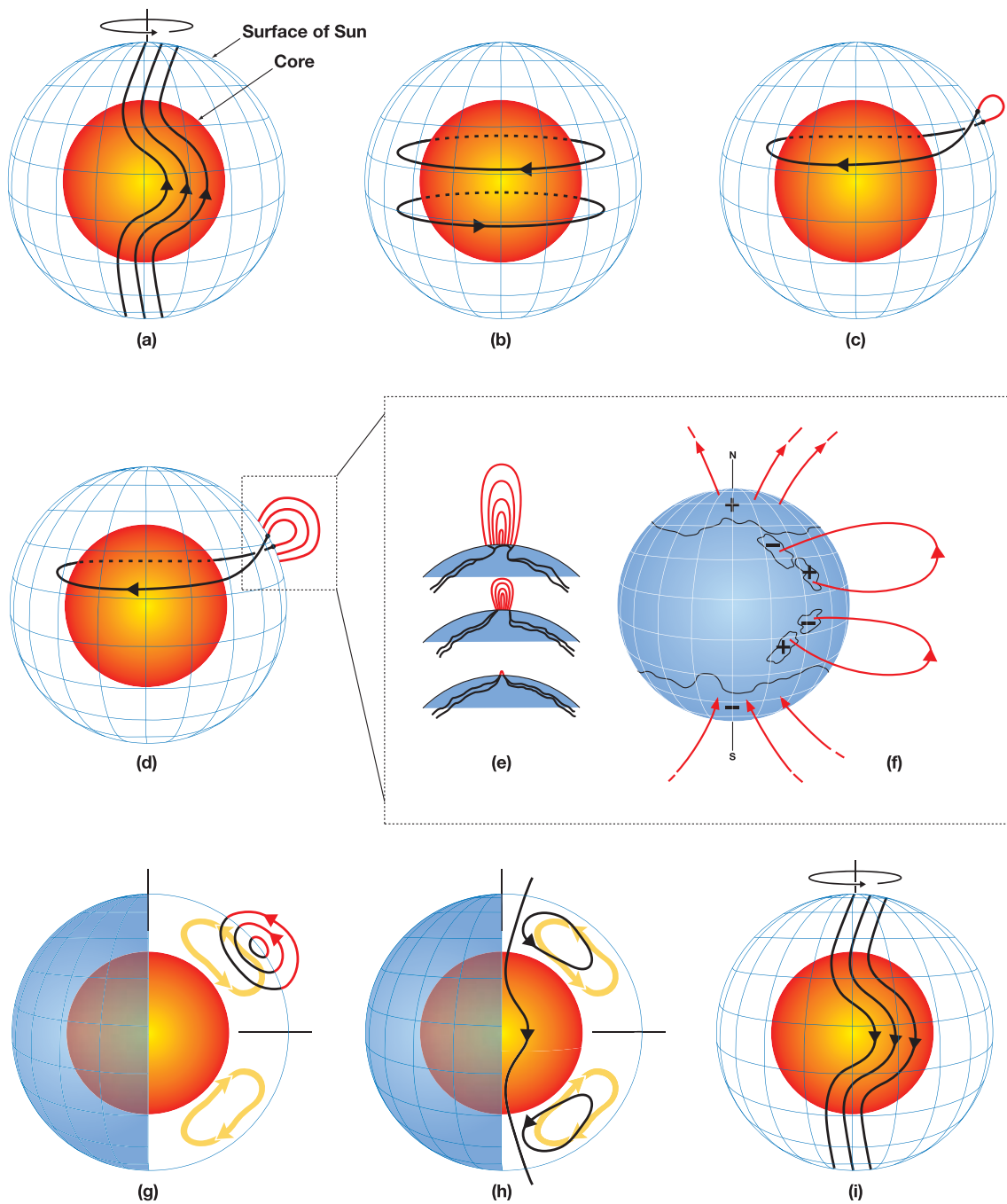


Figure 1.11: Schematic of solar flux transport dynamo process taken from Dikpati and Gilman (2009). The red inner sphere represents the radiative core of the Sun and the blue outer mesh the solar surface. In between the two layers is the convection zone, throughout which the dynamo process takes place. The black/red lines represents magnetic field below/above the surface. The yellow lines represents the meridional flows. Detailed description of the figure is given in the text.

Weiss (2008). As more and more flux emerges, the sunspot will grow in size and turn into larger spots. With time, they get diffused, sheared due to the differential motion of the Sun and prominences generally form in sheared field above the PIL in single or in multiple bipolar regions, see Section. 1.4). However, filaments are not formed during the flux emergence process, they only form when the bipolar regions naturally expand after the emergence. Usually the large-scale quiescent filaments are formed  $\sim$  one solar rotation after the flux emergence (Mackay 2005). Flux convergence and cancellation takes place between the separated bipolar regions and it leads to the formation of a filament channel (Gaizauskas et al. 1997, 2001, Wang and Muglach 2007).

## 1.4 Prominence models

In this section, we will summarize some of the important prominence models which are compatible with the observations in the present work of my thesis. These models try to answer some of the basic questions regarding prominences. How do the prominences form? How the cool plasma lifted upward? Since there is not enough prominence mass existing in the corona and plasma must come from the chromosphere (Pikel’Ner 1971, Saito and Tandberg-Hanssen 1973, Zirker and Cleveland 1994). In all the prominence models, the solar magnetic field is the main source of the prominence mass support.

Babcock and Babcock (1955) were the first to establish that prominences are formed above the neutral line of opposite polarity magnetic fields on the photosphere. Either they lie above the opposite polarity of the same bipolar regions or above the opposite polarity of the adjacent bipolar regions. Two prominence models have been established for understanding the prominence magnetic field configuration. One is the normal polarity model (Kippenhahn and Schlüter 1957) and other one is the inverse polarity model (Kuperus and Raadu 1974). According to the normal polarity model, direction of magnetic field is from positive to negative polarity and the prominence plasma is supported in the dips of magnetic field lines. The concave upward dips can occur in the potential field lines and the horizontal component ( $B_x$ , where the dip occurs) has same direction with respect to the overlying field lines. This is not very common in case of prominences because the field lines are highly non-potential in the filament channel. This was stated by Kuperus and Raadu (1974) who proposed the inverse polarity model. In this model, direction of magnetic field is from negative to positive polarity, dips are having inverse polarity with respect to the overlying field lines. Leroy et al. (1984) was the first who observed that the transverse field of the quiescent prominences, specially the polar crown prominences, has an inverse polarity (Anzer 1994, Antiochos et al. 1994, Kuperus 1996). However, the magnetic structure of the prominences is not fully understood by observations.

Furthermore, theoretical models have been proposed to explain how the prominence plasma is embedded in the field lines e.g. the sheared arcade model (Antiochos et al. 1994, DeVore and Antiochos 2000, Aulanier et al. 2002) and the flux rope model (Kuperus and Raadu 1974, Priest et al. 1989, van Ballegoijen and Martens 1989, Low and Hundhausen 1995, Aulanier and Demoulin 1998, Chae et al. 2001, Low and Zhang 2002, van Ballegoijen 2004, Gibson et al. 2006).

- *Sheared arcade model*: According to the sheared arcade model, initially field lines are potential in a filament channel. Footpoints move parallel to the polarity inver-

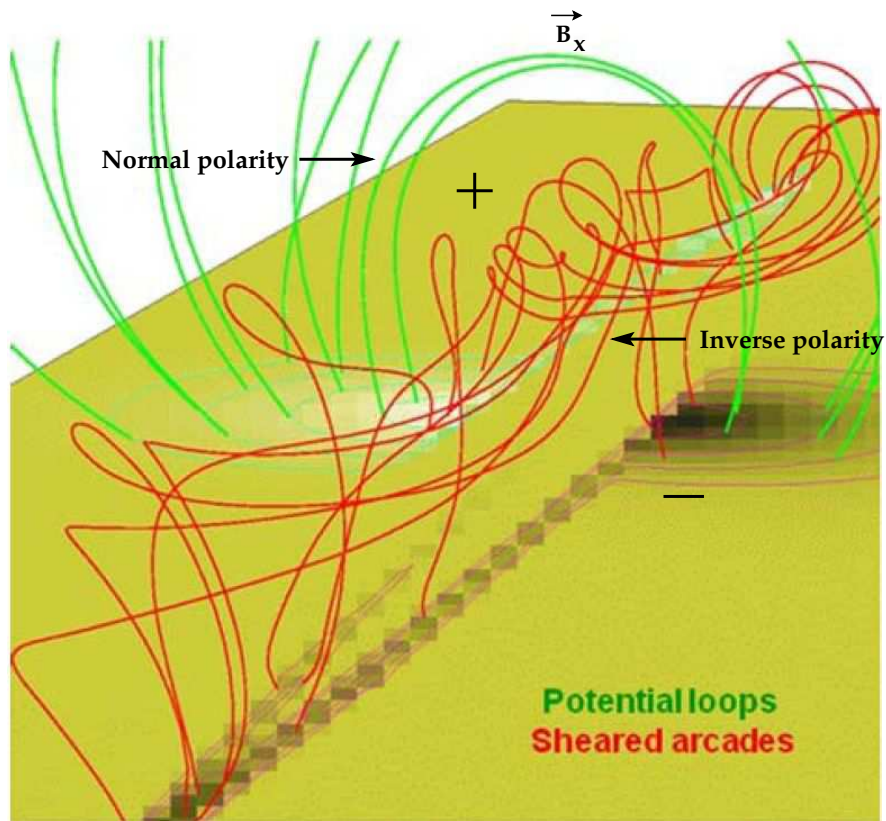


Figure 1.12: A sketch shows the sheared arcade model for magnetic field lines. Sheared arcade is shown in red colour lines and green lines represent the coronal arcade field lines. Image is adapted from Mackay et al. (2010).

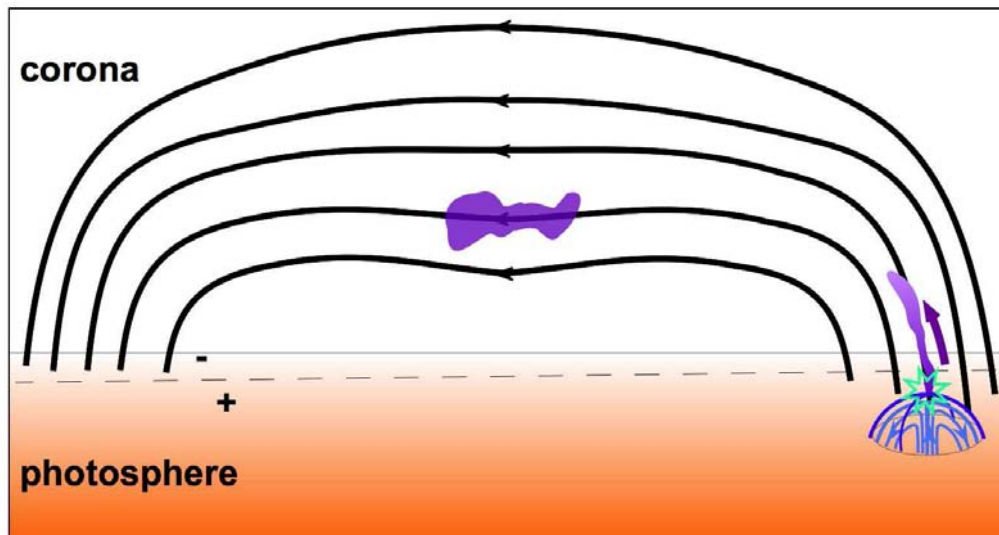


Figure 1.13: A sketch of an injection model, prominence plasma is shown in purple colour, heating is in blue colour and black lines are the filament channel field lines. Dashed line indicates the PIL. Figure adopted from Mackay et al. (2010).

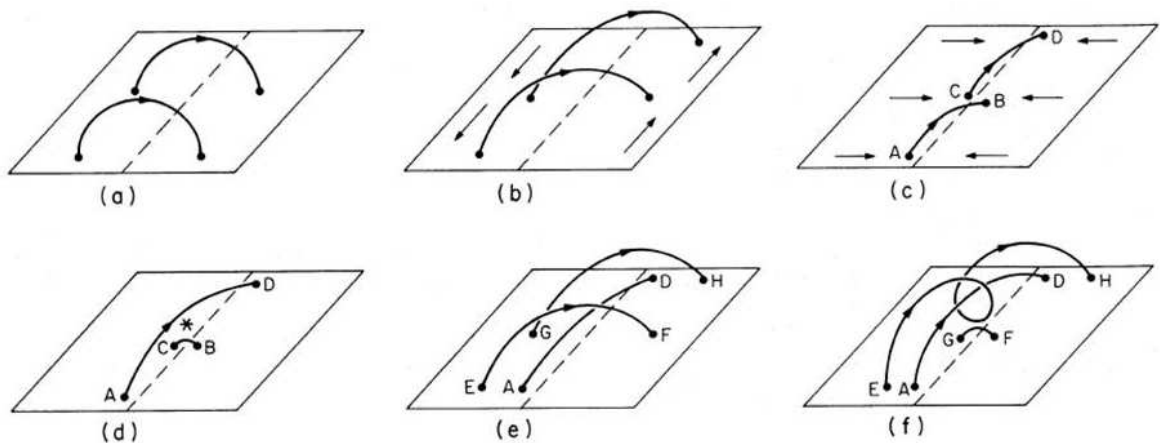


Figure 1.14: Prominence model for the formation of filament shown by van Ballegoijen and Martens (1989). Rectangular box represents the photosphere, polarity inversion line is shown by dashed line in each panel which separates the region of two magnetic field and solid lines are the magnetic field lines in a bipolar configuration.

sion line due to the shear, caused by the differential rotation or footpoint motion. Shearing causes the field to rise up from the footpoint and then dip down in the middle of the loop with an inverse polarity to the coronal arcade (red lines in Fig. 1.12). In Fig. 1.12, red lines show the field lines that carry the prominence plasma. The horizontal component ( $B_x$ , where the dip occurs) has an opposite direction to overlying green field lines which have normal polarity (Antiochos et al. 1994). According to the flux rope model the dip exists in the helical field lines, which is explained below.

- *Flux rope model:* van Ballegoijen and Martens (1989) introduced the model for the formation of a prominence through the flux cancellation by considering the shearing motions in a bipolar configuration. According to this model, also initially the field lines are potential which means that they are perpendicular to the magnetic PIL (Fig. 1.14a). Then due to the shear flow, footpoints get displaced along the PIL (Fig. 1.14b). Shear could be supplied due to the differential rotation on the Sun. In the next case (Fig. 1.14c,d), footpoints (marked as C and B) come closer, due to the flux convergence towards the PIL. As they come closer, they may reconnect to produce one small loop CB and one long loop AD (Fig. 1.14d,e). Small loop submerges in the solar surface because of its small radius of curvature (stronger the tension force) and magnetic buoyancy prevents the submergence of long loop because of its large radius resulting in a smaller tension force. Similarly, the footpoints of the overlying loops EF and GH come close and reconnect. This leads to the formation of a longer loop (EH). The longer loop EH wraps around the existing loop AD and forms a helical field structure (Fig. 1.14f) which carries the prominence material. This process repeats many times and building a long helical structure. Thus dipped magnetic field lines are formed carrying the plasma higher in the corona.
- *Flux linkage model:* A similar type of scenario is given by Martens and Zwaan

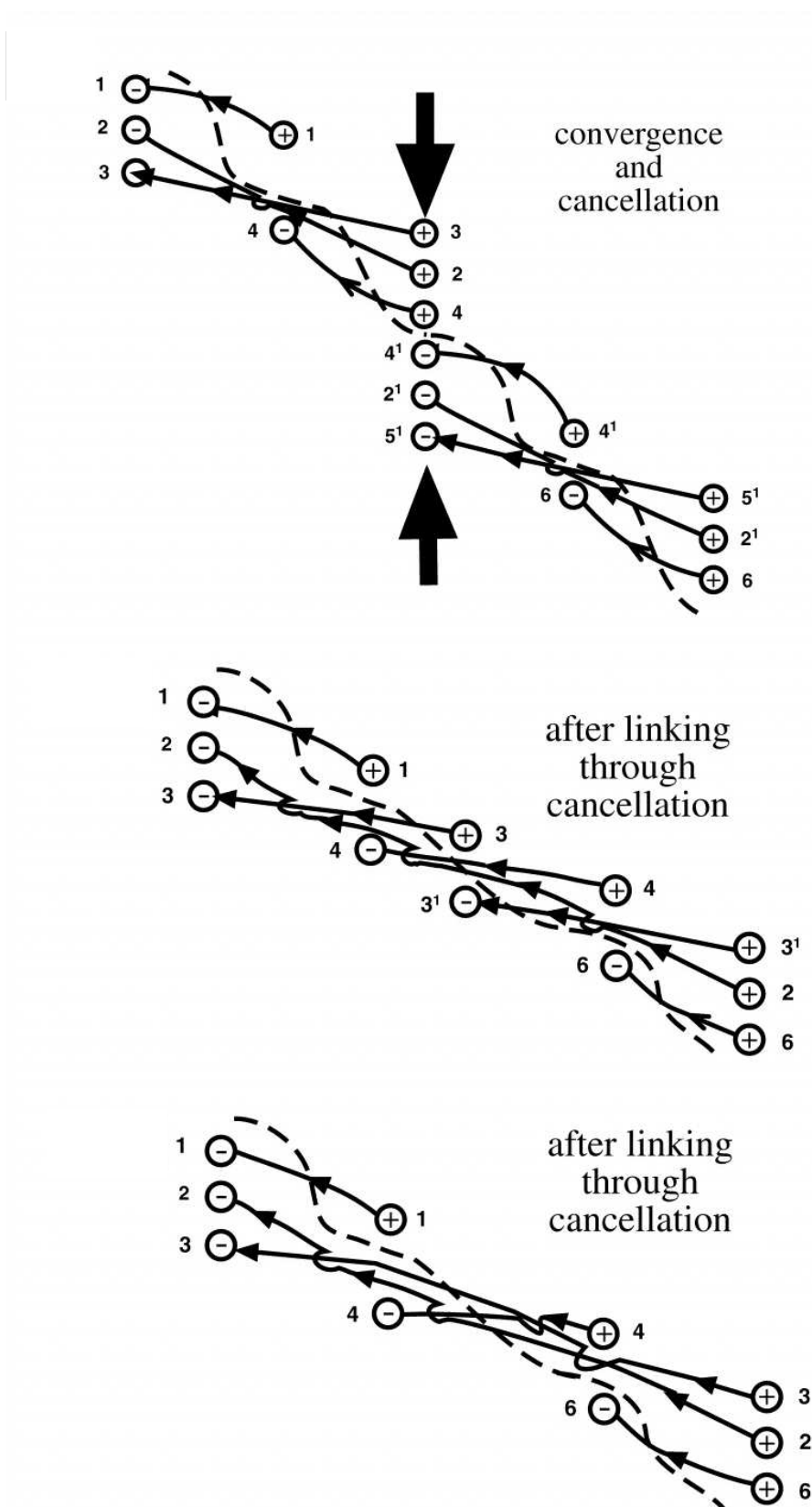


Figure 1.15: Flux linkage model for the growth of polar crown prominences. Dashed line in each panel indicates the polarity inversion line. Prominence plasma is located in the dips of the field lines, field lines can be identified with different numbers from 1 to 6. Image is taken from Martens and Zwaan (2001).



(2001) in the flux linkage model for the formation of polar crown prominences in the multiple bipolar configuration. There are two initially unconnected bi-poles (see Fig. 1.15, upper panel). Flux convergence and cancellation near the PIL (at 4 and 4'), reconnects the unconnected magnetic field lines (2 and 4, in Fig. 1.15 middle panel) and creates the longer loops with dips. For the reconnection, flux convergence is an important driver (also see Kuperus (1996), Kuijpers (1997), Litvinenko (1999, 2000)). In the interaction between two unconnected bi-poles, one is older and diffused which is at higher latitude, the other polarity is at lower latitude (and satisfies the Hale's Polarity Law and Joy's law). This results in the highly sheared field at the PIL. Thus, after the many repetitions of this process, it forms the long helical structures that can partly or fully cover the polar region of the Sun. Mackay et al. (2000), Mackay and van Ballegoijen (2001) have done numerical simulation supporting this type of filament formation. In Chapter. 3, we discuss observation of a similar scenario of a flux linkage in a polar crown prominence. In next paragraph, we will discuss the injection of the chromospheric material through the footpoint.

- *Injection model*: According to the injection model (Wang 1999, Chae et al. 2001, Mackay et al. 2010), cool plasma is ejected upward from the footpoints of the flux tubes of a filament channel (Fig. 1.13). The plasma is driven upward due to heating or by reconnection at the base of the footpoint of the field lines. This can be seen in the prominence observation too, as shown in Chapter. 3. One of the models proposed by Chae (2003) suggests that the reconnection occurs at the PIL. Reconnection associated with the barbs in the filament channel may also drive the plasma upward (Litvinenko 2000, Wang 2001, Chae et al. 2005). This type of upflows have been reported by Zirker and Cleveland (1994) and Berger et al. (2008).

Some of the recent observations suggest that the heating is mainly concentrated near the foot points of the loops (Aschwanden et al. 2001, Winebarger et al. 2002). According to the model of Antiochos et al. (1999), the heating length is smaller than the length of the loop, thus the plasma can cool down in the middle of the loop where heating is almost negligible (Serio et al. 1981, Mok et al. 1990, Klimchuk et al. 2010). Prominence material usually reside in the longer non-potential loops that are aligned along the PIL, not in the shorter potential loops. Therefore, condensation is more likely to take place in the longer loops than in the shorter coronal loops. However, heating at the footpoint is not well understood, it is discussed by many researchers (Antiochos and Klimchuk 1991, Antiochos et al. 2000, Karpen et al. 2001, 2003).

## 1.5 Prominence eruption

Even though, prominences are quite stable, they do erupt, specially the active region prominences are associated with flares and coronal mass ejections (CMEs). Prominences become unstable due to the emerging flux in the active part of the Sun. A lot of free magnetic energy is stored in the active regions and a sudden release of the magnetic energy leads to the flares, CMEs and prominence eruptions (Low 1981, Forbes 2000). AR prominences/filaments may erupt with or without CMEs.

Quiescent prominences are also observed to erupt. Su and van Ballegooijen (2013) have reported the eruption of a large polar crown prominences associated with a CME, due to the increase in the twist of the field lines. However, the reason for the sudden prominence destabilization is still not completely known.

CMEs and flares are important to study because they cause space weather problems on Earth. Until now, it is not well understood how an eruption begins. Filaments mainly consist of chromospheric plasma, suspended in the solar corona and participate in the most of the CMEs. Therefore, filaments can be used as tracers to locate the erupting field in the lower corona (Sterling and Moore 2005). For this, we need to study the evolution of the prominence, then how the eruption begins. The study of the erupting prominence structure may shed light on the triggering mechanisms of eruptions and CMEs. The present study is not focused on the prominence eruption therefore we will not go into deeper details. However, as proposed in last chapter, I plan to investigate the structure and dynamics of erupting prominences in the future.

### 1.6 Outline of the thesis

Solar prominences and filaments have been investigated for more than 50-60 years. A lot of work is done on the prominences and on the filaments. Until now, no observations have been reported of a prominence seen at the limb and simultaneously its filament flows structure and related coronal brightenings against the disk. Now it has been possible to disentangle the 3-D structure of the prominences by combining the data from two directions normal to each other. Solar Dynamic observatory (SDO) provides the high spatial and temporal resolution images of the prominences and filaments that are observed simultaneously as filaments and prominences with the Solar TERrestrial RELations Observatory (STEREO) spacecraft. In the present study, STEREO spacecraft are 90 degrees to Earth-Sun line. I combine the observations from both the directions by using the data from SDO and STEREO spacecrafts and study the prominences in 3-D. The main aim of this thesis is to study the flows and dynamics of quiescent prominences and compare the observations with the theoretical models to understand their structure. In this study, I have analysed two different types of quiescent prominences, one is quiescent polar crown prominence and the other one is a quiescent active (tornado-like) prominence.

Chapter 2 focuses on the details of the two instruments - SDO and STEREO, which are used in this work. I have shown the position of both the spacecraft during our observations and have discussed how to find exact locations of limb features on disk images. A detailed method of background removal for the SDO images is described.

In the third chapter, I have presented the study of a quiescent polar crown prominence. Data from SDO and STEREO of a polar crown prominence were analysed for two days. The small polar crown prominence was situated at 60-70° latitude. To find the prominence position on STEREO disk images, different timeseries was created through different structures. I compared the flows of filaments on disk with prominence dynamics seen on the limb. The off-limb prominence plasma was interestingly connected to the other prominences which are hundreds of arc seconds away from each other. A small-scale coronal cavity became visible during the upflow from one of the prominence pillars. Prominence pillars showed the dominant up-flows and down-flows at different sites. To

compare the prominence positions and brightening in the filament channel with the underlying photospheric magnetic field, I have used line-of-sight SDO/HMI magnetogram and GONG synoptic maps.

A huge solar tornado was observed by the SDO on 25 September 2011. In chapter 4, I have presented a study of a quiescent tornado-type prominence. The data of quiescent prominence was analysed for one day to study its activation, it appeared as a tornado after the activation of the prominence. An active region was observed near the prominence-cavity system. There were three flares associated to the active region. Each time they influenced the prominence-cavity system. From disk images, it was noticed that the flares were associated with EUV waves and CME's. To understand the relation between the flares and the prominence-cavity system, a number of timeseries were generated at different times. A simple mathematical model was constructed for the explanation of the cavity expansion.

In chapter 5, I have presented a preliminary result of the Differential Emission Measurement (DEM) applied on some of the prominences. I have used DEM to study the multi thermal prominence structure. It measures the electron number density along the line-of-sight that contributes to the different emitted temperature ranges (Craig and Brown 1976).

Finally, in chapter 6, I have summarized the results presented in the thesis and have outlined some of the future plans.



## 2 Instruments and data analysis techniques

Our Earth receives light from the Sun at all wavelengths of electromagnetic radiation. There is a limitation to study the solar corona from the Earth's surface. The hotter plasma in the solar corona is mainly observed in the Extreme ultraviolet (EUV), X-rays and gamma rays and these wavelengths are blocked by the Earth's atmosphere (Fig. 2.1). This problem can be reduced with the use of space-based telescopes, which are above/outside the Earth's atmosphere.

There are many spacecraft missions that are observing the corona in these wavelengths. GOES is a geostationary satellite that measures the soft X-ray flux from the Sun and categorizes the flares. The Reuven Ramaty High Energy Solar Spectral Imager (RHESSI) can image solar flares at wavelengths from soft X-rays to high gamma rays (Lin et al. 2002, 2003a). SOHO, HINODE, STEREO and SDO are used to image the Sun at different EUV wavelengths.

In the present thesis work, we have used the EUV images from Solar Dynamic Observatory (SDO) and Solar TERrestrial Relations Observatory (STEREO) to study the prominence structures at different coronal temperatures.

### 2.1 The SDO

The Solar Dynamic Observatory is a NASA mission. The spacecraft was launched on 11 February 2010 from Cape Canaveral Air Force Station (Pesnell et al. 2012). The main aim<sup>1</sup> of the SDO is to understand the 11-year solar variability, how it is generated and how the solar activity is related to the space weather. Another objective of the SDO is to understand the magnetic field configuration from the Sun's interior to the outside (in the corona) and to understand what drives Coronal Mass Ejections (CME), prominence eruptions and flares. To achieve these scientific goals, the following three instruments have been built (see Fig. 2.2):

- *Heliospheric and Magnetic Imager (HMI)*: HMI is designed to study the oscillations and the magnetic field at the solar surface. It delivers continuum images, dopplergrams, line-of-sight and vector magnetograms of the photosphere. For more details of this instrument see paper by Schou et al. (2012)

---

<sup>1</sup><http://solar-center.stanford.edu/sdo/SDOguide.pdf>

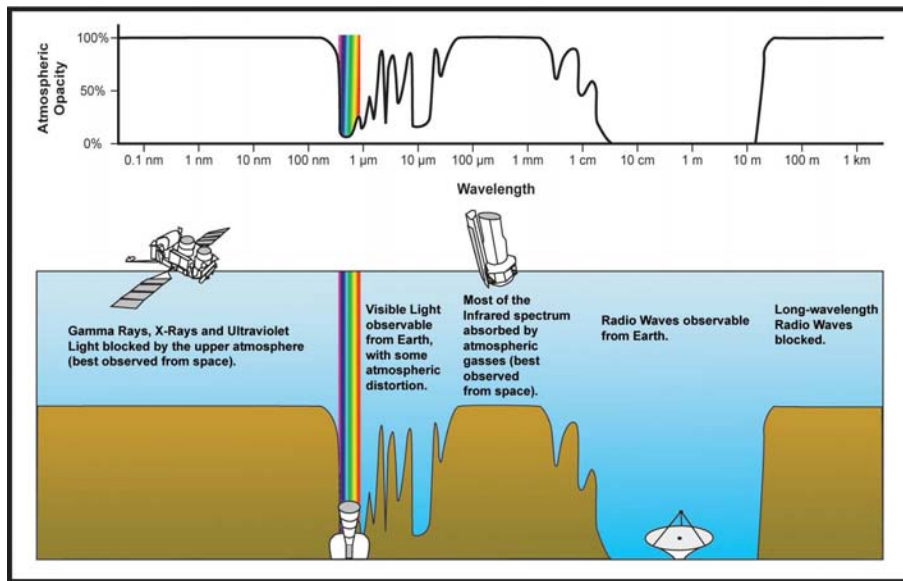


Figure 2.1: This image shows the opacity of the Earth’s atmosphere in different wave-lengths ranges. Credit: NASA/IPAC.

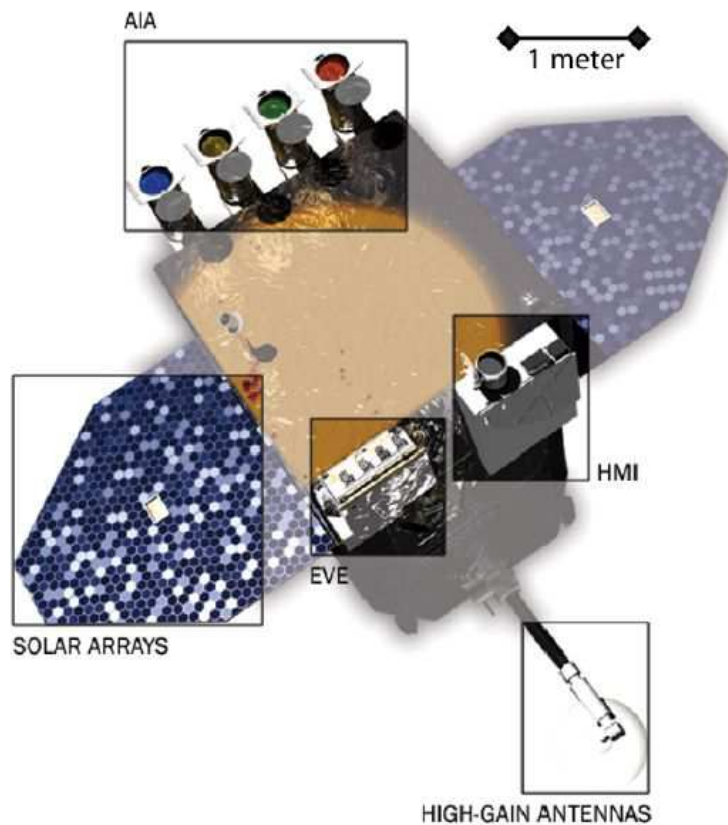


Figure 2.2: An image of the SDO spacecraft, showing its three main instruments: HMI, AIA and EVE. Solar arrays and high-gain antennas are on the left and bottom side. Image adapted from Pesnell et al. (2012).

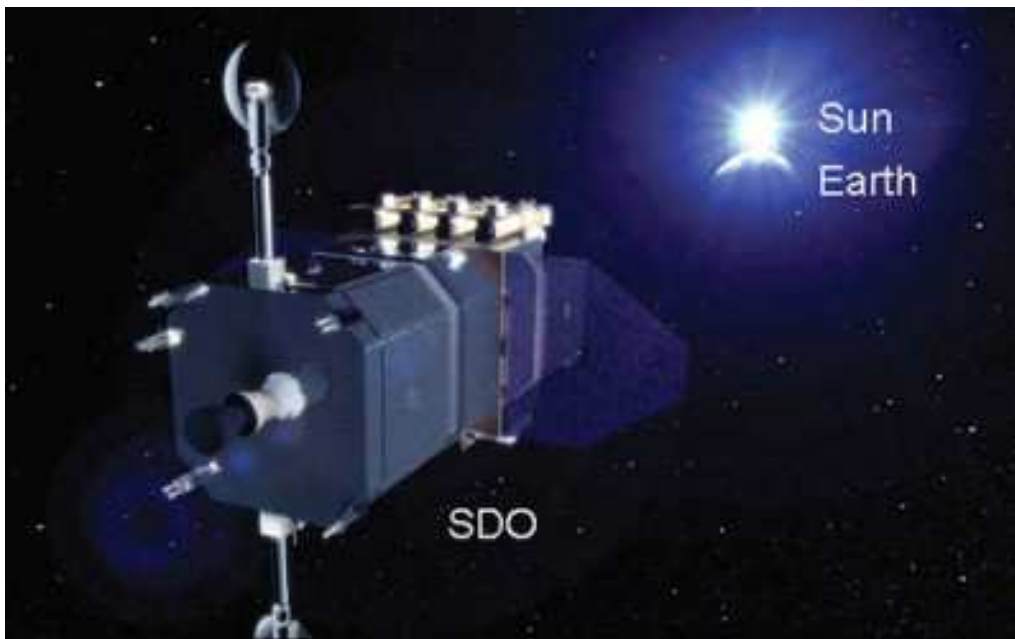


Figure 2.3: An image of the SDO spacecraft during an eclipse. The Earth passes between the Sun and SDO, and blocks the SDO's view. Credit: NASA.

- *Atmospheric Imaging Assembly (AIA)*: AIA observes the Sun in multiple wavelength channels to investigate a broad range of scientific objectives. For example - dynamics of coronal structures, coronal heating - what is the source of heating and coronal emission, magnetic reconnection, origin of coronal mass ejections and how they propagate into the heliosphere. The main aim of AIA is to understand the connection between the Sun and Earth (Lemen et al. 2012).
- *Extreme Ultraviolet Variability Experiment (EVE)*: EVE is mainly focussing on the understanding of solar EUV irradiance, how the EUV spectral irradiance varies, try to forecast the EUV spectral variability to avoid the geospace disturbances. Because the solar EUV radiance is the primary source of disturbances at the Earth's atmosphere. Detailed information can be found in paper by Woods et al. (2011).

All the three instruments are onboard the SDO spacecraft and observing full solar disk simultaneously. We will discuss these instruments in detail in the next sections. An image of the spacecraft is shown in Fig. 2.2. The total mass of the spacecraft is 3000 kg. It has high-gain antennas and solar arrays which produce 1500 W of power. The SDO mission is planned for five-years. It's ground station is located at White Sands Complex in New Mexico.

### 2.1.1 SDO orbit

The SDO spacecraft is placed in an inclined geosynchronous orbit at an altitude of 35,350 kilometers (Pesnell et al. 2012). The orbit allows SDO to continuously observe the Sun and to have nearly continuous contact with a single ground station ensuring a high data transfer rate of high resolution and cadence solar images. It has the eclipse seasons twice

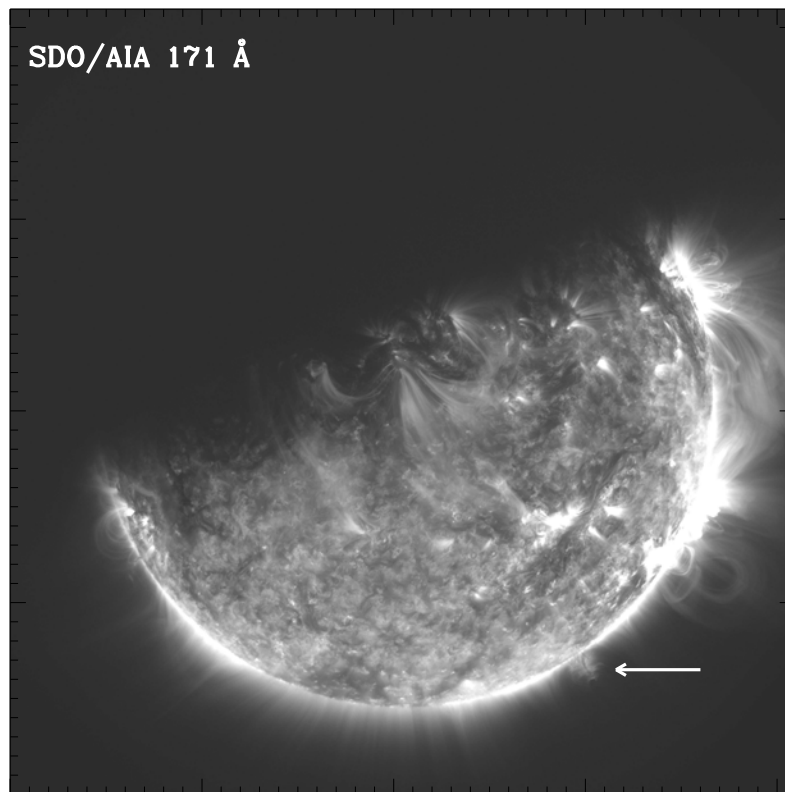


Figure 2.4: SDO/AIA 171 intensity image observed during eclipse on 25-September-2011 at 07:14:00 UT. The white arrow points the tornado-like prominence (See Chapter 4, Fig. 4.1 for closer view of tornado).

in a year during equinox. Once in March (spring season) and other one is in September (fall season). During these months, the Earth passes between the SDO and the Sun for three weeks (Fig. 2.3). Therefore the Earth blocks the SDO view for  $\sim 2$  hours in day. In our observations of a tornado 25 September 2011 (see Chapter. 4), we have faced the eclipse problem, when the Earth came in between the Sun and the SDO (Fig. 2.4).

### 2.1.2 SDO/AIA

The Atmospheric Imaging Assembly (AIA) is an instrument on the SDO spacecraft. As mentioned above, it has been built to study the temporal evolution of the solar coronal structures (Lemen et al. 2012). To achieve this goal, AIA has been designed to take high cadence full-disk images in ten different wavelength bands, seven in EUV, two in UV and one in Visible channel. It provides high spatial resolution images of  $0.6''$  per pixel of entire solar disk ( $4096 \times 4096$  pixel images) with a cadence of 12 seconds which were not available before. Previously the best instrument for full-disk coronal images was EIT on SOHO (Delaboudinière et al. 1995). Because of the limited temporal and spatial resolution of EIT/SOHO, the detailed investigation of corona was not possible. On the other hand, Transition Region and Coronal Explorer (TRACE) satellite (Handy et al. 1999) was successful in observing the corona at high spatial and temporal resolution but in comparison to AIA, TRACE had a much smaller field of view and fewer wavelength



channels. The AIA is capable of taking almost simultaneous observations of the entire solar disk in wavelength bands selected to pick-out structures with plasma temperatures from  $10^4$  to  $10^7$  K. A detailed information is given in Table. 2.3

The AIA instrument is made up of four Cassegrain telescopes. Fig. 2.5 shows the schematic diagram of four AIA telescopes in different wavelength band passes. Each of the four telescopes is divided into two parts and one half of telescope no. 3 has three selectable UV-Visible wavebands and the other half of it has 171 Å wavelength band. The remaining three telescopes (no. 1, 2 and 4) have one wavelength on each half (see Table. 2.1). The field of view of each telescope is 41 arcmin with  $4096 \times 4096$  pixels (see Table. 2.2 for the other parameters of the AIA instrument). Further detailed information about the telescopes is given in the papers by Cheimets et al. (2009) and Boerner et al. (2012).

Table 2.1: The position and central wavelength of different AIA channels. This table is taken from Podgorski et al. (2009)

Telescope	Position	Center Wavelength
1	Top	335 Å
1	Bottom	131 Å
2	Top	211 Å
2	Bottom	193 Å
3	Top	UV/Visible
3	Bottom	171 Å
4	Top	304 Å
4	Bottom	94 Å

### 2.1.3 SDO/HMI

Apart from the AIA data, we have also used a few line-of-sight magnetograms, observed by SDO/HMI in the present thesis work. In this section, we will briefly describe the HMI instrument.

The Helioseismic and Magnetic Imager (HMI) is designed to study the dynamics and origin of magnetic field on the Sun (Scherrer et al. 2012). The instrument was built at the Lockheed Martin Solar and Astrophysics Laboratory (LMSAL) in collaboration with Stanford University. HMI provides full-disk continuum images, Doppler velocity, line-of-sight magnetic field maps in Fe I line at 6173 Å with temporal cadence of 45 s and spatial resolution of 0.5 arcsec per pixel. It also provides the vector magnetic field with temporal cadence of 90-135 seconds (Scherrer et al. 2010, 2012).

The HMI obtains one full-disk line-of-sight magnetograms images at every 45 s. This is an improved version of the SOHO's instrument - Michelson Doppler Imager

Table 2.2: Important parameters of the AIA instrument (Lemen et al. 2012)

CCD detector	
Pixel size	0.6 ''
Array size	4096 × 4096
Field of view	41 × 41 arcmin <sup>2</sup>
Cadence of all telescopes	10 s to 12 s
Exposure time	0.5 to 3 s
About telescope	
Mirrors	Multilayer-coated Zerodur
Primary diameter	20 cm
Focal length	4.1 m

(MDI) (Scherrer et al. 1995), with higher spatial resolution and higher cadence. Additionally, it also provides the vector magnetograms. A detailed information about the HMI filter characteristics, image quality can be found in the papers by Couvidat et al. (2012) and Wachter et al. (2012). The HMI data<sup>2,3</sup> are freely available on web for the scientific community.

## 2.2 The STEREO

The STEREO (Solar TERrestrial RELations Observatory) spacecraft is also a NASA solar observation mission (Howard et al. 2008). It was launched on October 26, 2006 from Cape Canaveral Air Force Station in Florida. The STEREO mission contains two identical spacecrafts and both were launched on the same day. One is STEREO Ahead (STEREO-A) and the other is STEREO Behind (STEREO-B), both orbiting around the Sun. The spacecraft observe the Sun from two different directions (see Fig. 2.6). They are in two slightly different orbits. The STEREO-A orbits slightly inside the Earth's orbit, which takes 347 days to complete one revolution around the Sun whereas STEREO-B orbits slightly outside the Earth's orbit which takes 387 days. Every year, both the spacecraft move apart from each other, roughly by 44°. The current position of the spacecraft can be found at the web<sup>4</sup>. The STEREO provides the images of structures from different angles than seen from the Earth. This is the main benefit of the STEREO images that we can combine the data of different angles with the Earth's view e.g. SDO. In this way, we can study the solar structures in 3-dimensions (3D). In the present thesis, we combine the STEREO data with the SDO and construct the 3D view of prominences. During our observation, SDO and STEREO-A were at ~ 90° to the Earth-Sun line. Fig. 2.8 shows

---

<sup>2</sup><http://hmi.stanford.edu>

<sup>3</sup><http://jsoc.stanford.edu>

<sup>4</sup><http://stereo-ssc.nascom.nasa.gov/where.shtml>

Table 2.3: The primary ions observed by AIA and their approximate height of formation. The table is taken from Lemen et al. (2012)

Channel	Primary ions(s)	Region of atmosphere	log(T)
4500Å	continuum	photosphere	3.7
1700Å	continuum	temperature minimum, photosphere	3.7
1600Å	C IV	transition region, upper photosphere	5.0, 4.0
304Å	He II	chromosphere, transition region	4.7
171Å	Fe IX	quiet corona, upper transition region	5.8
193Å	Fe XII, Fe XXIV	corona and hot flare plasma	6.2, 7.3
211 Å	Fe XIV	active-region corona	6.3
335 Å	Fe XVI	active-region corona	6.4
94 Å	Fe XVIII	flaring corona	6.8
131 Å	Fe VIII, Fe XXI	transition region, flaring corona	5.6, 7.0

the position of both the spacecraft.

The STEREO spacecraft has a set of four different scientific instrument packages: 1) Sun Earth Coronal and Heliosphere Investigation (SECCHI); 2) In-situ Measurements of Particles and CME Transients (IMPACT); 3) PLASMA and SupraThermal Ion Composition (PLASTIC); 4) STEREO/WAVES (SWAVES). In this thesis, we only use the data from SECCHI/EUVI, therefore in the following section we will give the brief description about the EUVI instrument:

### 2.2.1 SECCHI/EUVI

The Sun-Earth Connection Coronal and Heliospheric Investigation (SECCHI) is a set of telescopes on STEREO that observes features from the solar surface out to interplanetary space (Wuelser et al. 2004, Wülser et al. 2007). The main purpose of the SECCHI is to observe CME's and other solar structures in 3D, e.g. loops, plumes, prominences, etc (Howard et al. 2008). It consists of five telescopes, that are observing the Sun, its outer

corona and the heliosphere.

- The Extreme Ultraviolet Imager (EUVI) takes images in four different wavelengths bands : 304Å, 171Å, 195Å and 284Å (see Table 2.4), which have been selected to image the Sun's atmosphere from the chromosphere to the corona. The main emission lines centering to the wavelength bands have formation temperature in the range of the from 80000 K to 20 MK.

Fig. 2.7 shows a schematic internal view of the EUVI telescope (Howard et al. 2008). The EUV light entering the telescope encounters the thin metal filter which suppresses the UV, visible and IR radiation in order to keep the telescope cool. The radiation passes through one of the four quadrant selectors, shown by arrow in Fig. 2.7. To optimize the EUV lines, primary and secondary mirrors are coated with a narrow-band, multilayer reflective coating. The reflected light from the primary and secondary mirror continues through thin aluminium filters which further reduce the remnants of the visible and IR radiation. The exposure time is controlled by the rotating blade shutter. Finally the images are received by the CCD detectors. The important parameters of the telescope are listed in Table 2.4.

- There are two visible light Lyot coronagraphs - COR1 and COR2. One takes the images of the inner corona from 1.4 to 4  $R_{\odot}$  and other one is imaging the outer corona from 2 to 15  $R_{\odot}$
- There are two heliospheric imagers H-1 and H-2. These telescopes observe the CMEs, solar wind and heliospheric structures when the travel from the corona through the heliosphere to Earth.

Table 2.4: Important parameters of the EUVI instrument (Wuelser et al. 2004)

Wavelengths	Main emitting ion
304Å	He II
171Å	Fe IX
195Å	Fe XII, Fe XXIV
284Å	Fe XV
About telescope	
Instrument type	Normal incidence EUV telescope (Ritchey - Chretien)
pixel size	1.6 arcsec
Focal length	1750 m
Primary diameter	9.8 cm
Array size	2048 × 2048

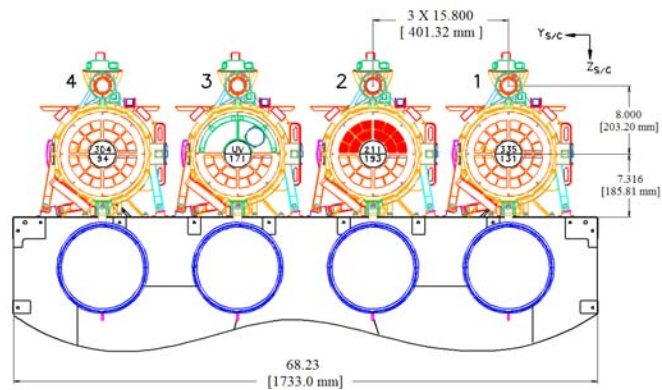


Figure 2.5: Sketch of the four AIA telescopes showing the division of wavelength bands. Each telescope is divided into two parts. The waveband of each part is shown in Table 2.1. (courtesy of Podgorski et al. (2009)).

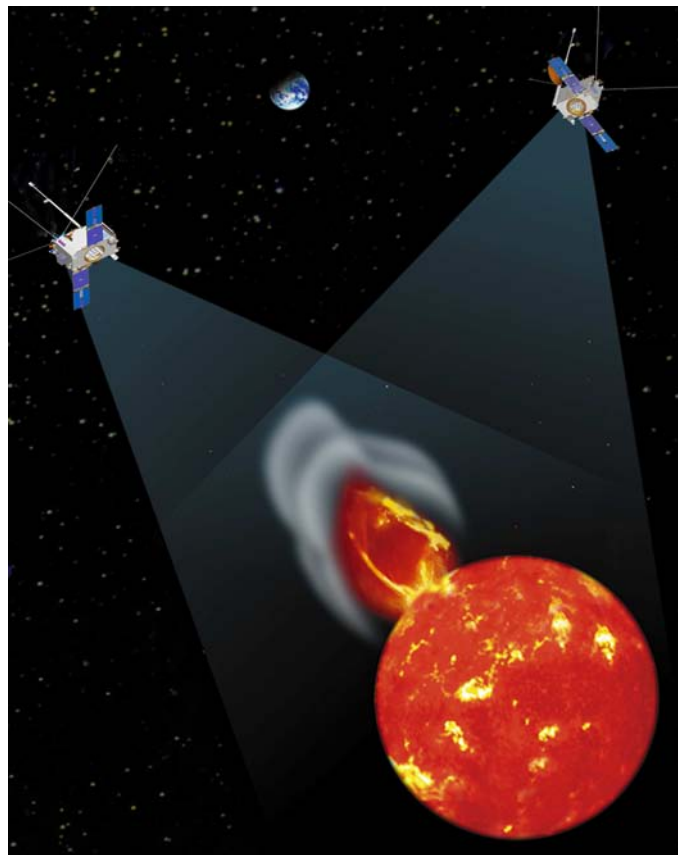


Figure 2.6: The image shows the twin STEREO spacecrafts - STEREO-A, STEREO-B observing the Sun from different directions. Courtesy: [http : //stereo.jhuapl.edu/mission/overview/overview.php](http://stereo.jhuapl.edu/mission/overview/overview.php)

## 2.3 Data analysis techniques

The present work mainly deals with the study of the dynamics of the prominences, by using SDO observations and combining them with observations from STEREO to obtain the observations of the prominences from two directions to study the 3-D structure of the prominences. We studied two different types of a quiescent prominences: A quiescent polar crown prominence and quiescent tornado-like prominence. In the study of both the prominences, we have used the STEREO-A images because prominences were only visible from STEREO-A near the disk center and were not seen by STEREO-B. The position and separation angle between the SDO and STEREO-A are shown in Fig. 2.8. During the observations of a polar crown prominence (on February 13, 2011), the separation angle was  $86^\circ$  between both the spacecraft. During the study of the tornado-like prominence (on September 25, 2011), the separation angle was  $103^\circ$  (Fig. 2.8). The images at  $304 \text{ \AA}$ ,  $171 \text{ \AA}$  and  $193 \text{ \AA}$  are used from SDO and images at  $195 \text{ \AA}$  are used from STEREO/EUVI. Images at  $195 \text{ \AA}$  are available with relatively higher temporal cadence than other STEREO images. The EUVI data are available on the web<sup>56</sup>. The EUVI images contain three levels of calibration<sup>7</sup>.

- Level 0.5 - It contains the raw data.
- Level 1.0 and 2.0 - Level 0.5 images are calibrated into level 1.0 and 2.0 by using the SolarSoft routine - SECCHI\_PREP.pro. The data have also been corrected for despiking, flat fielding and roll angle.

Atmospheric Imaging Assembly (AIA) provides full-disk images with high spatial and temporal cadence (Section. 2.1.2). By using the continuous AIA images we study the flows and dynamics of the prominences. We used the  $304 \text{ \AA}$ ,  $171 \text{ \AA}$  and  $193 \text{ \AA}$  images from SDO/AIA. The AIA data are freely accessible from web<sup>8</sup>. Calibration of the AIA data is described in the paper by Boerner et al. (2012). A detailed description the AIA data calibration is also available on the web page<sup>9</sup>. The AIA data has three levels<sup>10</sup>: level 0, level 1.0 and level 1.5.

- Level 0 - It contains the raw elementary data.
- Level 1.0 - It contains the compressed FITS files and all files are corrected for bad pixels, flat field and cosmic ray spikes (these are formed due to the collisions of high energy particles). All higher level data are constructed from level 1.0.
- level 1.5 - After getting the level 1.0 data, it has to be converted in to level 1.5 by using the SolarSoft routine - aia\_prep.pro. All images are corrected for its different plate scale and roll angle.

After the above calibration, we also normalized the all AIA images by dividing by its exposure time.

---

<sup>5</sup><http://secchi.lmsal.com/EUVI/DOCUMENTS/pptpreview.html>

<sup>6</sup>[http://secchi.lmsal.com/EUVI/DOCUMENTS/data\\_analysis\\_euvi2.html](http://secchi.lmsal.com/EUVI/DOCUMENTS/data_analysis_euvi2.html)

<sup>7</sup>[http://sohowww.nascom.nasa.gov/solarsoft/stereo/secchi/doc/secchi\\_prep.html](http://sohowww.nascom.nasa.gov/solarsoft/stereo/secchi/doc/secchi_prep.html)

<sup>8</sup>[http://www.lmsal.com/get\\_aia\\_data/](http://www.lmsal.com/get_aia_data/)

<sup>9</sup>[https://www.lmsal.com/sdodocs/doc/dcur/S\\_DOD0060.zip/zip/entry/](https://www.lmsal.com/sdodocs/doc/dcur/S_DOD0060.zip/zip/entry/)

<sup>10</sup>[http://solar-center.stanford.edu/sdo/SDO\\_Guide.pdf](http://solar-center.stanford.edu/sdo/SDO_Guide.pdf)

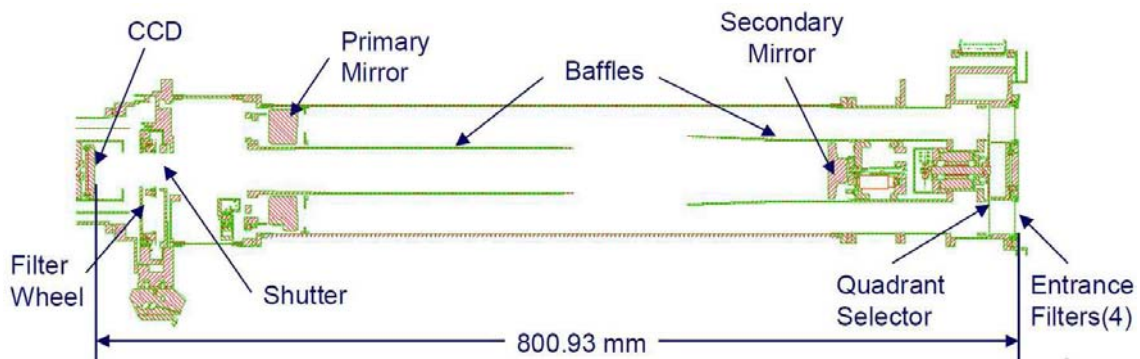


Figure 2.7: The cross-section view of EUVI telescope. Image is taken from Wuelser et al. (2004).

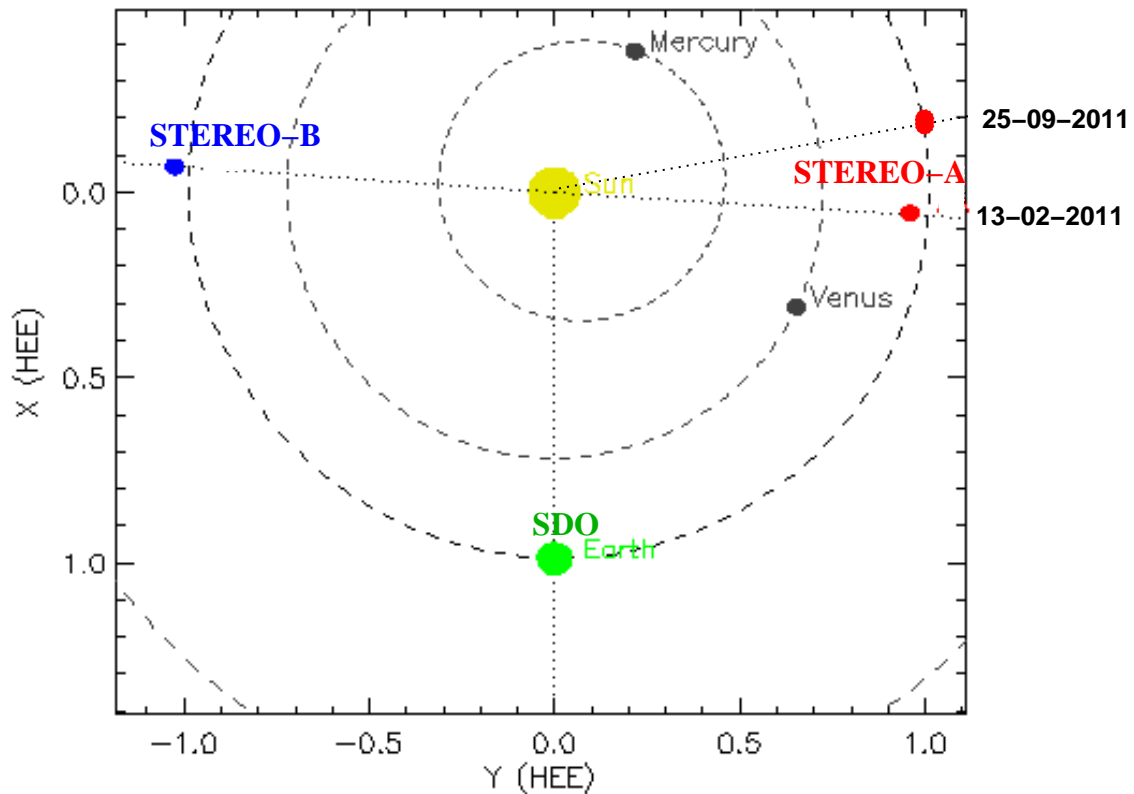


Figure 2.8: The figure shows the position of STEREO-A (right hand side, red dots) during the study of two different prominences presented in the Chapter 3 and Chapter 4.

### 2.3.1 Background removal

To improve the visibility of the cavity and prominence structure, we removed an average background from the SDO/AIA 171 Å and 193 Å images. For this purpose, first we download the four full disk, high resolution images for everyday over a period of two months around the date of our observations and calculated median of them. For example, for the analysis of the quiescent prominence observed on 25 September 2011, we used the September and October 2011 images to compute the background. Then we calculated

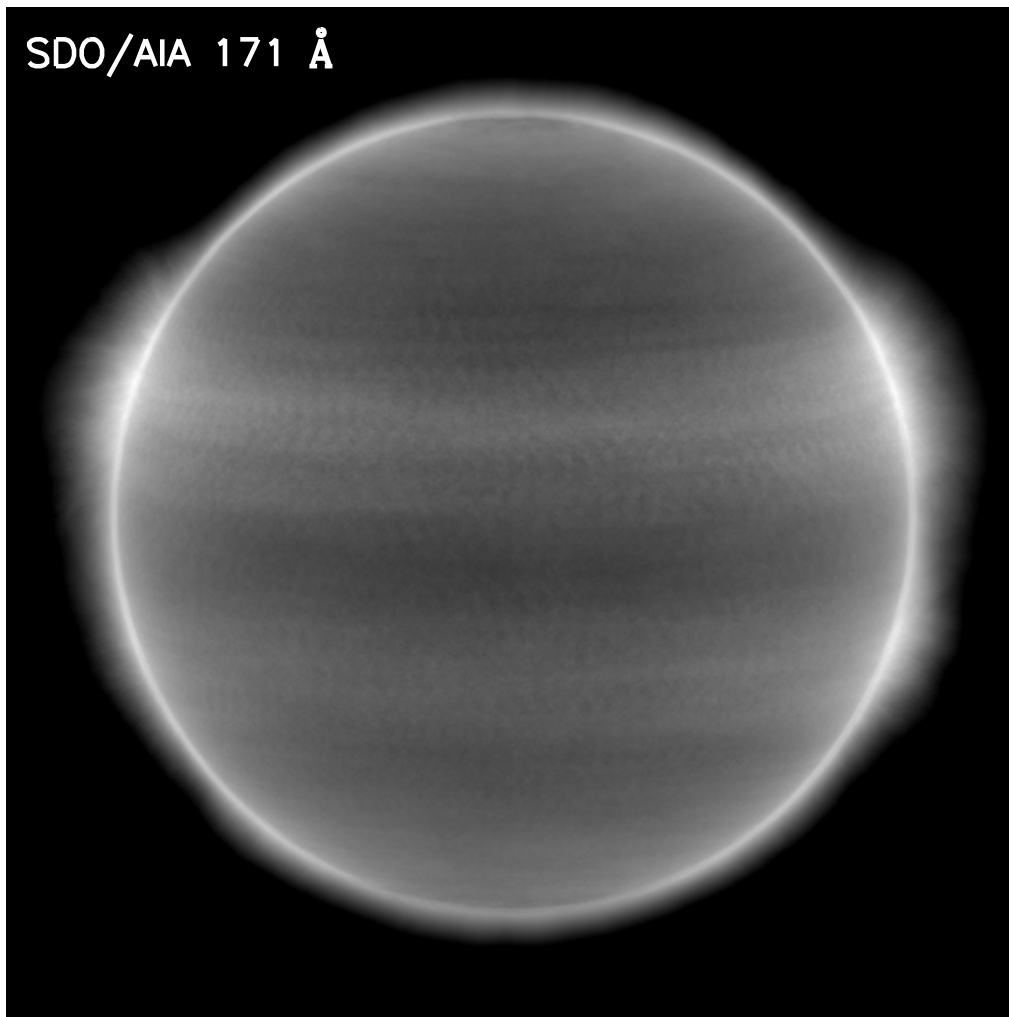


Figure 2.9: SDO/AIA 171Å median image calculated for two months of data.

the median of two months data set. We used median because it avoids the too high and too low pixel values and gives the smooth background image with intensity decreasing radially outwards from the limb, as shown in Fig. 2.9. All analysed intensity images are obtained by taking the logarithm of the ratio of the intensity images to the background image. The advantage of taking the log of the ratio rather than subtracting the average is that this reflects relative changes so both bright and faint features show up equally well.

Fig. 2.10 shows a clear difference between the images before and after the background removal. In Fig. 2.10, upper panel, we can see that prominence structure and active region loops are not visible due to the hazy background. The cavity was clearly visible after removing the background. Similarly background removal has been done in the case of the polar crown prominence.

### 2.3.2 Feature identification

To construct a 3D geometry of the prominence structures, we need to know the exact locations of the particular feature on both the images (SDO and STEREO). First we select



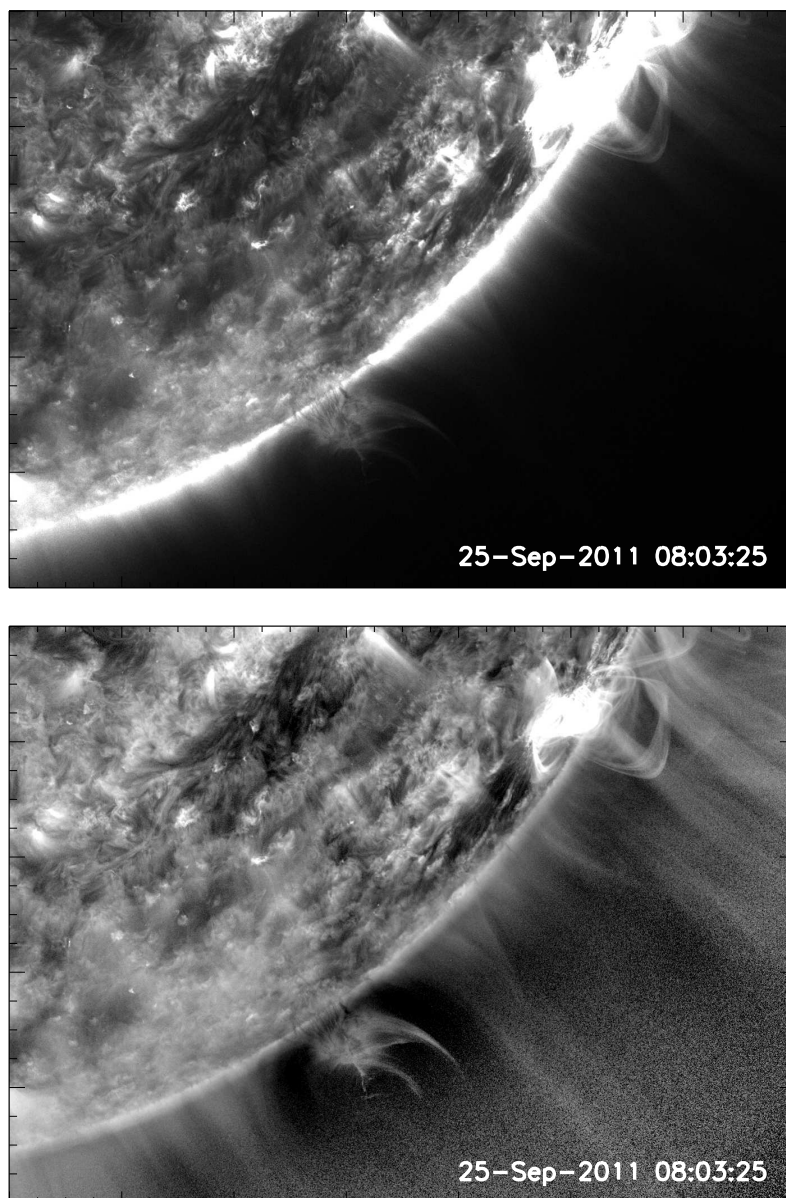


Figure 2.10: *Upper panel* shows the SDO/AIA 171Å image before background subtraction. *Lower panel* shows the SDO/AIA 171Å image after the background subtraction.

the same field of view (see Chapter 3, Fig. 3.1) and take both images at the same time e.g. with respect to the STEREO-A 195Å temporal cadence  $\sim 5$  minutes. To look into the detailed dynamics of the prominence, several movies have been created for (1 - 2 days) so that the prominence activity can be noticed easily in both images at same time. To blow up the changes in faint structures, base difference and running differences/ratio images are also used in the analysis. For finding the exact location of the limb features (SDO) on the solar disk (STEREO-A), we use two methods - plotting the SDO grid lines on the STEREO images, and tie-pointing method (Thompson 2009).

### 2.3.2.1 SDO grid lines on the STEREO images

The structures of the solar atmosphere observed from two different viewing angle (by the SDO and STEREO) are at different locations on the images. One can find the position of structures in the two images, if one knows the separation angle between the spacecrafts. For this, accuracy of the positions between the two viewpoints is very important with respect to the Sun. Therefore we take into account the difference between the two viewpoints and obtain the location of particular features.

First, we obtain the separation angle between both the spacecrafts - SDO and STEREO-A from the STEREO website<sup>11</sup>. For example, (see Fig. 2.8) on 13 February 2011 the separation angle between both the spacecrafts was  $86^\circ$ . This gives an idea that the SDO limb line is at the  $-4^\circ$  on the STEREO-A image (e.g  $86^\circ - 90^\circ = -4^\circ$ ) during our observations. We have applied this method to all the images and over-plotted the SDO grid lines on STEREO-A images. For looking at changes in specific features in the on-disk images, solar rotation has been removed from data set. When this is done to the STEREO-A images, the limb line of the SDO images moves across the solar disk with time. This helps us to find out the prominence position on STEREO-A disk images (see Chapter. 3, Fig. 3.1).

### 2.3.2.2 Tie-pointing method

Another method is tie-pointing (SCC\_MEASURE), which we used to locate the position of solar structures in two different images from the two spacecrafts. The point at which the lines of sight from each spacecraft to the solar feature meet is the tie point. The method which is used to obtain the coordinates is known as tie-pointing method. This method is described by Thompson (2009), who wrote the routine SCC\_MEASURE in the Interactive Data Language (IDL) which is provided in SolarSoft. We used this technique to determine the SDO limb features on STEREO-A disk images. The SCC\_MEASURE display a pair of images from two spacecrafts (SDO and STEREO). It takes the FITS (Flexible Image Transport System format) file as input. Both SDO and STEREO images provides the World Coordinate System keywords and these keywords permit the users to determine the precise position of the feature in image from two spacecrafts (also see other methods Inhester (2006), Aschwanden et al. (2008), Thompson (2009)). The display of the images allow to select a feature on one image (see Fig. 2.11, '+' sign on SDO images), then an epipolar line will display on the other image passing through the same feature as shown in Fig. 2.11.

---

<sup>11</sup><http://stereo-svc.nascom.nasa.gov/where.shtml>

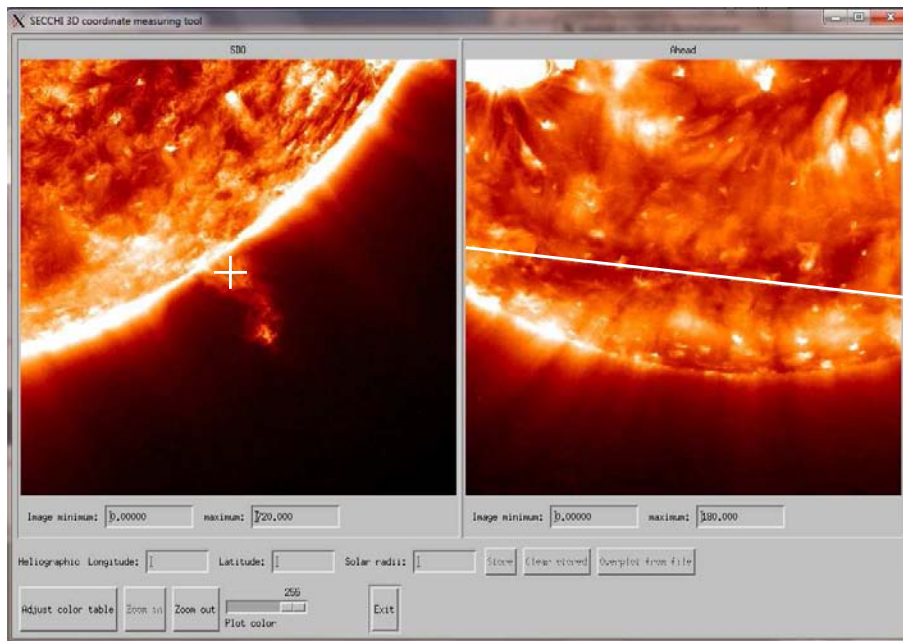


Figure 2.11: *Left panel* is the SDO image. *Right panel* is the STEREO-A image. The white long line is the epipolar line for the prominence position marked with + sign on the SDO image.

In addition to above methods, we have developed several routines (including IDL and SolarSoft) to analyse the SDO and the STEREO data.



# 3 Structure and evolution of a polar crown prominence/filament system<sup>★</sup>

Polar crown prominences are coronal structures of chromospheric plasma partially circling the Sun's poles between 60° and 70° latitude. We aim to diagnose the 3D dynamics of a polar crown prominence using high cadence EUV images of the Atmospheric Imaging Assembly (AIA) from the Solar Dynamics Observatory (SDO) at 304 and 171Å and the Extreme UltraViolet Imager (EUVI) on the Ahead spacecraft of the Solar Terrestrial Relations Observatory (STEREO-A)/EUVI at 195Å. Using time series across specific structures we compare flows across the disk in 195Å with the prominence dynamics seen on the limb. The densest prominence material forms vertical columns which are separated by many tens of Mm and connected by dynamic bridges of plasma that are clearly visible in 304/171Å two-color images. We also observe intermittent but repetitious flows with velocity 15 km s<sup>-1</sup> in the prominence that appear to be associated with EUV brightenings on the solar disk. The separatrix between the prominence and the overlying cavity appears as a sharp edge. We discuss the cause and structure of the coronal cavity seen both above and around the prominence. SDO/Heliioseismic and Magnetic Imager (HMI) and Global Oscillation Network Group (GONG) magnetograms are used to infer the underlying magnetic topology. The evolution and structure of the prominence with respect to the magnetic field seems to agree with the filament linkage model.

## 3.1 Introduction

As their name suggests, polar crown prominence-filament systems create a crown that approximately outlines the polar coronal holes (Hirayama 1985, Tandberg-Hanssen 1995). They form between dispersed active region flux and polar coronal holes. Their position and number changes with the solar cycle (Webb et al. 1984, McIntosh 1992). Starting a few years before solar maximum, the phase in which the reported observations were made, polar crown filaments become more common (Zirker et al. 1997, Minarovjech et al. 1998a). On the disk they appear as rows of dark pillars or vertical columns with intermittent filamentary connections (Lin et al. 2003c, Schmieder et al. 2010, Dudík et al. 2012, Li and Zhang 2013). On the limb, persistent small-scale flows are seen in the cold plasma pillars (Chae et al. 2008, Berger et al. 2008, 2011) that often reside in long-lived

---

<sup>★</sup> A paper on this work has been published in *Solar Physics*: N. K. Panesar, D. E. Innes, D. J. Schmit, S. K. Tiwari, 2014, *Solar Physics*, 289, DOI 10.1007/s11207-014-0504-z, reproduced with permission by Copyright Clearance Center ('CCC')

coronal cavities (Gibson and Fan 2006, Gibson et al. 2010, Habbal et al. 2010, Schmit and Gibson 2011).

One key to understanding the formation of polar crown prominences is the linkage of flux across and between dispersing active regions (Martens and Zwaan 2001, Mackay and van Ballegoijen 2001). Most filaments are found between initially unrelated active regions (Gaizauskas et al. 1997, Martin 1998a, Mackay et al. 2008a) along the magnetic polarity inversion lines (PILs) which separate the regions of opposite polarity magnetic fields (Martin 1973a). It is probable that magnetic reconnections, driven by flows converging to the PIL, play an important role in the filament formation and maintaining the filament mass (e.g. Chae 2003). As new connections are made between the adjacent active regions, open flux regions develop along the outer edges of the original bipoles (Mackay and van Ballegoijen 2006).

Prominences and their on-disk counterparts, filaments, have been thoroughly investigated with imaging and spectroscopic techniques (Labrosse et al. (2010) and references therein). They are relatively cool and dense structures suspended in the hot million degree kelvin corona (Hirayama 1985, Mackay et al. 2010, Labrosse et al. 2010). When observed in chromospheric lines, they appear to consist of two main structures: the spine that runs along the filament channel, and the barbs that project sideways from the spine and connect to the photosphere (Martin 1998a, Aulanier and Demoulin 1998). Often in images of polar crown filaments only the barbs, sometimes known as the filament feet, are visible as dark pillars (Schmieder et al. 2010, Dudík et al. 2012, Li and Zhang 2013). The two main reasons for prominences appearing dark in EUV images is absorption and/or volume blocking (Anzer and Heinzel 2005). Absorption is due to the photoionization of neutral H and He, by the coronal radiation passing through the prominence (Kucera et al. 1998, Heinzel and Anzer 2001, Heinzel et al. 2003). Volume blocking is caused by the presence of cool prominence plasma in a volume of space which does not participate in the emission of coronal lines (Schmieder et al. 2004, Heinzel et al. 2008). Some of the prominence features can also be visible as emission in the 171Å filter (Parenti et al. 2012). Prominences observed in H $\alpha$  and HeII have different morphological features (Wang et al. 1998). In observations, the H $\alpha$  emission coincides with the 193Å absorption because the optical thickness of the prominence observed in the EUV at around 193Å is similar to the optical thickness in the H $\alpha$  (Anzer and Heinzel 2005). Spectroscopic observations of lines formed at transition region and coronal temperatures show plasma streaming through the corona with velocities up to 70 km s<sup>-1</sup> for typically 13 min (Kucera et al. 2003). Such flows would therefore travel a distance of 50,000 km, equivalent to a supergranule cell diameter. One of the outstanding problems is to disentangle structures along the line-of-sight and to see the connections between the cool H $\alpha$  and 304 Å emission and the hot coronal emission.

An important and probably necessary condition for the stability of the prominence-filament system is an overlying coronal arcade above the cold prominence plasma and related coronal cavity (Low and Hundhausen 1995, Hudson et al. 1999a, Gibson and Fan 2006, Heinzel et al. 2008). The arcade is nearly potential field and surrounds both the cavity and the prominence. Most models for the cavity and prominence invoke either a flux-rope (Kuperus and Raadu 1974, Priest et al. 1989, van Ballegoijen and Martens 1989, Low and Hundhausen 1995, Aulanier and Demoulin 1998, Low and Zhang 2002) or a sheared-arcade (Antiochos et al. 1994, DeVore and Antiochos 2000, Aulanier et al.

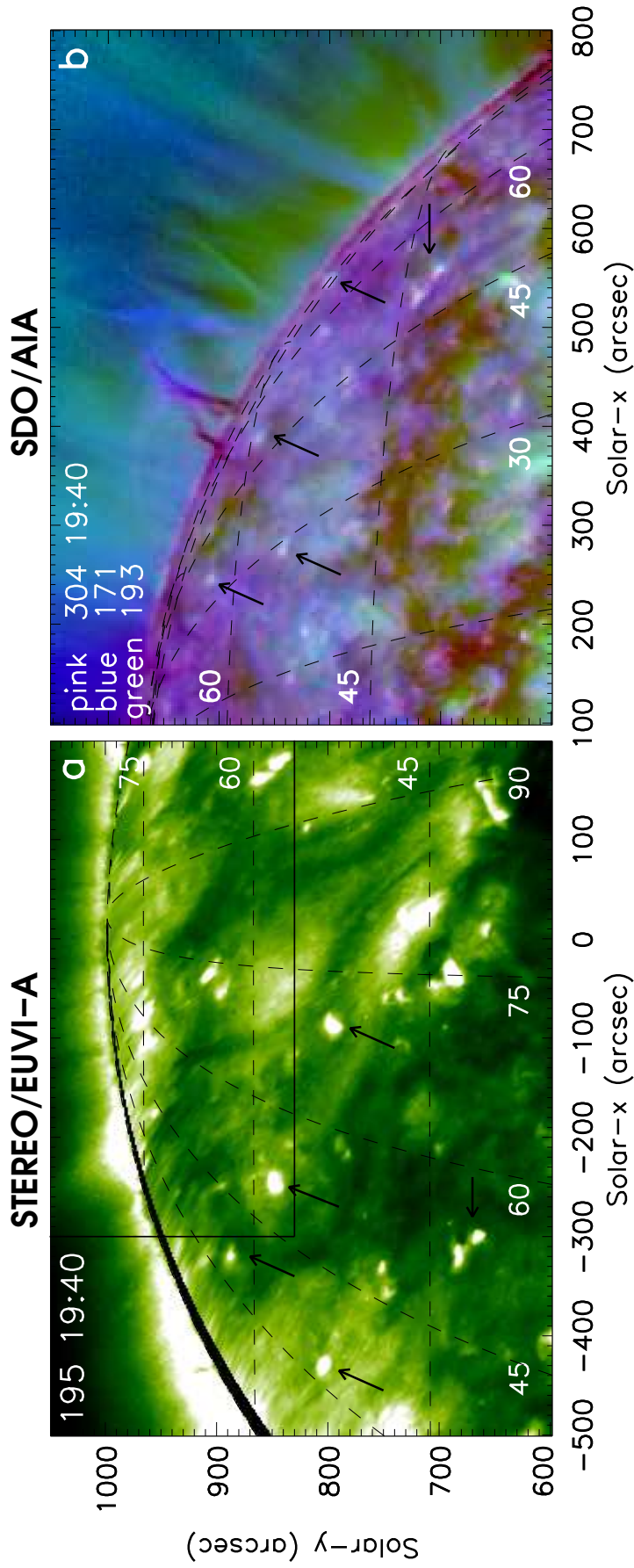


Figure 3.1: a) Prominence-flament system observed on 13 February 2011 (a) STEREO-A 195Å b) SDO (304Å, 171Å, 193Å composite). Arrows point to common brightenings in the STEREO and SDO images. Grid lines are SDO longitude and latitude separated by 15°. The righthand longitude line shows the position of SDO limb. The lowest latitude line 45°. The STEREO image has been derotated to align with disk features at 00:05 UT on 15 February. A black box outlines the region presented in Fig. 3.6.

2002). In these models the dense prominence plasma lies in the dips of the field and the cavity is filled with the surrounding, low-density plasma. Typically the transverse fields of quiescent polar crown prominences are observed to have an inverse polarity with respect to their overlying arcade (Leroy et al. 1984, Anzer 1994, Antiochos et al. 1994, Kuperus 1996). This is consistent with both the flux-rope and sheared arcade models. Coronal magnetic field measurements favour a flux-rope configuration in at least one of the observed polar crown cavities (Rachmeler et al. 2013, Bak-Stęślicka et al. 2013).

The cavity in extreme ultraviolet (EUV) images is sometimes seen on top of cooler prominence material with horns of cooler material outlining the base of the cavity (Régnier et al. 2011, Schmit and Gibson 2013, Panesar et al. 2013, 2014b), and sometimes surrounding the prominence (Berger et al. 2012). From the top, the cavity shows up as a dim region in EUV images (Vásquez et al. 2009).

In the present work, we focus on the dynamics of a small polar crown prominence seen on the north-west limb from Earth using high cadence Solar Dynamics Observatory (SDO) images from the Atmospheric Imaging Assembly (AIA) (Lemen et al. 2012) and near the central meridian in 195Å Solar Terrestrial Relations Observatory Ahead (STEREO-A) images from the Extreme UltraViolet Imager (EUVI) (Howard et al. 2008). The prominence is typical of the many small ones seen at high latitudes. Hazy 171Å emission extends from the top and sides of the main 304Å prominence pillars, into and from which plasma streams along spidery legs. Recently, Su and van Ballegooijen (2012) have also analysed SDO and STEREO quadrature observations to investigate the magnetic structure of a large polar crown prominence-filament system, in the days preceding its partial eruption. Here we use the stereoscopic perspective of SDO and STEREO-A to separate the filament into pillars and interconnecting flows. In particular we are able to use combined 304 and 171Å AIA images to track the flows through the corona, and to find the starting and end points of the flows on the disk. The character of the start and end sites are determined using running difference time-slice images of on-disk emission which show distinctly different behaviour for brightenings, flows, and pillars. Using the two instruments in quadrature, we are also able to investigate the events leading to the appearance of EUV cavities around and over the prominence. To identify the magnetic configurations underlying the prominence, we have used line-of-sight magnetograms obtained by the Helioseismic and Magnetic Imager (HMI) (Schou et al. 2012) and the Global Oscillation Network Group (GONG) (Harvey et al. 1996).

The plan of the chapter is as follows: In Section 3.2, we describe the observations, and give details of the data analysis; In Section 3.3, we first give an overview of the polar crown prominence and the structure of the filament channel. Then we investigate the evolution of the prominence over about 40 hours so as to identify the main prominence pillars in the STEREO-A images. In Section 3.4 we show the flows and velocities in the prominence pillars. Finally in Section 3.5 we present a sketch of the prominence/filament system and relate it to the large-scale magnetic field configuration.



## 3.2 Observations and data analysis

The prominence studied here was seen from Earth (SDO) on the north-west limb of the Sun between latitudes  $60\text{-}70^\circ$  on 13 and 14 February 2011. During our observations, the separation angle between SDO and STEREO-A was  $86^\circ$  (see Chapter. 2, Fig. 2.8) so that the prominence was close to the central meridian in STEREO-A images.

### 3.2.1 SDO/AIA data

AIA provides high spatial resolution ( $0.6 \text{ arcsec pixel}^{-1}$ ) full disk images with a cadence of 12 s in 10 wavelength bands, including seven extreme ultraviolet (EUV), two ultraviolet and one visible filter (Lemen et al. 2012). For the SDO analysis, we select two channels:  $304\text{\AA}$  which is dominated by the HeII lines formed between  $5 - 8 \times 10^4 \text{ K}$  and  $171\text{\AA}$  which is centered on the FeIX line formed around  $6.5 - 8 \times 10^5 \text{ K}$  (Del Zanna et al. 2011, Lemen et al. 2012, Parenti et al. 2012). The prominence flows are best seen in  $304\text{\AA}$  and the overlying hotter plasma and cavity in  $171\text{\AA}$ .

To enhance the visibility of the  $171\text{\AA}$  prominence structure, we removed an average coronal background from the  $171\text{\AA}$  images. The background is computed as the median of two months data - January and February, 2011. This gave a smooth background with intensity decreasing radially outwards from the limb, as well as the correct average angular dependence. The displayed images are the logarithm of the ratio of the images to the background: both taken at the same solar coordinates. We found that this gave better contrast than could be obtained by straight subtraction of the background image, probably because it reflects the relative rather than absolute changes. Two colour images are constructed by combining scaled  $304\text{\AA}$  intensity and  $171\text{\AA}$  background ratioed images. Because the standard AIA colours for 193, 171, and  $304\text{\AA}$  filters are not easy to distinguish in 3- or 2-color images, we have used the green color for 195 and  $193\text{\AA}$ , blue for the  $171\text{\AA}$  and red for the  $304\text{\AA}$  images.

### 3.2.2 STEREO/EUVI data

We have used STEREO-A  $195\text{\AA}$  images with a time cadence of 5 minutes. For most of the analysis the images have been derotated to a particular time and SDO grid lines are superimposed so that the position of the SDO limb can be easily identified. We set the Solar-B to zero only for the on-disk features (STEREO images) because this makes the alignment with the off-limb features easier. Setting solar-B to zero off-limb does not help with the alignment in the prominence features. To relate the  $195\text{\AA}$  images to structures in the filament channel we looked at SDO  $304$ ,  $171$  and  $193\text{\AA}$  images taken one week earlier, 5-9 February, when the prominence appeared as a filament near the central meridian from SDO.

### 3.2.3 SDO/HMI and GONG observations

We also used SDO/HMI magnetograms taken on the 6, 7 and 8 February to look at the magnetic field under the filament channel. HMI provides full disk, line-of-sight magnetograms with a resolution of  $0.5 \text{ arcsec pixel}^{-1}$  and a cadence of 45 s. Since the field was

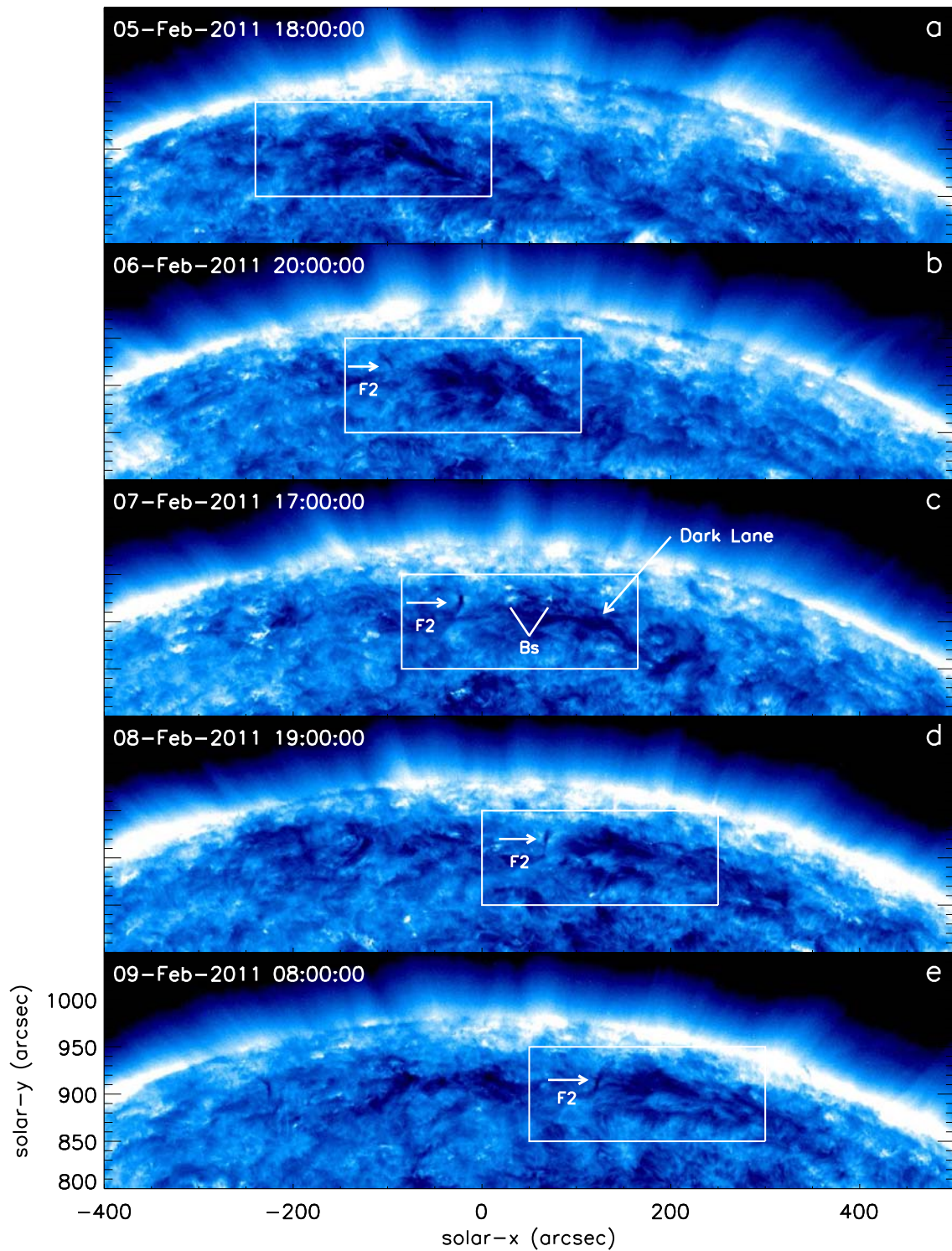


Figure 3.2: Evolution of prominence-filament system from 5-9 February 2011: Sequences of SDO 171Å intensity images showing the growth of pillar F2 and brightenings (Bs) in the filament channel. The white box roughly outlines the region of the filament channel observed on the limb on 13 and 14 February 2011.

very weak, we built up a deep magnetogram for the 6, 7 and 8 February 2011 by averaging 48 coaligned magnetograms taken throughout the day. First, we derotated the images to a particular time, then we took the average of all the images to enhance the polarities in the HMI magnetograms. This enhanced map is used to identify the polarities which are involved in the prominence system.

The GONG synoptic maps are  $360^\circ$  magnetograms of the Sun available from the GONG website as hourly fits files. We have co-aligned magnetograms for 17 January 2011 and 13 February 2011 to  $360^\circ$  STEREO-SDO composites of the  $195/193 \text{ \AA}$  EUV emission at those times. This provides an estimate of the large scale magnetic field structures during the observation and one solar rotation earlier.

### 3.3 Overview

The small polar crown prominence-filament system, as seen from the two viewing angles at 19:40 UT on 13 February 2011, is shown in Fig. 3.1. Grid lines are the same in both images and the SDO limb is the right hand dashed line on the STEREO image. The SDO overview image shown here includes the  $193 \text{ \AA}$  as well as the  $304 \text{ \AA}$  and  $171 \text{ \AA}$  in the composite because the brightenings, used as markers, are much more visible when the  $193 \text{ \AA}$  emission is included. Several of the common brightenings are indicated with arrows. The brightenings east of the  $60^\circ$  grid lines are clearly identifiable in both STEREO and SDO, but those closer to the limb are partially obscured in the SDO image due to the column of intervening gas along the line-of-sight. The prominence which lies between  $60\text{-}75^\circ$  latitude is difficult to see in the disk image. We have outlined the filament channel region with a black box. Several dark structures in the filament channel are just discernable. The cold plasma should be dark in the  $195 \text{ \AA}$  disk image due to absorption/blocking of EUV emission by the cold, neutral gas (Anzer and Heinzel 2005). However the darkening due to prominence material can easily be confused with darkening caused by a coronal cavity or regions of low coronal density in the filament channel. We therefore looked at the filament channel in the SDO images from 5-9 February 2011 to distinguish the various structures.

#### 3.3.1 Structure of the filament channel

The structure of the filament channel when it was on the disk is illustrated in Fig. 3.2 and Fig. 3.3, which show one SDO  $171 \text{ \AA}$  and one  $193 \text{ \AA}$  image per day from 5-9 February. By comparing the two, we could identify features of the filament channel, that were clearly visible at  $171 \text{ \AA}$ , in  $193 \text{ \AA}$  images, and thus better interpret the  $195 \text{ \AA}$  STEREO images. The filament plasma is seen most clearly in the  $171 \text{ \AA}$  images. The white box highlights the part of the filament channel that we have analysed, when it appeared on the limb. The filament channel shows a slowly evolving broad, dark lane in  $171 \text{ \AA}$  images (Fig. 3.2). On the 6 February, a pillar (marked F2) appears which, by tracking its motion across the disk, we have identified as one of the pillars that was seen on the SDO limb and the STEREO disk on 13 and 14 February (Figs. 3.6 and 3.11). We also observed a region with multiple small-scale brightenings (see Fig. 3.2c) just north of the main filament plasma. These brightenings were seen simultaneously in the  $193 \text{ \AA}$  images (Fig. 3.3c). At  $193 \text{ \AA}$  a

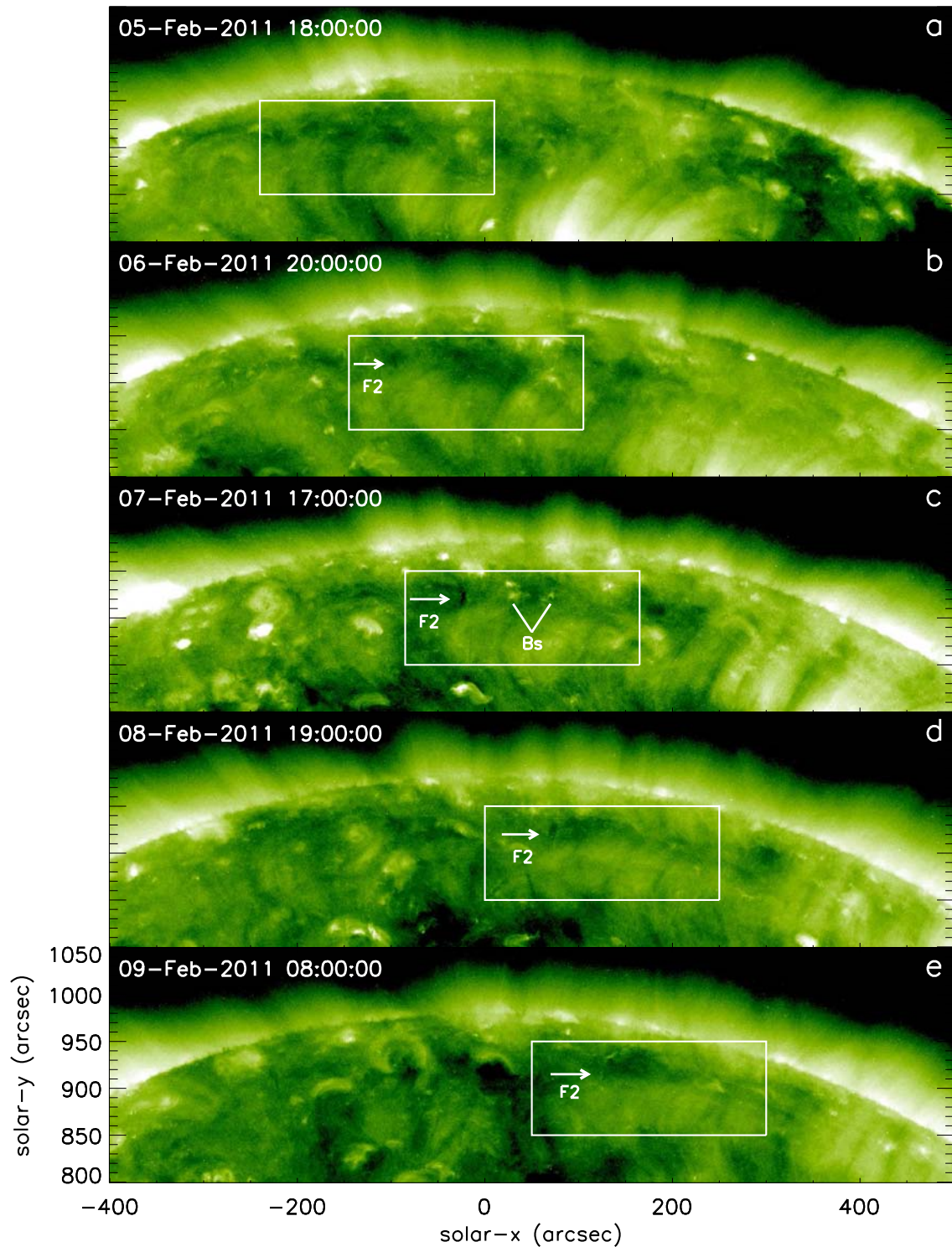


Figure 3.3: Evolution of prominence-filament system from 5-9 February 2011: Sequences of SDO 193Å intensity images showing the pillar F2 and brightenings (Bs) in the filament channel. The prominence-filament system taken at the same time as Fig. 3.2. The white arrows point to the pillar F2, brightenings (Bs).

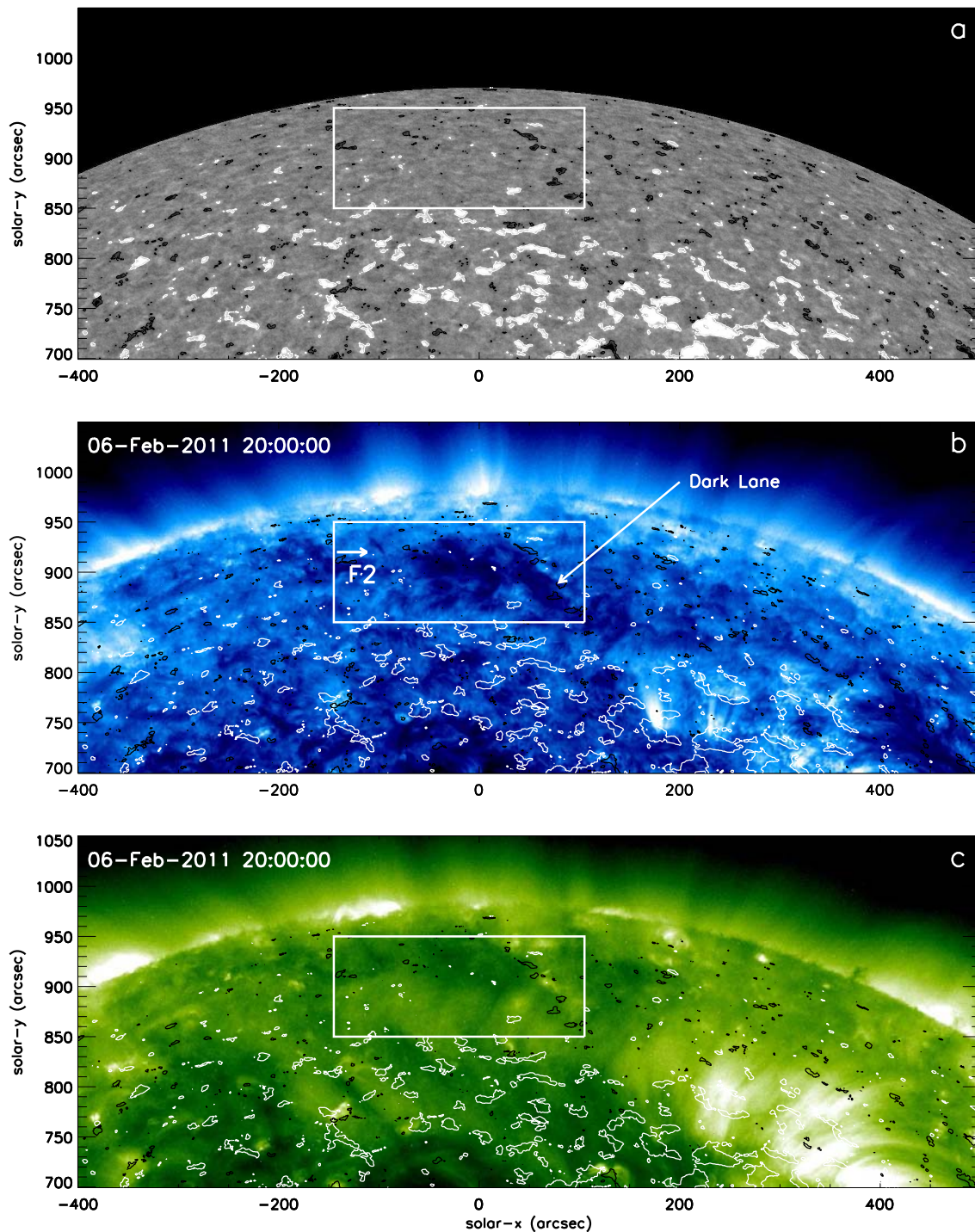


Figure 3.4: Magnetic field structure on 6 Feb 2011: a) SDO/HMI 6301Å averaged magnetogram overlaid with contours of  $\pm 8$  Gauss; b) and c) SDO/AIA 171 and 193 Å intensity image with the overlaid with the same magnetic field contours. The pillar F2 is indicated with an arrow.

notable feature is a region of reduced 193Å emission. It is best seen in the 193Å image (in Fig. 3.3b) and appears between the three brightenings in Fig. 3.3c. By looking at the five-day sequence of 193Å images, we saw that this region was visible throughout the 7

and 8 February. When the filament channel was on the SDO limb, a pronounced region of reduced  $195\text{\AA}$  emission was visible in the STEREO images at roughly the same position with respect to the pillar. As discussed later, we believe this is associated with the coronal cavity.

Fig. 3.4a represents the SDO/HMI map of the average line-of-sight magnetic field on the 6 February 2011. A white box in Fig. 3.4a, b and c outlines the region of the filament channel investigated. On the whole, the filament channel coincides with a region of very low magnetic flux. Diffused active region positive flux is distributed to the south of the filament channel and smaller concentrations of negative flux are found on the north and west of the channel (Fig. 3.4b,c). From Fig. 3.4b we can see that the pillar F2 forms between the negative and positive magnetic flux. A similar pattern of low magnetic flux in the filament channel has been observed on 7 and 8 February.

To study the reduced emission seen in  $193\text{\AA}$  of the filament channel, we have investigated the STEREO-B images from 5-9 February when the filament channel was on the STEREO-B limb. We noticed that the cavity was clearly visible for 2 days throughout the period. Fig. 3.5 shows the cavity structure on the north west solar limb. It was clearly visible on 6 February (see Fig. 3.5, cavity is pointed by an arrow). On 7 February, it is not clearly visible because it moved a little bit beyond the limb. From STEREO-B images it seems that the dark part in the filament channel at  $193\text{\AA}$  (Fig. 3.3) is the coronal cavity and it appears dark due to the less density plasma. To confirm the cavity position in the SDO images, we obtained the three-dimensional coordinates of the prominence cavity with the routine `SCC_MEASURE` (Thompson 2009) available in the SolarSoft library.

### 3.3.2 Footpoints of the prominence

In Fig. 3.6 STEREO-A  $195\text{\AA}$  and SDO  $304\text{\AA}/171\text{\AA}$  composites taken at the same time on 13 February are shown. In the SDO images cool plasma (brown) on the limb is often connected through the corona with warmer  $171\text{\AA}$  filaments (blue). With the combination of two wavelengths we can see the connections through the corona as well as dark cavities above the prominence.

We derotated the STEREO images to 13 February at 00:05 UT, so that the SDO limb position, shown as a meridional dashed line, moves on the STEREO image with time. Identified features are indicated on Fig. 3.6. Arrows on the images at 06:00:30 UT point to the three main pillars (F1, F2, F3) and a site, B1, of several brightenings. The pillar, F1, is clearly visible at 06:00:30 UT in the STEREO images, but not in the 12:00:30 UT image. The sites of frequent brightening, B2, B3, and B4, are indicated in the 12:00:30 UT images.

To investigate the on-disk dynamics, we created time series of the emission along a few horizontal slices in the STEREO images. The positions of the time slices are shown as horizontal lines in the top-left frame of Fig. 3.6. The long dot-dashed line cuts across pillar F1 on the right, the filament channel, and the complicated section of connected pillars (F2, F3, F4). In Fig. 3.7a and b, we show the time evolution of these features as seen in STEREO  $195\text{\AA}$  intensity and running-difference time-distance images. In this representation, prominence pillars appear with a criss-cross pattern as cold plasma moved into and out of the pillars. The filament channel, which appears dark in the  $195\text{\AA}$  images, shows almost no variation except at its edge, B2, where there were continual small-scale

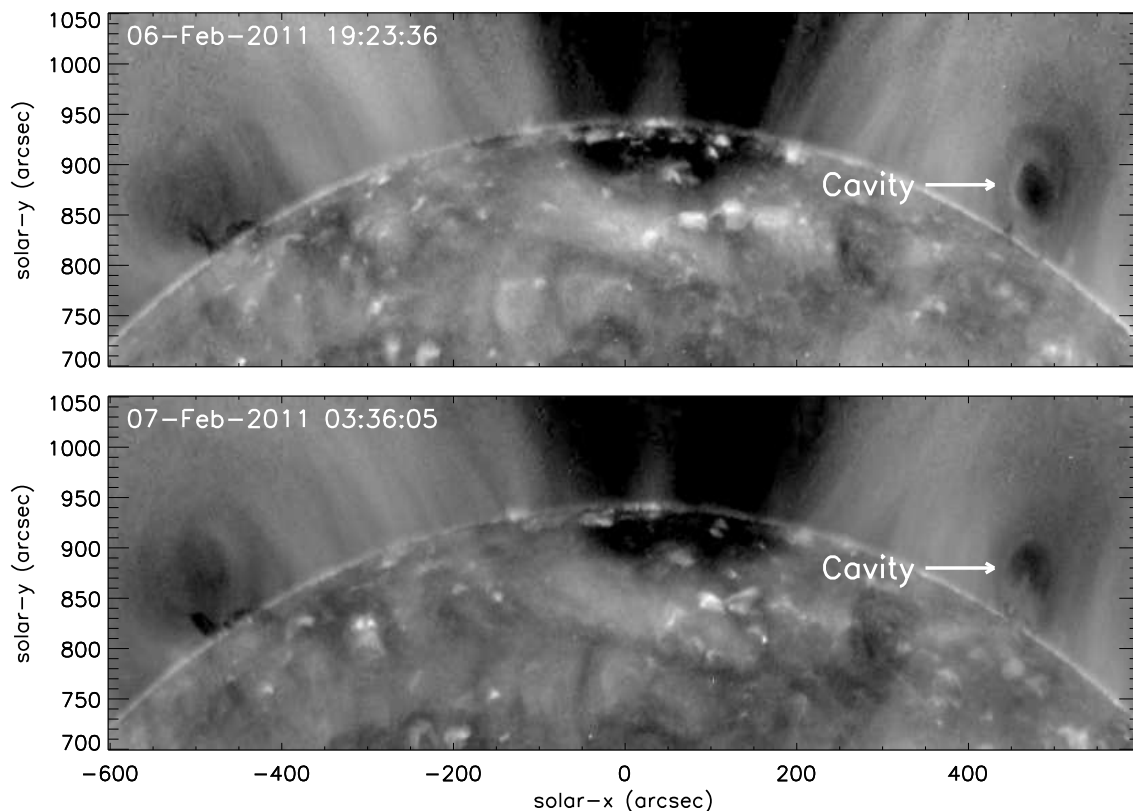


Figure 3.5: The cavity structure on 7 and 8 Feb 2011: STEREO-B 195Å intensity images. The cavity is on the north west solar limb (indicated with an arrow).

brightenings. There were several weak fronts coming from brightening B2 and moving left towards the direction of pillar F2. The white line indicates the position of one of the weak fronts which was moving with a velocity of about  $15 \text{ km s}^{-1}$ . We note that there were no fronts moving in the other direction from B2 into the filament channel, suggesting that these two regions were magnetically disconnected.

At F1 there is both the criss-cross pattern and continuous brightening until about 09:00 UT. At 09:00 UT a strong brightening (marked B4 in the image at 12:00:30 UT) appears below F1, further south from which 171Å emitting plasma is ejected into the corona. Fig. 3.8 shows the 195 Å STEREO-A timeseries image along the dotted line through brightening B4 and pillar F1. We observed the weak flows from B4 to F1 and strong upflows from pillar F1 until the pillar disappears.

We noticed from the SDO movie that plasma rising up and abruptly stopping at the dark edge of a coronal cavity (marked in the 12:00:32 UT image). On 13 February the cavity is visible on the top of the prominence in 171 Å images not in 193 Å images (see Fig. 3.12). The two-colour images show that the flows are a combination of 171 and 304Å emitting plasma, with the chromospheric (304Å) emission lower down and leading directly into the 171Å emission higher in the corona. Thus the brightenings at B4 seem to be associated with plasma heating and flow along a flux tube connecting F1 to F2. The change from 304 to 171Å emission can be due to plasma heating along the flux tube or delayed ionization of previously heated plasma. This will be investigated in a later study focussing on the thermal structure of the prominence plasma. The flows and

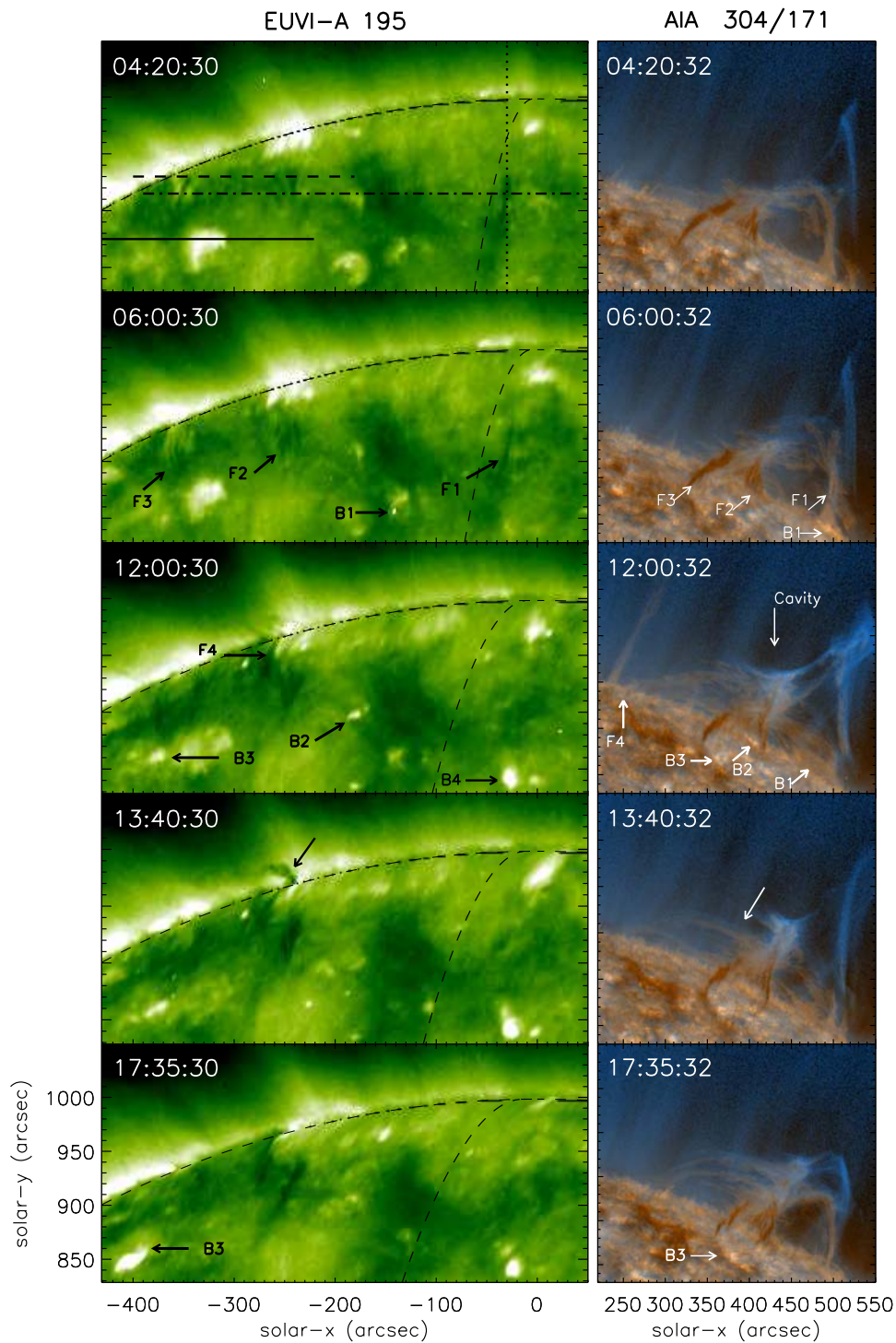


Figure 3.6: Time evolution of prominence-filament system on 13 February: (left) STEREO-A 195Å intensity images derotated to 00:05 13/02/2011 UT; (right) corresponding two-color SDO 304Å/171Å images. The SDO limb is marked with a dashed line on STEREO images. In the top left panel, the horizontal dot-dashed line shows the position of a cut through the pillars (Fig. 3.7) and the horizontal dashed line the cut along the spider feature (Fig. 3.9), the horizontal solid line the cut along the brightening near to the main pillar (Fig. 3.10) and the vertical dotted line the cut along the brightening B4 and pillar F1 (Fig. 3.8). The Y-axis is the same in both SDO and STEREO images.



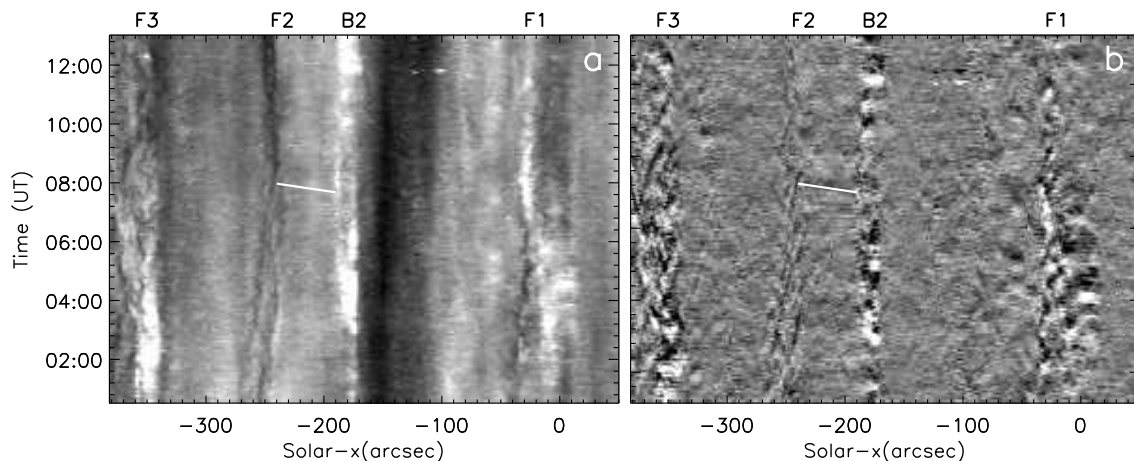


Figure 3.7: a) STEREO-A 195 Å intensity time series and b) running difference time series along the dot-dashed line in Fig. 3.6 on 13 Feb 2011. F1, F2 and F3 are the positions of pillars. The white diagonal line indicates the feature between B2 and F2 where we calculate the velocity.

associated brightenings at B4 are seen throughout the 13 February until about 13:00 UT on the 14 February (Fig. 3.11 at 07:25:32 UT, shown by an arrow F1). The structure of the emission associated with the flows is interesting because the prominence plasma must have stretched over about 150 arc seconds towards the east to connect to the pillar F2. This distance is about three times the line-of-sight distance travelled by the coronal flows seen in the spectroscopic observations of prominences analysed by Kucera et al. (2003).

Additional flows from the top of the prominence out to the north started at 11:44 UT, creating a spider-shaped prominence (Gilbert et al. 2001) with flows on either side of the main prominence pillar. Here the flows were going in one side (south) and out the other (north). From the SDO images it looks as though the outflows were triggered by the inflows from the south. Possibly a pressure increase from the inflowing plasma in the vicinity of a flux-rope dip is sufficient to drive plasma out of the dip along a northern extension of the flux-rope. These flows were associated with the generation of a new dark pillar in the STEREO images (in Fig. 3.6 marked as F4 on the 12:00:30 UT image). A time-series cut through this spider-shaped feature on the STEREO images (horizontal dashed line in Fig. 3.6) is shown in Fig. 3.9. The criss-cross flows after 11.30 UT (marked with a white line in Fig. 3.9a,b) are caused by the spider activity.

The solid line cut is through the bright region B3 below F2 and F3. The time evolution along this cut is shown in Fig. 3.10a,b. We notice the strong brightenings throughout the 13 February (Fig. 3.10b). Early on 14 February, an eruption occurred near this position, B3, and led to the coronal dimming.

### 3.3.3 Evolution on 14 February

The evolution of the prominence on the 14 February is shown in Fig. 3.11. During this day, two important things occurred. The first was a small eruption at B3 leading to cavity dimming over a significant portion of the filament channel, and the second was the breaking of the connection, F1-F2.

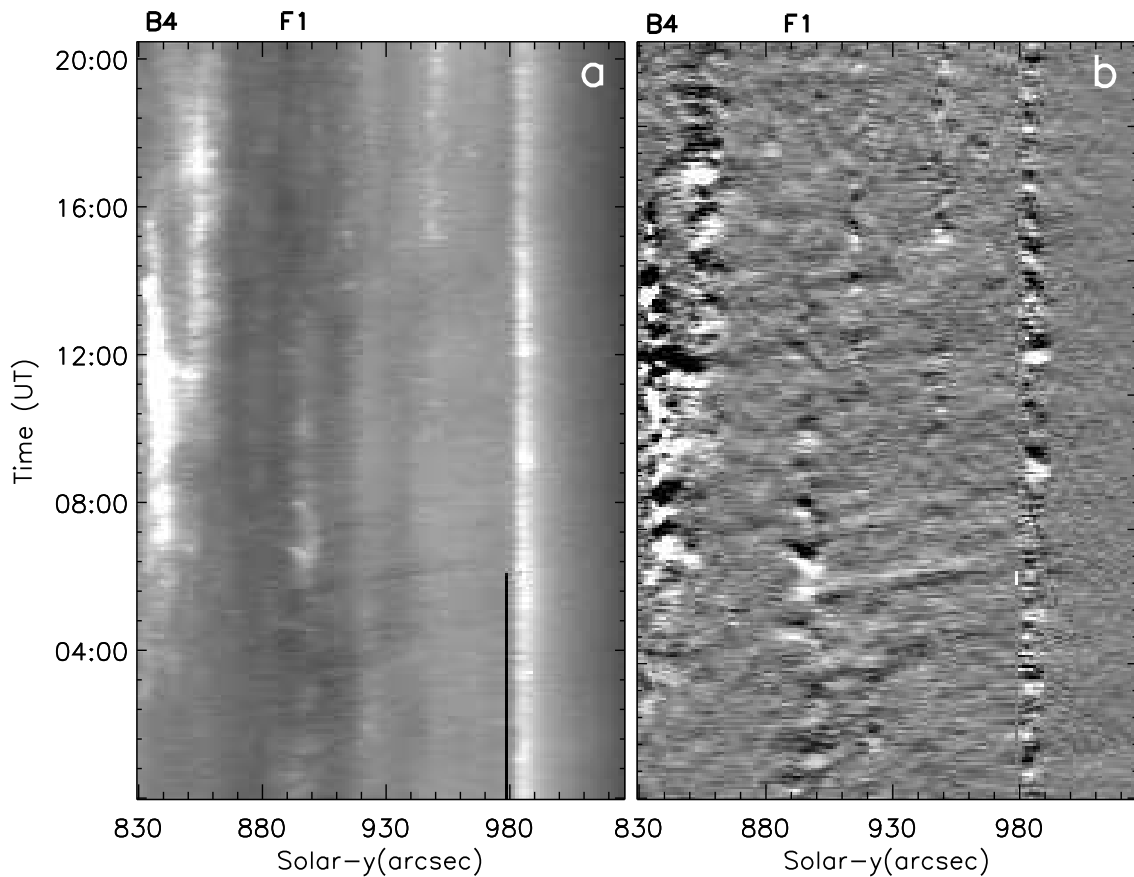


Figure 3.8: a) STEREO-A 195 Å intensity time series and b) running difference time series along the dotted line shown in Fig. 3.6 on 13 Feb 2011. The position of the brightening B4 and the pillar F1 are marked on the top.

### 3.3.3.1 Eruption leading to cavity dimming

The eruption, shown in Fig. 3.13, occurred around 01:00:30 UT on 14 February. This was not a filament eruption but an eruption associated with multiple brightenings seen in 304, 171, 193Å, and jets of chromospheric material in the filament channel. As seen from STEREO, the eruption produced a small EUV wave with a bright front, followed by a dimming that swept over the footpoints of the prominence pillars, F2, F3, and F4. The eruption can be clearly seen in the base difference STEREO image, Fig. 3.13. From SDO, the eruption was seen on the limb as a bright line along the prominence footpoints (Fig. 3.11, top right, B3) ejecting small jets of chromospheric plasma low down in the filament channel. Although the eruption was not associated with a big change to the filament structure, it caused obvious dimming at 193Å in the filament channel (Fig. 3.12). Later the dimming was visible in the 171Å coronal images on either side of the prominence. At the end of the day (17:45:32 UT) the dimming has filled the prominence cavity. In these images, the cavity, starting from the photosphere is visible, not just the region on top of the prominence (Fig. 3.12). In the 171Å images (Fig. 3.6), rather than the cavity itself being visible, we see the enhanced emission from its southern edge. We think that eruption and associated wave heated the cavity plasma and compressed the plasma along the

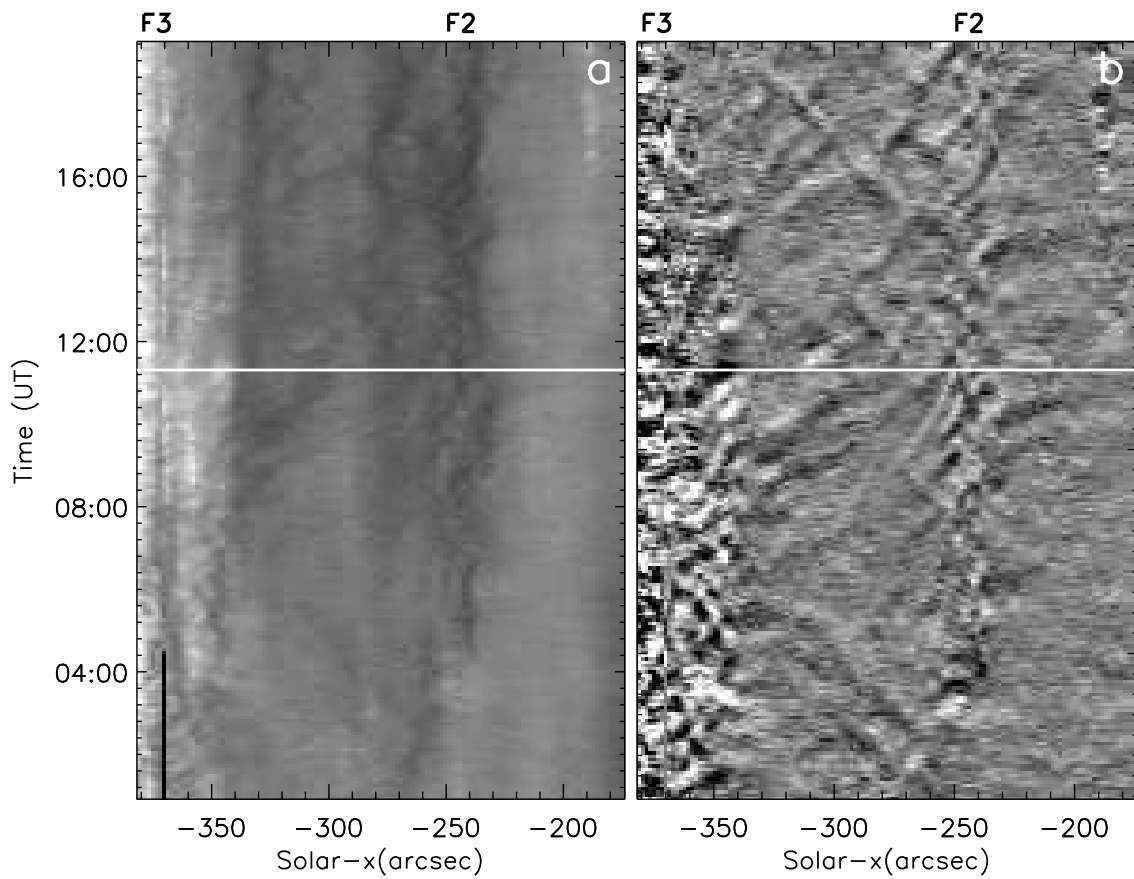


Figure 3.9: a) STEREO-A 195 Å intensity time series and b) running difference time series along the dashed line shown in Fig. 3.6 on 13 Feb 2011. The white line represents the time (11:45) when the spider-shaped prominence is observed. F2 and F3 are the positions of pillars.

cavity edge. Later the cavity was seen as a region of enhanced 193Å emission suggesting that the heated plasma cooled to about 1.5 MK (Fig. 3.12). The cavity remained visible in 171Å for at least two days, before it rotated around the limb.

### 3.3.3.2 Breaking of filament

Shortly after, the connection between F1-F2 broke, a brightening appeared in the filament channel (Fig. 3.11). We find no signature of the brightening in the SDO 304, 171 Å images close to the limb (see Fig. 3.11 at 12:55:30 UT). This indicates that the brightening was beyond the limb (in SDO images) and occurred in the chromosphere. It is interesting that when the connection between F1-F2 broke, the prominence pillar increased in height and the boundary to the coronal cavity above the prominence faded (Fig. 3.11 at 17:45:30 UT).

## 3.4 Flow patterns in the prominence

To analyse the flows in the prominence, we investigate the velocities of the up- and down-flows at different sites. Fig. 3.14a shows an SDO 304Å image when the southern leg was

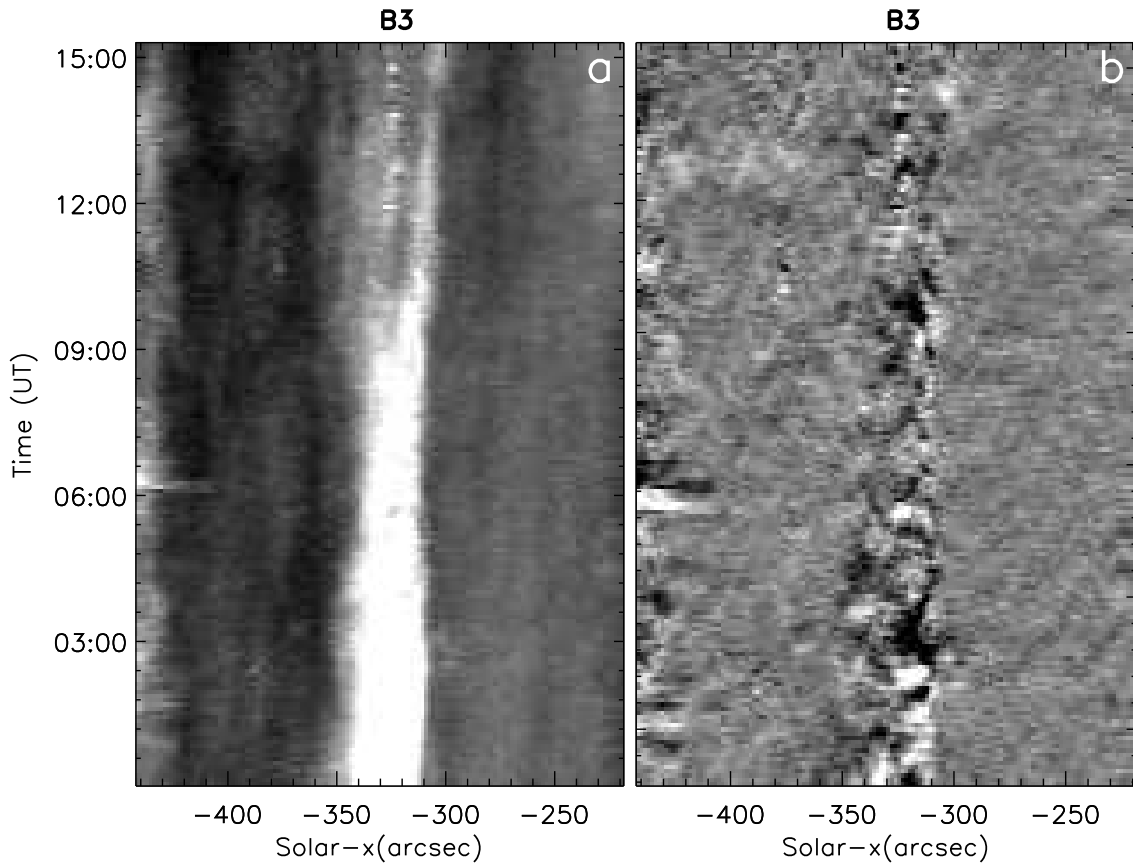


Figure 3.10: a) STEREO-A  $195 \text{ \AA}$  intensity time series and b) running difference time series along the solid line shown in Fig. 3.6 on 13 Feb 2011. A site of brightening, B3, observed near the base of pillar F2 and F3 is marked on the top.

prominent. A black vertical line shows the position of the running difference and intensity time series shown in Fig. 3.14b,c. In Fig. 3.14c, some of the stronger upflows are marked with red lines. Their average velocity comes out to be  $15 \pm 1.0 \text{ km s}^{-1}$ . Similar patterns of upflow have been observed on 14 February at pillar F1. In Fig. 3.15, we show the SDO  $304 \text{ \AA}$  intensity image on 14 February. A vertical line on the pillar F1 represents the position of time series image shown in Fig. 3.16. The long white arrow in Fig. 3.16 pointed the strong upflow along the pillar F1. We also track the bulk of plasma for 50 minutes (pointed with small arrow in Fig. 3.15) in the pillar F1. The average velocity of the bulk of plasma is  $11.5 \pm 1.0 \text{ km s}^{-1}$  which is shown in Fig. 3.17. We observed that in the beginning velocity increases gradually, when the bulk of plasma reaches up to certain height, its speed starts decreasing. At the end, this plasma goes to the main prominence pillar. These upflows seem to have been driven by heating at footpoint of the pillar F1. We observe continuous brightening at F1 from the STEREO  $195 \text{ \AA}$  running difference time series image (see Fig. 3.7b) on 13 February and an increase in  $171/304 \text{ \AA}$  intensity as the plasma moves upwards. According to the injection model (Mackay et al. 2010) heating may drive the plasma upward.

We take a cut along the pillar F2 and F3 as shown in Fig. 3.14d. Fig. 3.14e,f represents the SDO  $304 \text{ \AA}$  intensity and running difference time series image from 14 February

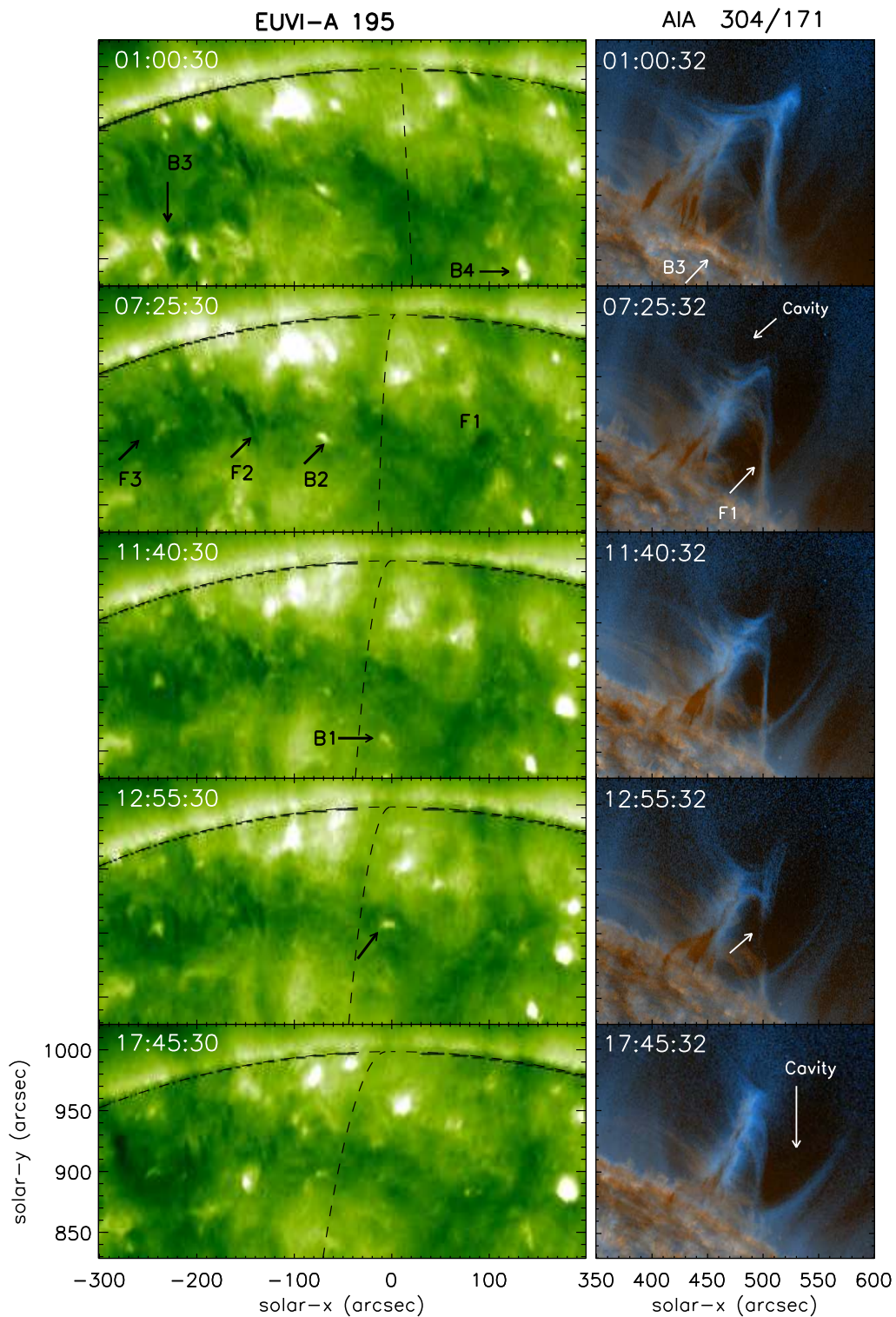


Figure 3.11: Evolution of the prominence-filament system on 14 February: (left) STEREO-A 195Å intensity images derotated to 12:05 14/02/2011; (right) corresponding two-colour SDO 304Å/171Å images. Annotated features are same as those in Fig. 3.6. At B3 there is an eruption seen in both SDO and STEREO images that leads to a coronal dimming. The southern pillar breaks at 12:40 UT. An arrow points to a brightening on the disk at 12:55 UT.

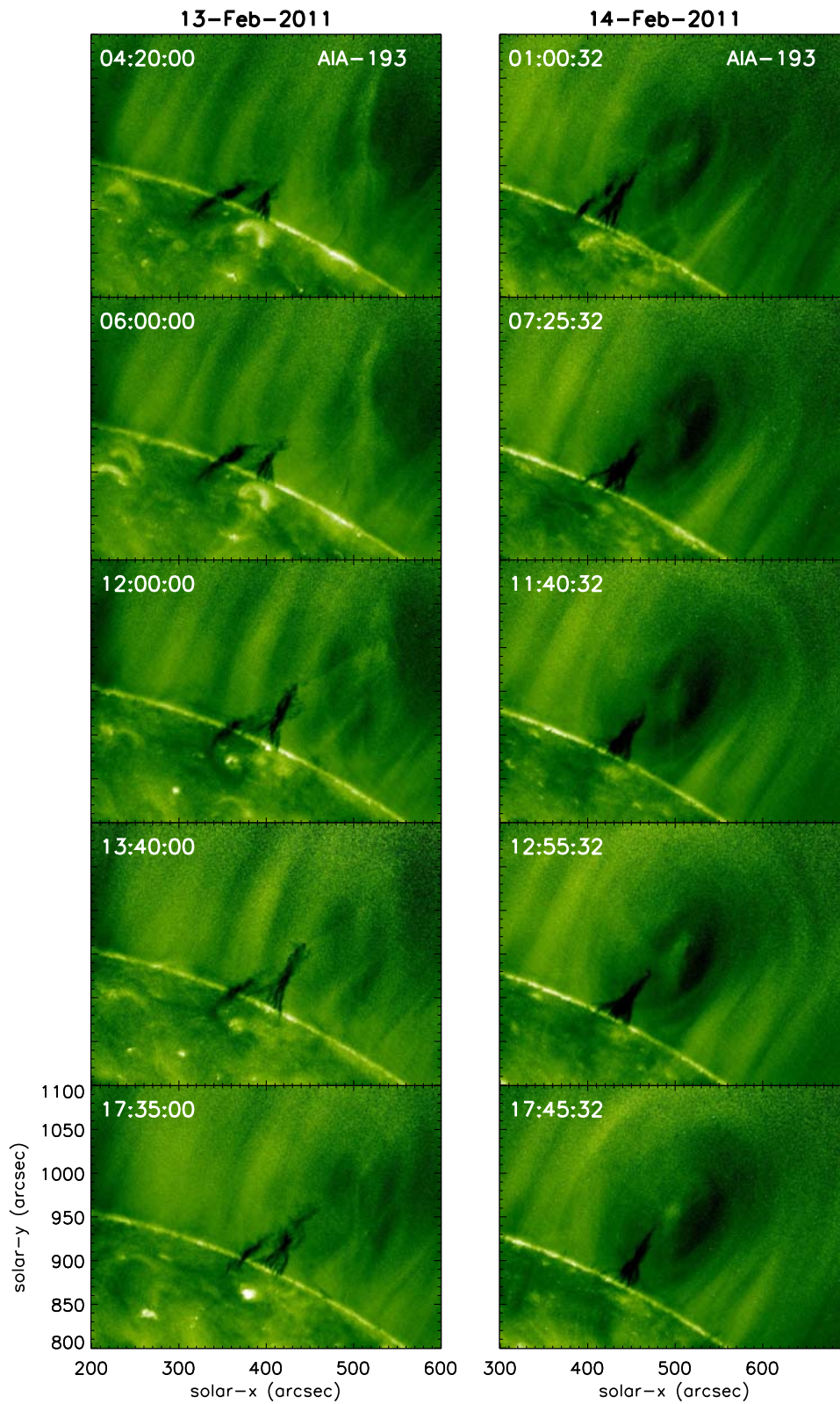


Figure 3.12: Evolution of the cavity system on 13 and 14 February seen in SDO/AIA 193 Å images.

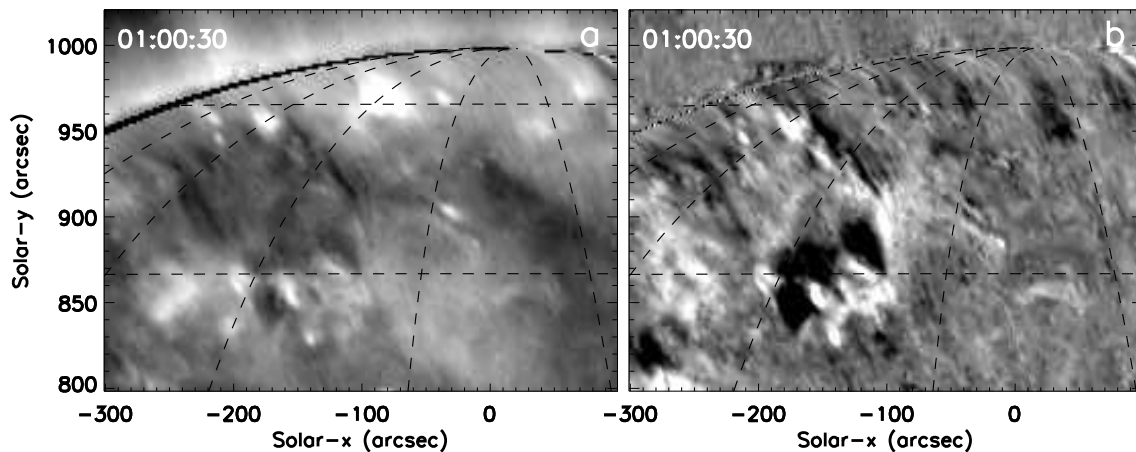


Figure 3.13: Eruption on 14 February 01:00 UT. a) STEREO 195Å intensity image; b) STEREO 195Å base difference image overlaid with SDO grid lines. The righthand longitude line shows the position of SDO limb. Grid spacing is 15 degree. STEREO image has been derotated to 15 February at 00:05.

along the diagonal arrow shown in Fig. 3.14d. The main flows in the pillars F2 and F3 were downward towards the solar surface. The average downflow velocity was  $15.5 \pm 1.5 \text{ km s}^{-1}$ . The dark streaks in the image represents the downflows highlighted with red lines. These downflows seem to be result of cooling and condensing of chromospheric plasma and coming down due to gravity (Dahlburg et al. 1998). Small-scale upflows were also present but for very short time periods.

We also calculated the velocity of the falling plasma from the pillar F2 and F3. Fig. 3.18 shows the SDO 304Å intensity images from the 14 February at different times. The small white arrow pointed the position of the plasma which is moving away from the prominence pillars. Total observation of this activity is 21 minutes from 01:52 to 02:13, we track the plasma at three minute intervals (Fig. 3.19). The plasma is moving away from the pillar with an average velocity of  $25.5 \pm 1.0 \text{ km s}^{-1}$ .

## 3.5 Discussion

We have investigated the structure and dynamics of a polar crown prominence observed in the northern hemisphere on 13-14 February 2011 seen simultaneously at the limb from SDO and at disk center from STEREO-A. The observations were made during the rising phase of the solar cycle when there was no obvious major polar coronal hole in either the SDO or the STEREO images of the northern pole. We have identified three main pillars (vertical columns) of prominence plasma and four sites of persistent brightenings. Using time-series of STEREO on-disk images we deduce that the pillars are separated by hundreds of arcsecs and connected by flows along the filament channel. During the two days studied, we noticed that microflaring (marked as B4 in Fig. 3.6) produced 171Å prominence flows that rise up and stop abruptly at a sharp concave edge in the corona. We speculate that this edge represents a change in the magnetic connectivity and outlines the separatrix layer between the cavity and the prominence.

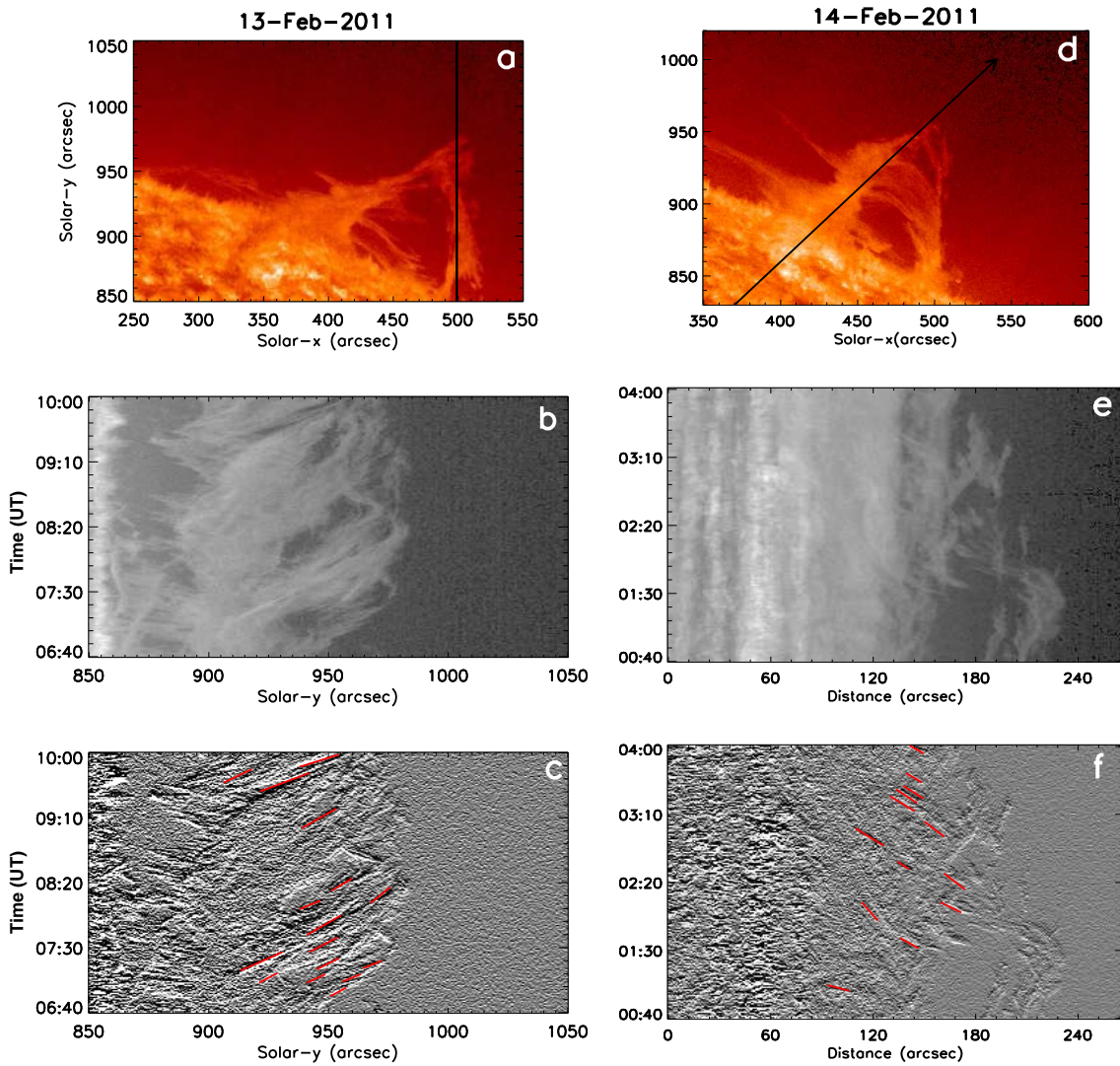


Figure 3.14: Prominence flows: a) SDO 304 Å intensity image from 13 February at 08:20 UT. The vertical black line indicates the position of time series in Fig. 3.14b,c; b) SDO 304 Å intensity time series and c) running difference time series along the line in Fig. 3.14a on 13 February - red lines indicate the upflows; d) 304 Å intensity image from 14 February at 01:40 UT. The arrow indicates the position of time series in (e) and (f); e) SDO 304 Å intensity time series and f) running difference time series showing dominant downflow in pillars along the arrow in Fig. 3.14d - red lines indicate the downflows .



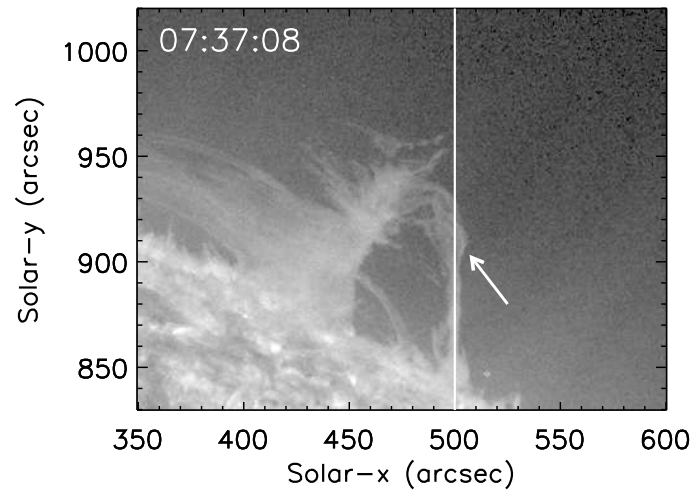


Figure 3.15: Prominence flows: a) SDO 304 Å intensity image from 14 February at 07:37 UT . The vertical line indicates the position of time series in Fig. 3.16 .

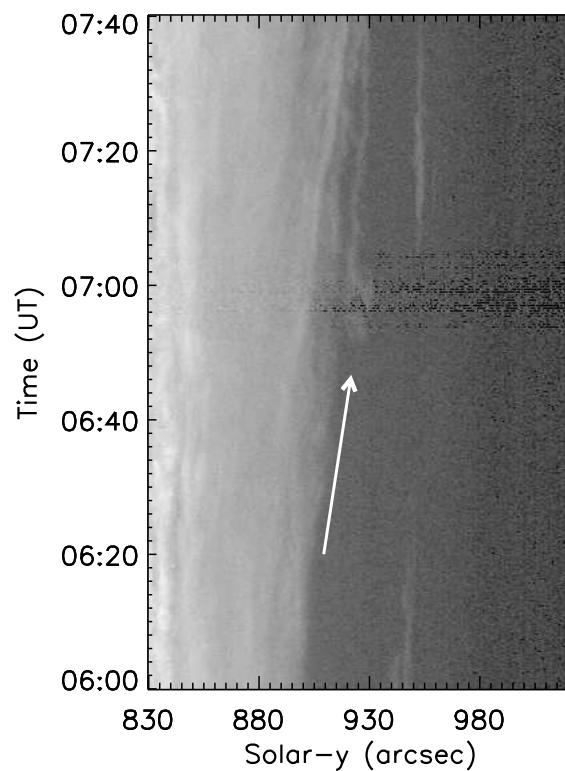


Figure 3.16: Prominence flows: SDO 304 Å intensity time series image along the vertical line in Fig. 3.15 on 14 February - long black arrow indicate the upflows .

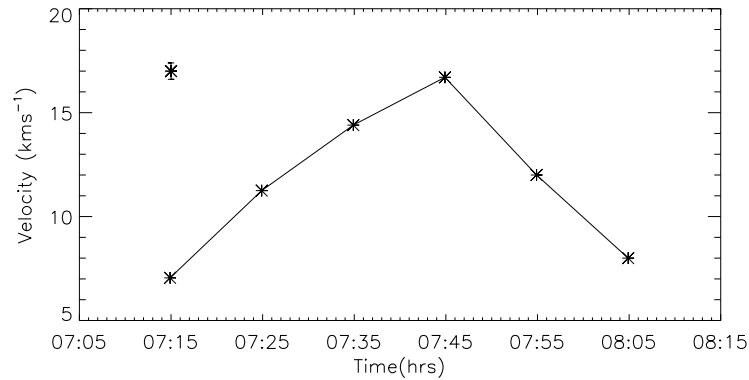


Figure 3.17: Velocity plot: The velocity pattern of the bulk of plasma in the pillar F1 along the line in Fig. 3.15 on 14 February. A common error bar is shown in the upper left corner of the plot .

The central body of the prominence contained stable pillars of cool material, seen suspended above the limb with moderate downflows of  $15.5 \pm 1.5 \text{ km s}^{-1}$ . Our estimations of velocities are in agreement with that of Berger et al. (2008), for a different quiescent prominence. These velocities suggest that prominence flows are moving approximately with the sound speed ( $\sim 10 \text{ km s}^{-1}$ ) and less than the Alfvén speed ( $\sim 30 \text{ km s}^{-1}$ ). The present observations support the model of van Ballegooijen and Cranmer (2010). According to this model, tangled magnetic field is located in the dense vertical pillars so that the plasma is essentially trapped.

One of the motivations for this study was to observe and study the dynamics of a prominence-cavity system. Initially, the cavity was visible as a concave, bowl-shaped dimming in  $171\text{\AA}$  emission above the prominence. It was particularly noticeable when there were flows between pillars F1 and F2. When the connection between the two main pillars, F1 and F2, broke, the magnetic field in the prominence-filament system reconfigured and the prominence increased in height.

The dark cavity region seen in SDO coincided with a dark region close to the filament channel, in the STEREO disk images. Unlike regions of the channel with dense, prominence plasma, this darker region did not show signs of flows in the STEREO time-series. We therefore predict that the darkness was due to its low density, rather than cool prominence plasma and that it is the disk signature of the prominence cavity. We found a similar region of reduced  $193\text{\AA}$  emission at approximately the same position in the SDO images when the prominence/filament channel was on the disk from SDO. In both the STEREO and the disk SDO images, persistent brightening was seen along the edge of this region of reduced  $195/193 \text{ \AA}$  emission.

The presence of the cavity also became apparent after a small flare-like brightening and EUV wave inside the filament channel at 01:00:30 UT on 14 February. This caused a coronal dimming that was immediately visible in the STEREO images and then later as an elliptical coronal dimming surrounding the prominence (e.g. Gibson and Fan 2006) in the limb EUV images. After several hours the region was visible as an ellipse of enhanced  $193 \text{ \AA}$  emission. It remained as a visible cavity in  $171\text{\AA}$  until the region rotated around the limb. We therefore find two configurations that make the cavity visible in EUV images.

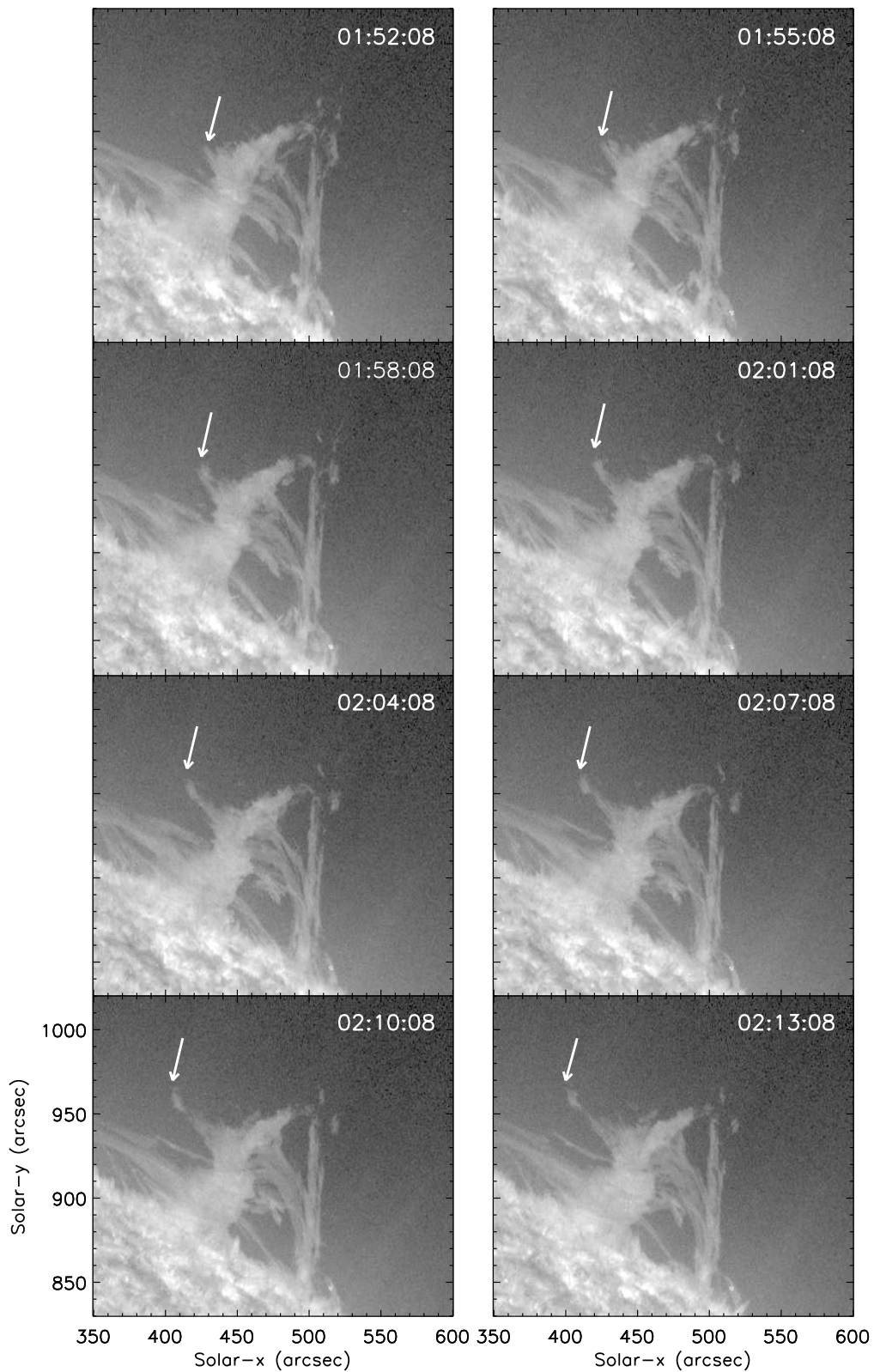


Figure 3.18: Prominence flows: SDO 304 Å intensity image from 14 February. The small arrow points the prominence plasma which is moving away from the main prominence pillar. The velocity pattern of the falling plasma is shown in Fig. 3.19 .

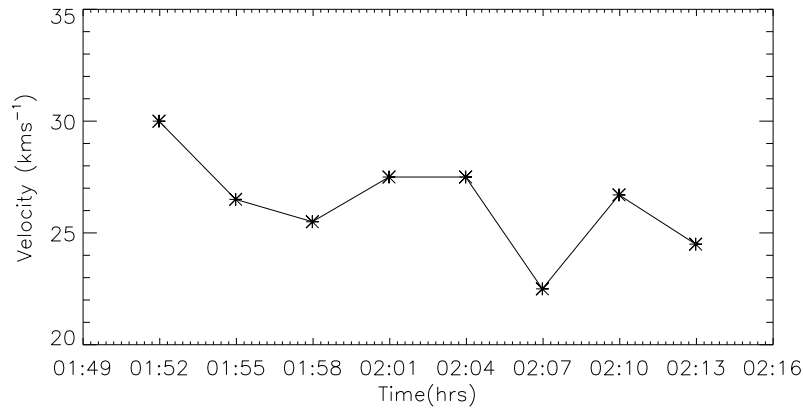


Figure 3.19: Velocity plot: The velocity pattern of the plasma which is moving away from the prominence pillar from 14 Feb 2011 (Fig. 3.18) .

The first seemed to be related to flows along the prominence and the second to heating and compression along the cavity boundary due to a small eruption inside the filament channel.

To understand the prominence-filament structures in relation to the large-scale magnetic field, we compared the sites of brightening and pillars to the underlying photospheric flux. For this purpose we used line-of-sight magnetograms from GONG and composite SDO and STEREO-A 195Å EUV images. Fig. 3.20 shows EUV images and contours of the images overlaid on the GONG magnetic fields for the 13 February 2011. The interpretation of these images at such high latitudes is ambiguous but the large scale is still discernible. To the south west was strong positive polarity active region flux that has diffused to this position during the previous 27 days (Fig. 3.20a,b). A close-up of the diffused positive flux and higher latitude negative flux is shown in the HMI image (Fig. 3.4a). We tend to believe that cancellation of the newly diffused positive flux with pre-existing negative flux elements is the reason for the many microflares at B1, B3 and B4 (Fig. 3.20).

A sketch of the inferred magnetic topology and sites of the prominence features is shown in Fig. 3.21. Since the observations were made in the rising phase of the solar cycle when the negative polarity is dominant over the northern pole, we have placed a region of negative field over the pole. The newly diffused active region is on the south west. The positions of the other magnetic flux regions are more speculative and are chosen to reflect the structure seen in the GONG map and the observation that filaments form between adjacent active regions. Martens and Zwaan (2001) proposed a flux linkage model to explain the chains of polar crown filaments. Here we have the situation where the arrival of new active region flux is merging with an already formed chain due to magnetic field reconnection at B2, B1, and B4 which in the process leads to the injection of flux and plasma into the prominence.

In this work, we have demonstrated the possibility of being able to dissect polar crown prominences into individual pillars, and filament flows using observations from spacecrafts separated by about 90°. These dynamics suggest the presence of complex magnetic geometries in the filament channel. The arrival of diffused active region flux seems to play an important role in the evolution of this prominence-filament system.

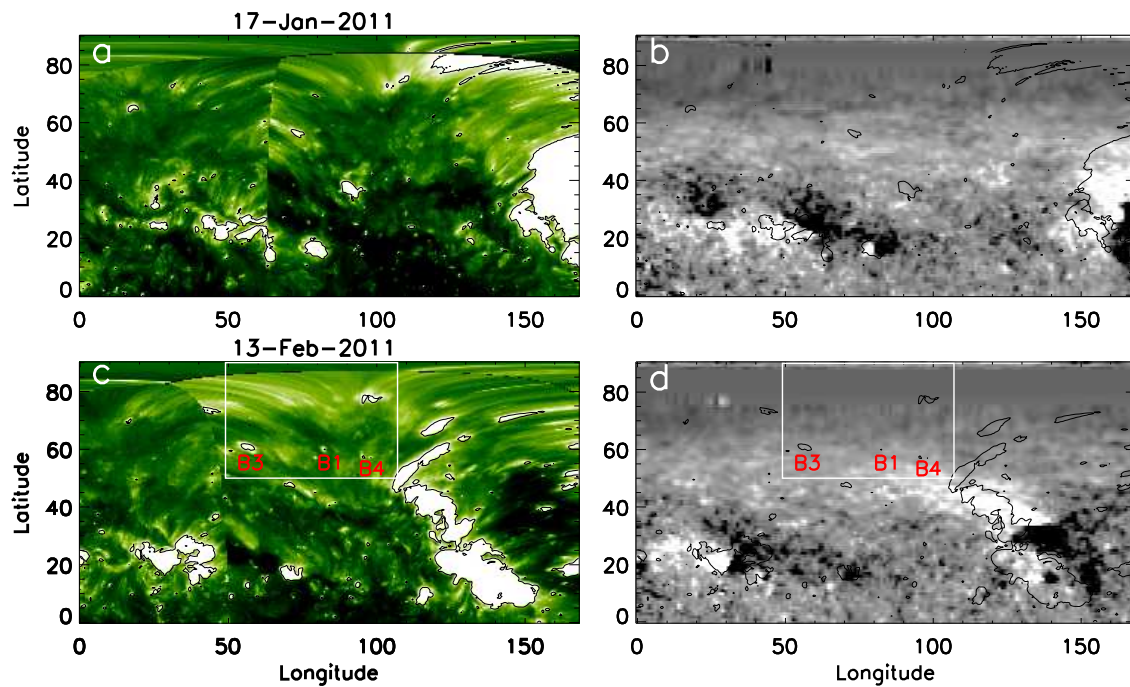


Figure 3.20: Magnetic field structure: a) Stoneyhurst projection of STEREO-A 195Å intensity on 13/2/2011 with contours outlining the brightest patches; b) Gong synoptic map for 13/2/2011 with the same contours as in (a); c) as (a) one solar rotation earlier (17/1/2011); d) as (b) for 17/1/2011. Features identified in Fig. 3.6 and discussed in the text are marked. The white box outlines the region of the prominence-filament system is shown in Fig. 3.6.

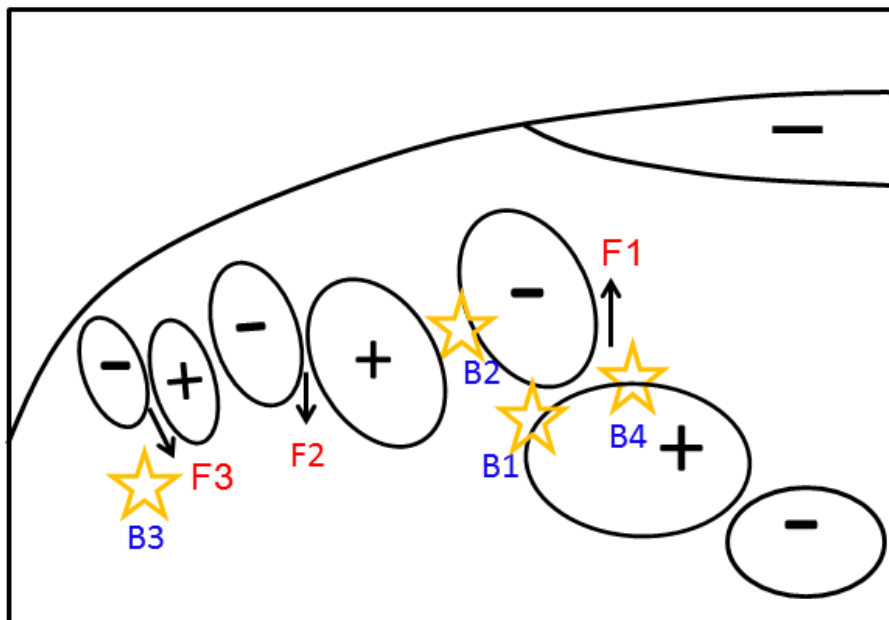


Figure 3.21: Sketch of our observations. Stars show sites of the various brightenings. Pillars are marked as F1, F2 and F3. Positive and negative sign represent the magnetic flux polarity.

In Summary, we investigated the structure and dynamics of a polar crown prominence/filament system in this chapter. We propose that the dark feature observed in the 195Å images of the filament channel can be the disk signature of the coronal cavity (of low density) rather than the cool and condensed matter of prominence. The velocity of the flows along the prominence pillars are in agreement with the earlier quiescent prominence observations (Berger et al. 2008). The magnetic configurations and brightenings at photosphere shows a resemblance with the flux linkage model of the prominence.

In next chapter, we will show an interesting activation of a quiescent prominence which gets accelerated after a flare and appeared like a tornado prominence.

## 4 Activation of a tornado-like prominence<sup>★</sup>

Solar tornados are dynamical, conspicuously helical magnetic structures that are mainly observed as a prominence activity. We investigate and propose a triggering mechanism for the solar tornado observed in a prominence cavity by SDO/AIA on September 25, 2011. High-cadence EUV images from the SDO/AIA and the Ahead spacecraft of STEREO/EUVI are used to correlate three flares in the neighbouring active-region (NOAA 11303), and their EUV waves, with the dynamical developments of the tornado. The timings of the flares and EUV waves observed on-disk in  $195\text{\AA}$  are analysed in relation to the tornado activities observed at the limb in  $171\text{\AA}$ . Each of the three flares and its related EUV wave occurred within ten hours of the onset of the tornado. They have an observed causal relationship with the commencement of activity in the prominence where the tornado develops. Tornado-like rotations along the side of the prominence start after the second flare. The prominence cavity expands with the accelerating tornado motion after the third flare. Flares in the neighbouring active region may have affected the cavity prominence system and triggered the solar tornado. A plausible mechanism is that the active-region coronal field contracted by the ‘Hudson effect’ through the loss of magnetic energy as flares. Subsequently, the cavity expanded by its magnetic pressure to fill the surrounding low corona. We suggest that the tornado is the dynamical response of the helical prominence field to the cavity expansion.

### 4.1 Introduction

Prominences consist of relatively large, cool and over dense plasma seen in the lower corona above the solar limb (Martin 1998a, Tandberg-Hanssen 1995, Mackay et al. 2010). Their structure and composition are exceedingly complicated. The plasma mainly resides in highly tangled magnetic fields (van Ballegooijen and Cranmer 2010). Coronal cavities are often observed to have cooler prominence plasma at their bases (Hudson et al. 1999a, Gibson and Fan 2006, Régnier et al. 2011). The cavity is a region of relatively low density, high temperature plasma (Gibson et al. 2010, Habbal et al. 2010). Berger et al. (2011) have proposed that the prominence and its cavity are a form of magneto-thermal convective structure, macroscopically stable but internally in a constant state of ubiquitous motions (Low et al. 2012a,b).

---

<sup>★</sup> This work has been published in A&A: N. K. Panesar, D. E. Innes, S. K. Tiwari, B. C. Low, 2013, A&A, 549, A105, reproduced with permission © ESO

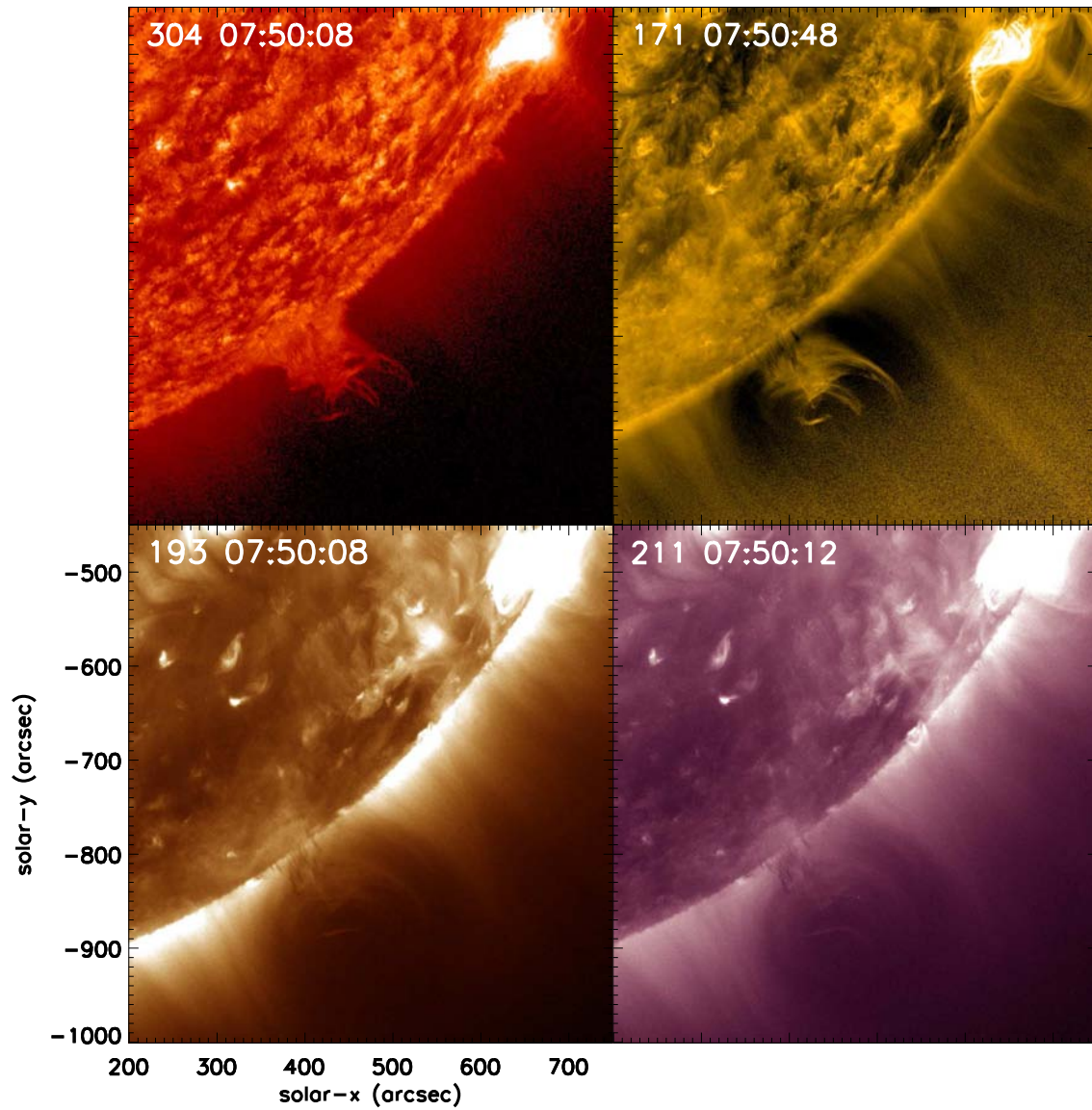


Figure 4.1: A prominence-tornado observed on 25 September 2011: The images show the prominence-cavity system observed by SDO/AIA in four different wavelengths on south-west solar limb.



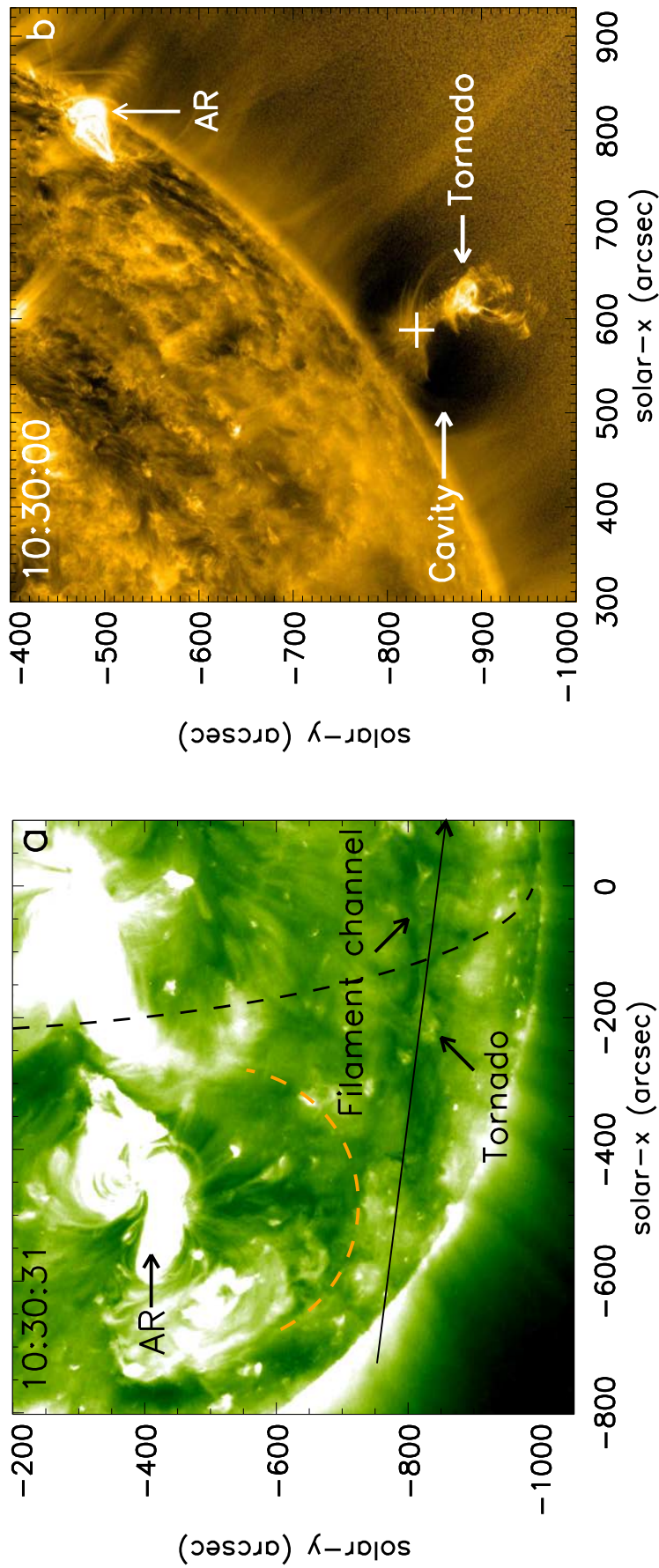


Figure 4.2: The region around a tornado on 25 September 2011: a) EUVI-A 195Å; b) AIA 171Å images. On the EUVI image, the dashed line shows the position of the AIA limb, and the long diagonal arrow is the epipolar line for the prominence position marked with '+' on the AIA image. The orange dashed line outlines the position of the southern edge of the AR corona.

Viewed at the limb, quiescent prominences mostly appear as curtains of vertical thread-like structures (Berger et al. 2008). Occasionally they look like tornados with rotations along, or of, their magnetic structures (Pettit 1932, 1943, Liggett and Zirin 1984). At first glance it is not obvious why tornados do not erupt but continue rotating for several hours before quietening down. Recently, images from Atmospheric Imaging Assembly (AIA) on the Solar Dynamic Observatory (SDO), have allowed the study of solar tornados (Li et al. 2012, Su et al. 2012, Liu et al. 2012a). The driving mechanism may be a coupling and expansion of a twisted flux rope into the coronal cavity (Li et al. 2012) and/or related to photospheric vortices at the footpoint of the tornado (Velli and Liewer 1999, Attie et al. 2009, Wedemeyer-Böhm et al. 2012, Su et al. 2012, Kitiashvili et al. 2013, Rappazzo et al. 2013).

This chapter is a study of the impressive solar tornado observed by AIA on 25 September 2011 (shown in Fig. 4.1). Li et al. (2012) described the formation and disappearance of the related prominence by analysing SDO data from 24-26 September. The evolution of the tornado was attributed to the expansion of helical structures into the cavity. But the reason behind the expansion remained an open question.

Here we analyse observations on the mechanism leading to the expansion of the prominence. We show using Solar TERrestrial RELations Observatory (STEREO) Extreme UltraViolet Imager (EUVI) observations that three strong flares in a neighbouring active region coincided with phases of the tornado activation. A Flare is known as the eruptive phenomena when there is a sudden release of free magnetic energy from the Sun. Often they are associated with EUV (extreme ultra violet) waves. Each flare was associated with a Coronal Mass Ejection (CME) and EUV wave. Particularly, after the third flare, there was slow but significant expansion of the overlying prominence cavity together with more rapid rotation at the top of the prominence. We describe the observations in Section 4.2. The evolution of the tornado, its relationship to the solar flares and EUV waves are described in Section 4.3. In Section 4.4, we summarize our observations and speculate on the link between the flares and the cavity expansion.

## 4.2 Observations

The solar tornado on 25 September 2011 was observed on the south west limb by SDO/AIA (Lemen et al. 2012). In images from EUVI on the Ahead spacecraft of STEREO (Howard et al. 2008), it appeared on the solar disk around  $15^\circ$  E. The separation angle between SDO and STEREO-A was  $103^\circ$  (see Chapter. 2, Fig. 2.8). We study the tornado by combining observations from the two directions.

AIA takes high spatial resolution ( $0.6'' \text{ pixel}^{-1}$ ) full disk images with a cadence of 12 s. For the analysis, we select images from the  $171\text{\AA}$  channel which is centered on the Fe IX line formed around 0.63 MK. Images from this channel show both hot, bright emitting and cold, dense absorbing parts of the prominence, as well as the dark, low density cavity and the surrounding coronal loops. To enhance the visibility of the cavity and faint loops, we removed an average background from the  $171\text{\AA}$  images. The background is the median of two months data - September and October, 2011.

During the period studied, 01:30-13:30 UT, SDO was in eclipse from 06:02-07:13 UT. This gap is covered by the SWAP instrument on PROBA-2 (Halain et al. 2010). SWAP

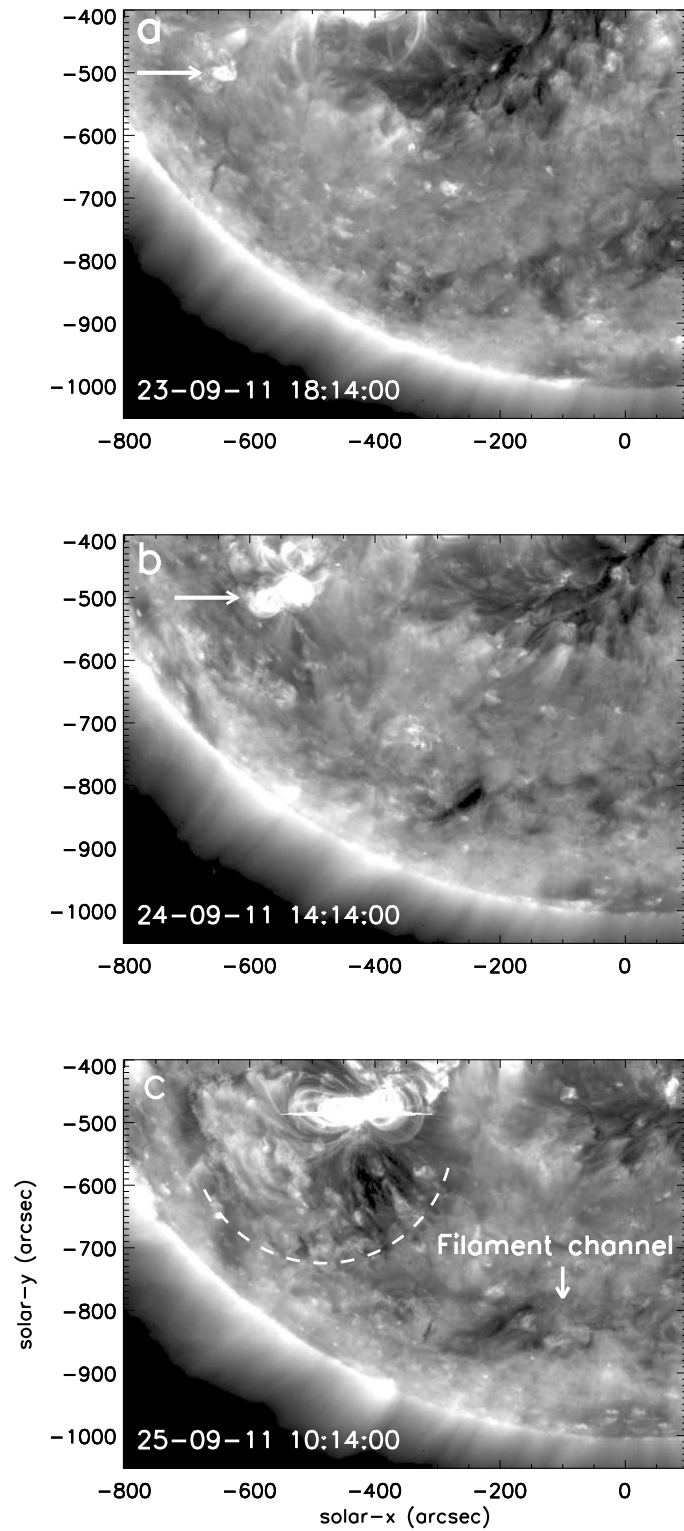


Figure 4.3: STEREO-A 171Å intensity images from 23-25 September 2011. The arrows show the positions of the emerging active region (AR). The filament channel is indicated by an arrow. The dashed line outline the southern of the active region corona.

provides a full Sun 174Å image every 2-3 min with a spatial resolution of 3.16'' pixel<sup>-1</sup>. The images are not as detailed as AIA images but are essential for checking the behaviour of the prominence during the data gap.

The EUVI-A 195Å images have a time cadence of 5 min and resolution of 1.6'' pixel<sup>-1</sup>. The 195Å emission is mainly Fe XII formed at ~1.2 MK. To confirm the prominence position in the EUVI images, we obtained the three-dimensional coordinates of the prominence with the routine SCC\_MEASURE (Thompson 2009) available in the SolarSoft library.

### 4.3 Overview

In Fig. 4.2 we show the EUVI-A 195Å and AIA 171Å images of the filament/prominence and the active region NOAA 11303 (marked with an arrow) as seen from the two angles. The position of the cross on the stem of the prominence lies along the epipolar line drawn as a long black arrow on the EUVI image. The dark lane crossed by the epipolar line is the filament channel and the tornado is the bright region that coincides with the epipolar line and the filament channel, indicated with a black arrow. The core of the active region is separated by 300'' from the filament channel. However, the southern edge of the active region corona (outlined by orange dashed line) reaches to within 50'' of the filament channel. We have verified that this is a newly emerged active region which is appeared on 23 September (see Fig. 4.3a,b).

#### 4.3.1 The three flares

There were flares at approximately 02:45, 07:00, 09:40 UT from the nearby active region. They were all associated with CMEs and EUV waves. The third was GOES class M1.4 according to the NOAA flare catalogue<sup>1</sup>. The GOES class of the first two are not given in the catalogue. We therefore checked the hard X-ray quicklook images from the Reuven Ramaty High Energy Solar Spectroscopic Imager (RHESSI). Unfortunately they both had their peaks during RHESSI data gaps. The first RHESSI image in the flares' decay phase showed that these flares were the brightest RHESSI sources. At the time of the first and second flares the GOES 1-8Å fluxes reached the M4.4 and M1.0 level respectively, so it is possible that these too were M-class flares.

The flares' onsets and related EUV waves can be seen in the 195Å running ratio images shown in Fig. 4.4. The running ratio images are the log of the intensity at the time shown on the images divided by the intensity 5 min earlier. Because this reflects relative changes the faint EUV waves show up against bright inactive active regions. The faint EUV wavefronts sweep over the filament channel about half an hour after the flare (bottom row). The small white arrows point to the tornado site where there was increased activity along the filament channel after the flares.

When we take a time series along the orange dashed line drawn on Fig. 4.4d, we are able to see the relation between the EUV waves and the filament activity (Fig. 4.5). In this time series image, the waves associated with the three flares are marked by F1, F2 and F3 and a white arrow points to the filament activity. We note that the filament

---

<sup>1</sup><ftp://ftp.ngdc.noaa.gov/STP/space-weather/solar-data/solar-features/solar-flares/x-rays/goes>

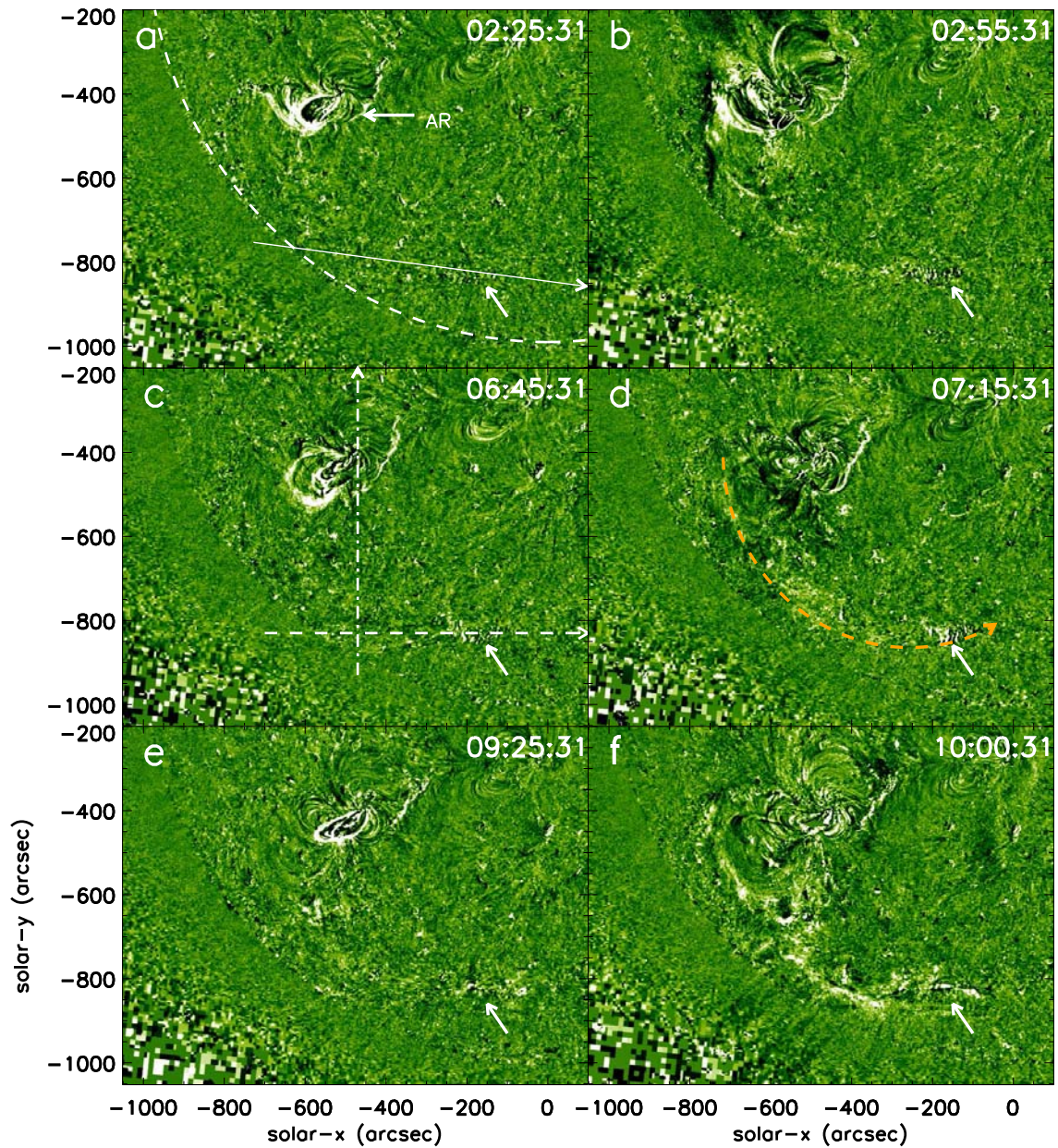


Figure 4.4: EUVI-A  $195\text{\AA}$  running ratio images showing the onset of the three flares (a,c,e) and their associated EUV waves (b,d,f). In (a) the epipolar line shown in Fig. 4.2a is drawn as a long white arrow, and the position of the time series in Fig. 4.6c. The solar limb is drawn as a dashed white line. The small white arrow in all images points to the tornado site. The dot-dashed/dashed lines in (c) mark the positions of time series shown in Fig. 4.6a,b, and the orange dashed line along the EUV wave front in (d) the position of the time series in Fig. 4.5.

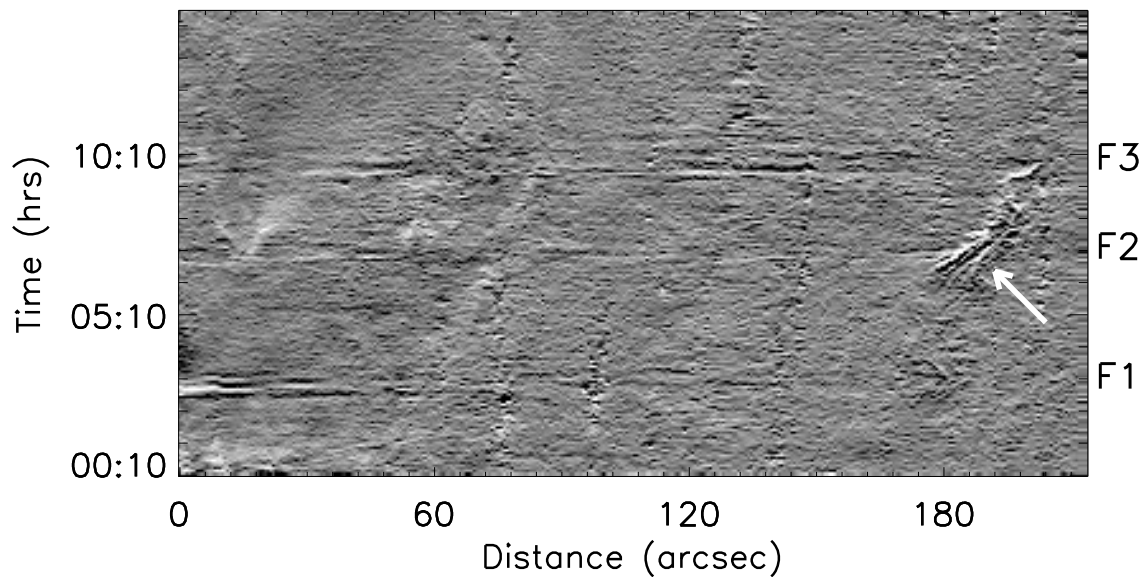


Figure 4.5: EUVI 195Å running ratio space time image along the dashed line in Fig. 4.4d. Three flares are labelled as F1, F2 and F3. The arrow points to the filament.

activity associated with F2 increased before the arrival of the EUV wave. We also notice that each EUV wave front was followed by a series of oscillations with a period of 20 min at the edge of the active region and along the filament channel. Similar post-EUV cavity oscillations, seen at the limb in AIA images, have been reported by Liu et al. (2012b). EUVI images have a much lower cadence than AIA, and may not be resolving the wave trains. As mentioned above, the EUV wave reached the filament channel after the filament activation. To investigate whether the activation could have been triggered by the flare, we took time series through the flare sites (vertical line Fig. 4.4c) and along the filament channel across the activated filament (horizontal line in Fig. 4.4c). We observe that there are perturbations in the filament plasma immediately after each flare (yellow arrows in Fig. 4.6b,c). Large-scale changes along the filament channel started after F2 and increased further after the F3.

The reaction of the prominence to the flares is illustrated in Fig. 4.10. The positions of the three time series are drawn on Fig. 4.9, an AIA image of the active region and tornado. The oscillations of the prominence at the time of F1 (Fig. 4.10a) are consistent with a flare trigger from the north since it moved first towards the pole. The wobbling in the prominence after the flare is also clearly visible in the movie.

The second flare, F2, was at ~06:45 UT when SDO was in eclipse. Since this phase is important for understanding the tornado, we checked the SWAP data to see if the prominence activation started before F2. The SWAP data clearly show the relation between flare and prominence expansion (see Fig. 4.8). Although the SWAP images are not as sharp as AIA images, they show quite clearly that increased prominence activity occurred after F2 and that the first AIA images after eclipse caught the expansion of the flare loops and the rapid growth in prominence activity. The middle image in Fig. 4.10b, taken along the dashed line in Fig. 4.9, shows an arm of prominence plasma reaching out in the direction of the active region. There is also a very slight expansion of the cavity boundary towards the active region.

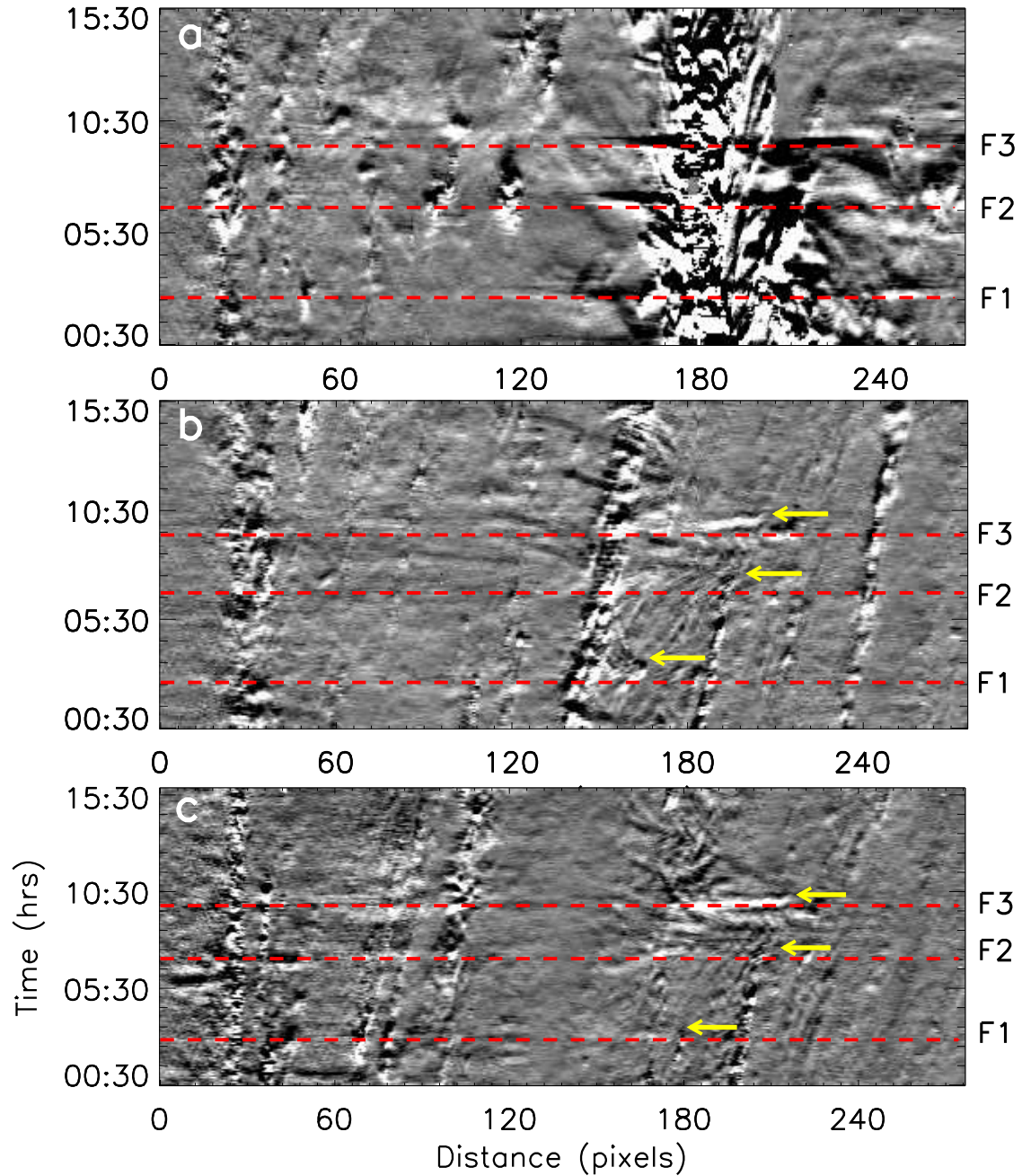


Figure 4.6: EUVI 195Å running difference time series along (a) the vertical, (b) the horizontal line in Fig. 4.4c and (c) the long diagonal arrow in Fig. 4.4a. The red dashed lines are drawn at the flare F1, F2, and F3 times. In b) and c) the yellow arrows point to the changes in filament structure after the flares.

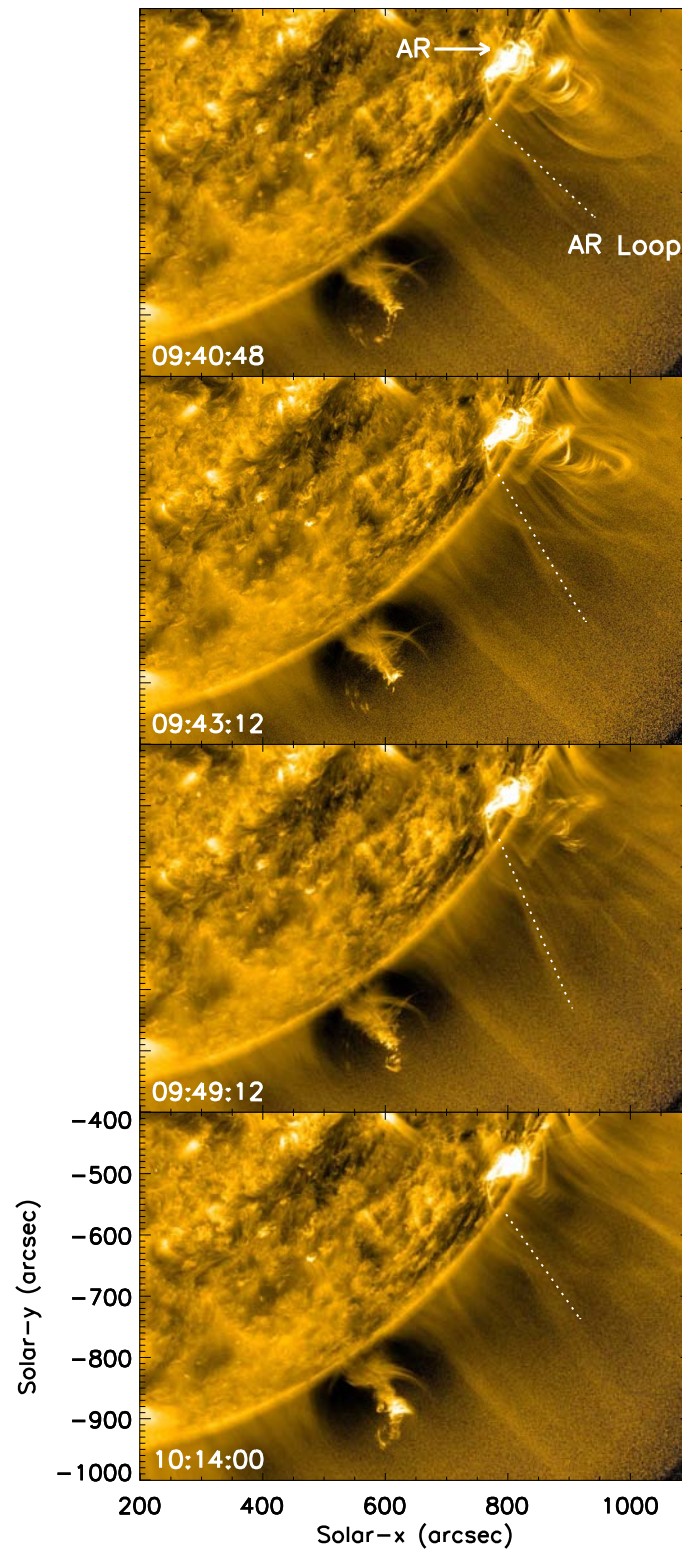


Figure 4.7: AIA 171Å intensity images during the third flare. Images show the expansion of active region loop (AR loop) towards the prominence-cavity system. Active region is indicated with an arrow.



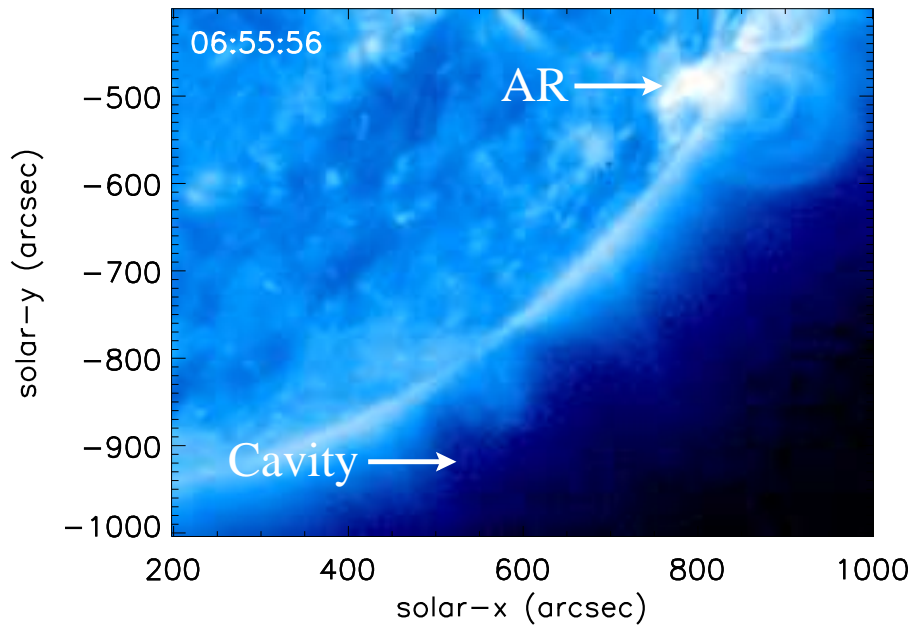


Figure 4.8: SWAP 174Å intensity image from 25 September 2011 taken at the time of second flare. The arrows show the positions of the cavity and the active region (AR).

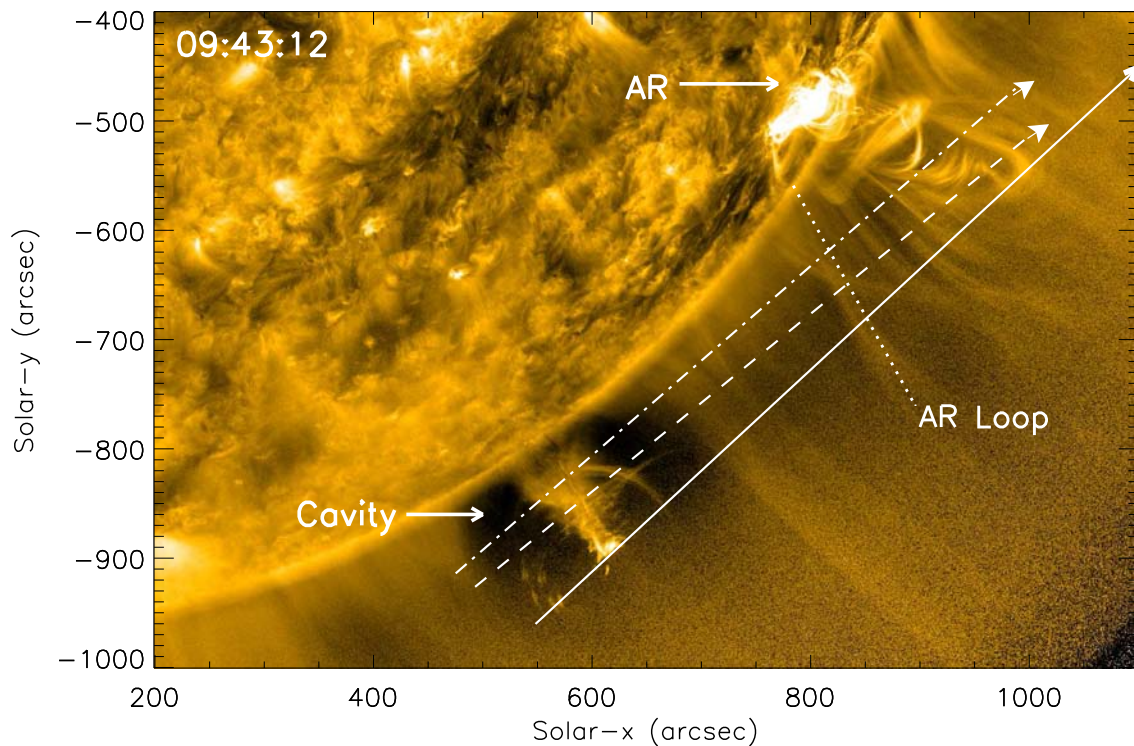


Figure 4.9: AIA 171Å intensity image. The diagonal long arrows show the positions of the time series images through the prominence/tornado, cavity, active region hot loop (AR loop) and active region (AR) shown in Fig. 4.10. 'FLARE-1' shows the evolution of this region at earlier times.

The biggest change in the cavity occurred after F3 when the bright and complex top part of the prominence started to rotate faster. Fig. 4.9, shows the evolution of the tornado and flare from F2 to a couple of hours after F3. The time series in Fig. 4.10c, taken along the top white arrow in Fig. 4.9, shows the main features. The flare erupted at 09:20 UT. The active region loops started expanding at 09:40:48 UT (see Fig. 4.7). At 09:50:13 UT there was a sharp contraction, approximately 10 Mm, of the observed cavity and the cavity started expanding back towards the active region after  $\sim 10:00$  UT. It grows from 140 Mm to 167 Mm in 3.5 hours. At the same time, the prominence grew in height and the bright and complex head of the prominence started to rotate faster, forming the tornado. The rotations at the top of the prominence/tornado lasted  $\sim 3.5$  hours with a speed from  $55 \text{ km s}^{-1}$  to  $95 \text{ km s}^{-1}$  (Li et al. 2012).

## 4.4 Discussion

A solar tornado was observed by AIA and EUVI-A on 25 September 2011. The tornado was reported by Li et al. (2012), who attributed it to the growth of a helical prominence system. The reason for the prominence growth remained unanswered. After careful observation of the event using AIA full disk images, we noticed that AR 11303, to the north of the prominence cavity was flaring and suspected it of having influenced the prominence in some way. We observed three flares, and they were all associated with EUV waves that swept over the prominence cavity. Each time the cavity was buffeted by the wave, the prominence plasma became more active. After the third flare a tornado had developed at the top of the prominence.

After the first flare, there were clear oscillations along the prominence stem. The second flare caused plasma to move along arm-like extensions projecting out from the stem in the direction of the active region. These extensions appear to subsequently rotate back towards the prominence before the third flare. After the third flare the tornado became very strong and was stable for about 3.5 hours. The third flare seemed to have the biggest impact on the surrounding plasma or at least produced the most visible (at  $195\text{\AA}$ ) EUV wave. It also caused large active region loops to move towards the edge of the prominence cavity. Afterwards the loops swayed back and the cavity started to slowly ( $\sim 2.5 \text{ km s}^{-1}$ ) but visibly expand over the next 3.5 hours. During this time the prominence rose into the cavity creating the tornado.

To understand the relationship between the flare, the prominence, the cavity and the tornado there are a number of effects that need to be considered. The expansion of the cavity is clearly associated with the rise of the prominence plasma. One possible explanation for the expansion is that the loss of free magnetic energy from the active region by flares and CMEs (Zhang and Low 2005) resulted in a contraction of the active region field, the Hudson effect (Hudson 2000, Zhang and Low 2003, Janse and Low 2007). Subsequently the surrounding fields, including the cavity field, expanded to fill the vacated space. An idealized illustration of the Hudson effect, in terms of the force-free equilibrium between two bipolar fields before and after one of the fields has lost its free energy, is given in Fig. 4.11. Initially the active region field on the right has excess free energy, and the cavity field on the left is taken to be potential in order to simplify the calculation. During the eruption, the active region field loses free energy, decreasing its pressure since

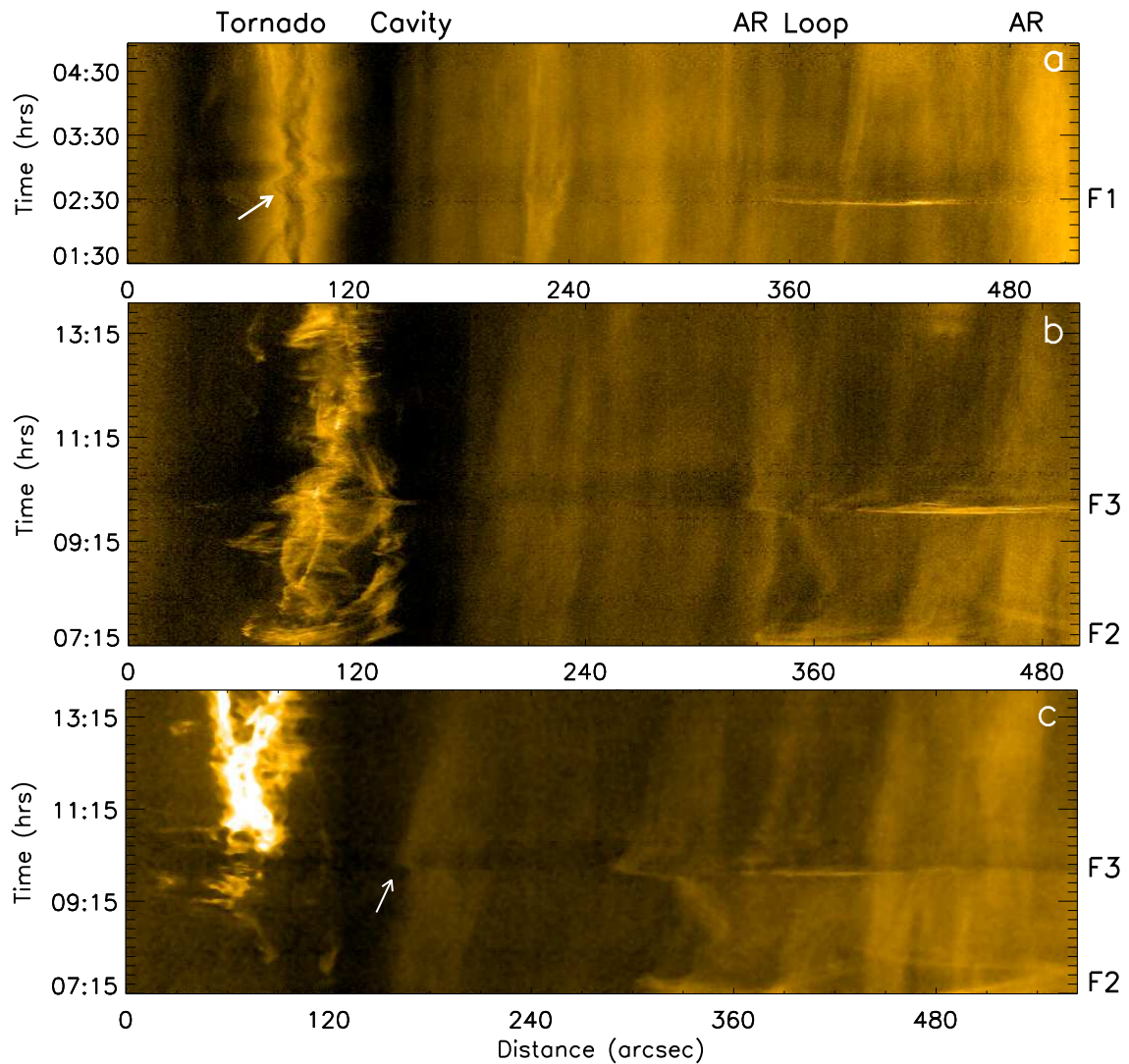


Figure 4.10: AIA 171Å intensity time series along the diagonal arrows in Fig. 4.9: a) oscillations of the prominence stem triggered by F1 taken along bottom white arrow; b) activity triggered by F2 and F3 taken along the middle white arrow; c) tornado activity and cavity changes triggered by F2 and F3 taken along top arrow. The arrow at the time of the flare (~09.40 UT) points to the movement of the cavity boundary.

the magnetic energy density  $B^2$  of a field  $\mathbf{B}$  is also the magnetic pressure. This leads to an expansion of the cavity field to restore pressure balance in the system.

We consider the 2D Cartesian domain  $0 < y < \pi$ ,  $0 < z < \infty$ , with  $x$  as an ignorable coordinate, taking the boundary to be a rigid perfect electrical conductor for simplicity. The initial state in Fig. 4.11a is a continuous global solution for the magnetic field,  $\mathbf{B} = \mathbf{B}_{initial}$  of the force-free equations

$$\nabla \times \mathbf{B} = \alpha \mathbf{B} = 0; \quad \nabla \cdot \mathbf{B} = 0, \quad (4.1)$$

describing a bipolar ( $\alpha = 0$ ) potential field representing the cavity that occupies the partial domain  $0 < y < 2\pi/3$ ,  $0 < z < \infty$ . This field continues into a constant- $\alpha$  force-free field representing the active region that occupies the complementary partial domain  $2\pi/3 < y < \pi$ ,  $0 < z < \infty$ . Their interface  $y = 2\pi/3$ , is in force balance because the fields on its two sides exert equal magnetic pressure. Suppose the electric current of the constant- $\alpha$  force-free field is removed from the partial domain  $2\pi/3 < y < \pi$ ,  $0 < z < \infty$  to represent a flare-like loss of free energy. The distribution of the normal component of the field along the rigid boundary and the magnetic foot-points on the base  $z = 0$  cannot change. This boundary condition then determine the unique end-state,  $\mathbf{B}_{end}$ , with  $\alpha = 0$  everywhere in the domain (Fig. 4.11b). The former bipolar field on the right has contracted downward and withdrawn into a partial domain of a finite height while the other bipolar field now occupies the whole infinite space above that height. The fluid-interface between the two fields is now an arc of finite length. These mathematical solutions, given in the next section, serve to conceptually make specific a basic effect in the complex processes of a real energy release.

In addition to the active region contraction, the CME/flare eruptions generated hydromagnetic disturbances, seen as EUV waves, that perturbed the surrounding low corona. They evidently caused swaying in the prominence and oscillations along the cavity boundary. These perturbations may have been intense enough to partially destabilize the cavity-prominence system, thereby contributing to or possibly even initializing the tornado-like activity.

Our observational study supports the interpretation that the CME/flare activities in the active region had a causal relationship with the nearby tornado. It is clear that the tornado was dynamically associated with the expansion of the prominence's helical field and its cavity. It is an open question as to whether the Hudson effect drove the cavity expansion and the helical field was responding dynamically to the expansion, or, the helical field loses its meta-stability as the result of hydromagnetic disturbances from the CME/flares from the active region. This physical question is worthy of MHD time-dependent simulation. Evidence of the Hudson effect has been reported in recent solar observational studies (e.g. Sun et al. 2012, Liu et al. 2009). Our study shows the importance of this effect in relation to CMEs, flares and prominences, and provides observational motivation for theoretical MHD modeling to address the specific questions posed by this relationship.

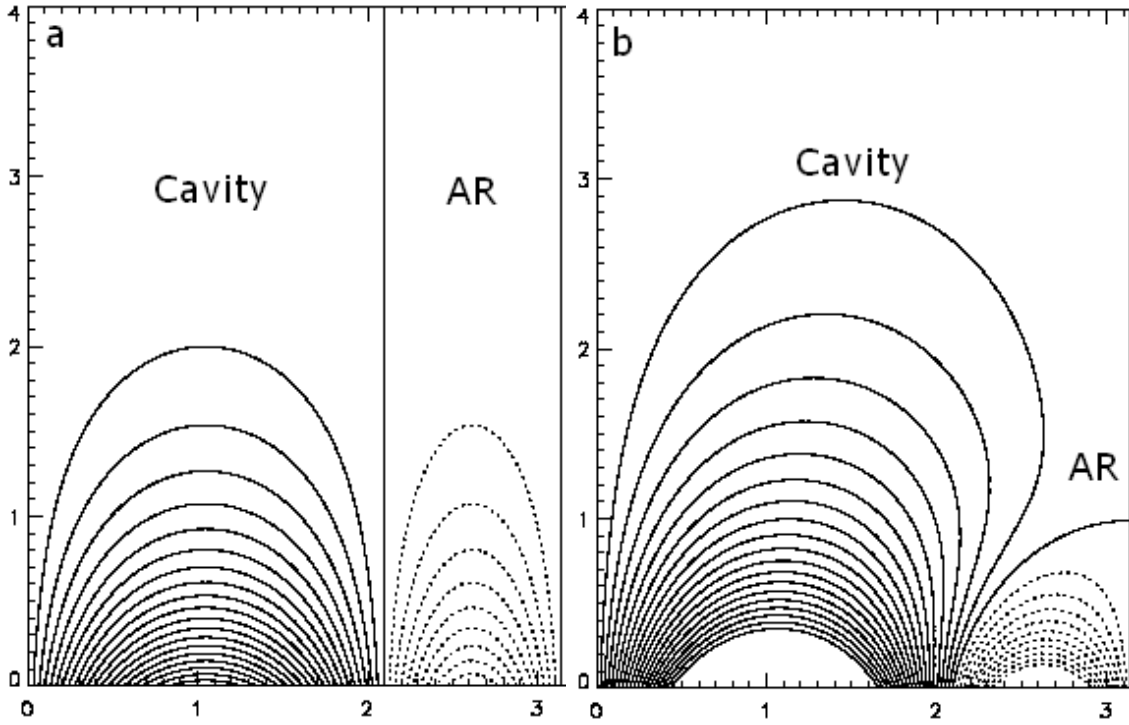


Figure 4.11: Idealized 2D Cartesian magnetic fields of the cavity and active region (a) before and (b) after the flare, in a domain  $0 < y < \pi, 0 < z < \infty$  with  $z$  denoting coronal height.

#### 4.4.1 Mathematical Illustration of the Hudson Effect

We give the mathematical solutions for 2D magnetic fields in Fig. 4.11, according to B.C. Low (private communication). Use the representation

$$\mathbf{B} = \left[ Q, \frac{\partial A}{\partial z}, -\frac{\partial A}{\partial y} \right], \quad (4.2)$$

in terms of the scalar flux-function  $A(y, z)$  and the component  $B_x = Q(y, z)$  corresponding to the ignorable coordinate  $x$ . The initial field  $\mathbf{B}_{initial}$  in Fig. 4.11a is given by  $A = A_{initial}$  and  $Q = Q_{initial}$  where

$$A_{initial} = A_{pot} = 2 \sin\left(\frac{3}{2}y\right) \exp\left(-\frac{3}{2}z\right); \quad Q_{initial} \equiv 0, \quad \text{in } 0 < y < 2\pi/3, 0 < z < \infty$$

$$A_{initial} = A_{fff} = -\sin(3y) \exp\left(-\frac{3}{2}z\right); \quad Q_{initial} = \sqrt{\frac{27}{3}}A, \quad \text{in } 2\pi/3 < y < \pi, 0 < z < \infty \quad (4.3)$$

The end-state field  $\mathbf{B}_{end}$  is the everywhere-potential field with  $A = A_{end}$  where

$$A_{end} = \sum_{n=1}^{\infty} a_n \sin ny \exp(-nz), \quad (4.4)$$

$$a_3 = \frac{1}{3} \quad \text{and} \quad a_n = \frac{2 \times 3^4}{\pi} \sin \frac{2\pi n}{3} \frac{1}{(4n^2 - 9)(n^2 - 9)}, \quad \text{for } n \neq 3, \quad (4.5)$$

with  $Q \equiv 0$ . Both  $\mathbf{B}_{initial}$  and  $\mathbf{B}_{end}$  have the same distribution of normal field component along the boundary of the domain  $0 < y < \pi, 0 < z < \infty$ .



## 5 Thermal stratification of a prominence using DEM

In previous chapters we studied the structure and dynamics of quiescent prominences. In this chapter we aim to investigate the multi-thermal structure of prominences by using the SDO/AIA data, and show our preliminary results.

As mentioned in Chapter 1, the corona is highly inhomogeneous in its temperature and density structure. The hotter coronal emission results from ionized gas at temperatures greater than 1 MK. We can get the temperature information from the emission of coronal structures in different SDO/AIA images. For this we need a wide range of temperature filters. The SDO provides images in six EUV channels that can be used to determine coronal temperatures from 1 - 10 MK. The 304 Å emission indicates the presence of much cooler, 0.1 MK transition region plasma. Fig. 5.1 shows a three colour composite image of the Sun captured by the SDO/AIA. The cooler plasma (of temperature  $\sim 0.6$  MK) is shown in blue colour e.g. coronal holes at northern and southern pole. The active region loops show the hot plasma ( $\sim 2$  MK) in brown colour. The green regions are hotter than the bluish ones.

By analysing the intensities in the various EUV channels we can determine the temperature and emission measure of the coronal plasma. Several such analysis of SDO/AIA images have revealed the thermal structure of coronal loops (Aschwanden 2002) and evolution of flaring plasma (McTiernan et al. 1999, Hannah and Kontar 2013). We use, the differential emission measurement (DEM) technique on the prominence cavity and the neighbouring active region to study the thermal evolution of the tornado-like prominence before and after the flare. There are some DEM codes available in SolarSoft e.g. by Hannah and Kontar (2012), Aschwanden et al. (2013). In the next section, first we will give the introduction about the DEM, and then present preliminarily results obtained and a brief discussion on them.

### 5.1 Introduction

The intensity of a spectral line  $I(i, j)$  in the optically thin corona, is given by the integral of the line emission along the line-of-sight (McWhirter 1984, Bruner and McWhirter 1988):

$$I(i, j) = \frac{h\nu}{4\pi} \int_0^{\infty} n_e n(z, Z) X'(g, i) dx, \quad (5.1)$$

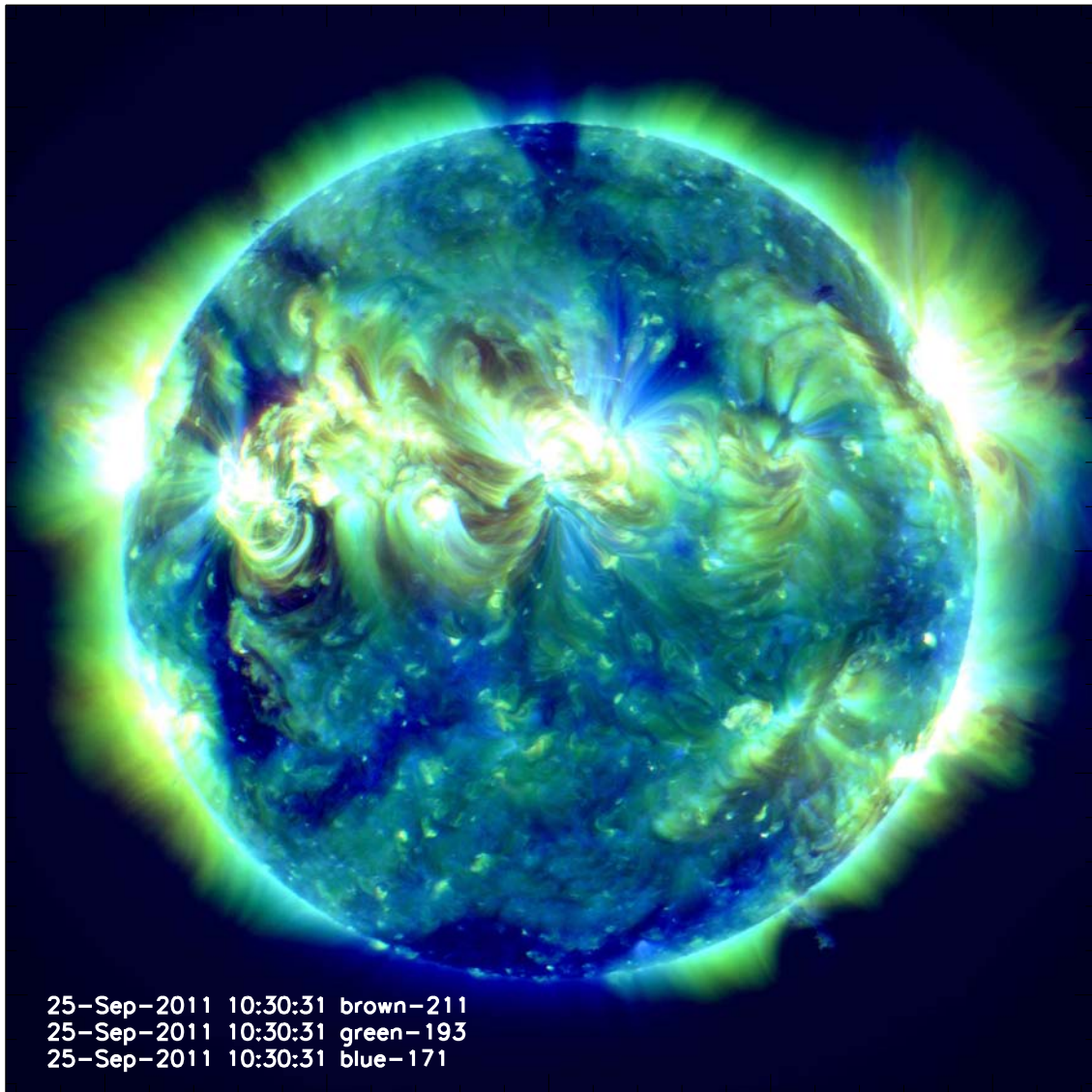


Figure 5.1: Three-colour (211 Å, 193 Å and 171 Å) SDO/AIA intensity image of full-solar disk from 25-September-2011. The active regions appear as bright regions on solar disk and limb. The formation temperatures of the lines contributing channels are 211 Å Fe XIV at 2 MK, 193 Å Fe XII at 1.5 MK, and 171 Å Fe IX at 0.6 MK.



where  $I(i, j)$  is the intensity of the spectral line (with units  $\text{erg cm}^{-2} \text{s}^{-1} \text{sr}^{-1}$ ) between upper state  $i$  and lower state  $j$  of the emitting ion;  $n_e$  is the population density of the free electrons ( $\text{cm}^{-3}$ );  $n(z, Z)$  is the population density of the ions;  $X'(g, i)$  is the effective excitation rate coefficient of the transition of ion from ground level  $g$  to upper level  $i$  (in  $\text{cm}^{-3} \text{s}^{-1}$ ) and  $z, Z$  are the ion charge and nuclear charge of the emitting ion.

If we assume that the electron temperature varies monotonically with the distance in the corona. Equation 5.1 can be written as the integral over electron temperature (Bruner and McWhirter 1988):

$$I(i, j) = \frac{h\nu n(Z)}{4\pi n(H)} \int_{T_{min}}^{T_{max}} n_e^2 \frac{n(H)}{n_e} \frac{n(z, Z)}{n(Z)} X'(g, i) \frac{dx}{dT_e} dT_e, \quad (5.2)$$

In Equation 5.2,  $n(Z)/n(H)$  is the ratio of the number of atoms of nuclear charge  $Z$  to the hydrogen (i.e. the atomic abundance) and we assume it constant over the height so it is kept outside the integral in Equation 5.2;  $n(H)/n_e$  is the ratio of hydrogen number density relative to the electron number density and it depends on the state of ionization of hydrogen, its also a function of electron temperature.  $n(z, Z)/n(Z)$  is a fraction of ions of nuclear charge  $Z$ , in ionization state  $z$ . It is a function of electron temperature,  $T_e$ .

The integral term in R.H.S of Equation 5.2 can be split into two terms - contribution function ( $G(T_e)$ ) and differential emission measure ( $\Phi(T_e)$ ). where contribution function contains the density and temperature dependent terms:

$$G(T_e) = \frac{n(H)}{n_e} \frac{n(z, Z)}{n(Z)} X'(g, i) \quad (5.3)$$

$G(T_e)$  is the contribution function (in units of  $\text{cm}^3 \text{s}^{-1}$ ), it includes the information of the atomic physics that tells about the emitting radiation at a given temperature.

The differential emission measure can be define as:

$$\Phi(T_e) = n_e^2 \frac{dx}{dT_e} \quad (5.4)$$

$\Phi(T_e)$  is the differential emission measurement ( $\text{cm}^{-5} \text{K}^{-1}$ ). It is defined as the measure of the electron density  $n_e$  along the line-of-sight at any given temperature (Mariska 1992, Aschwanden 2004). This is a general definition of DEM.

By using  $\Phi(T_e)$  and  $G(T_e)$  in Equation 5.2, the intensity of a observed spectral line is:

$$I(i, j) = \frac{h\nu n(Z)}{4\pi n(H)} \int_{T_{min}}^{T_{max}} G(T_e) \Phi(T_e) dT_e \text{ ergs cm}^{-2} \text{s}^{-1} \text{sr}^{-1}. \quad (5.5)$$

This equation gives the information about the thermodynamic state of the corona. The contribution function can be estimated by using CHIANTI database for each line (Dere et al. 1997, 2009) and differential emission measurement can be computed by using spectral line fluxes from different EUV images (see Section 5.2).

If we take the integral of the  $\Phi(T_e)$  within a fixed temperature range, we will get the total emission measure,

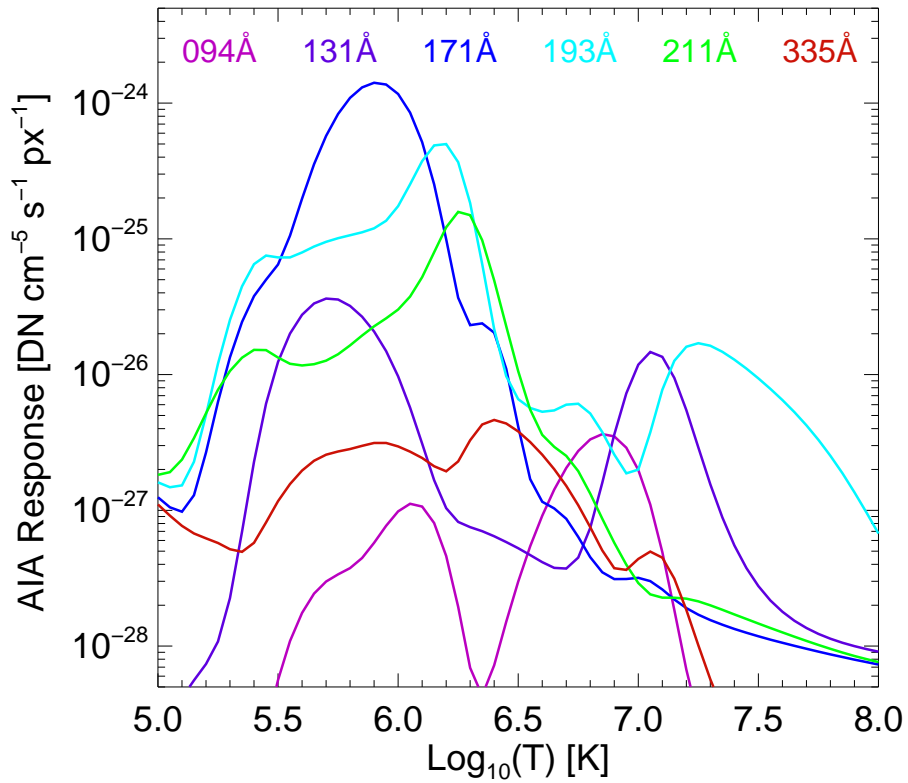


Figure 5.2: The SDO/AIA temperature response function for six EUV channels (Boerner et al. 2012).

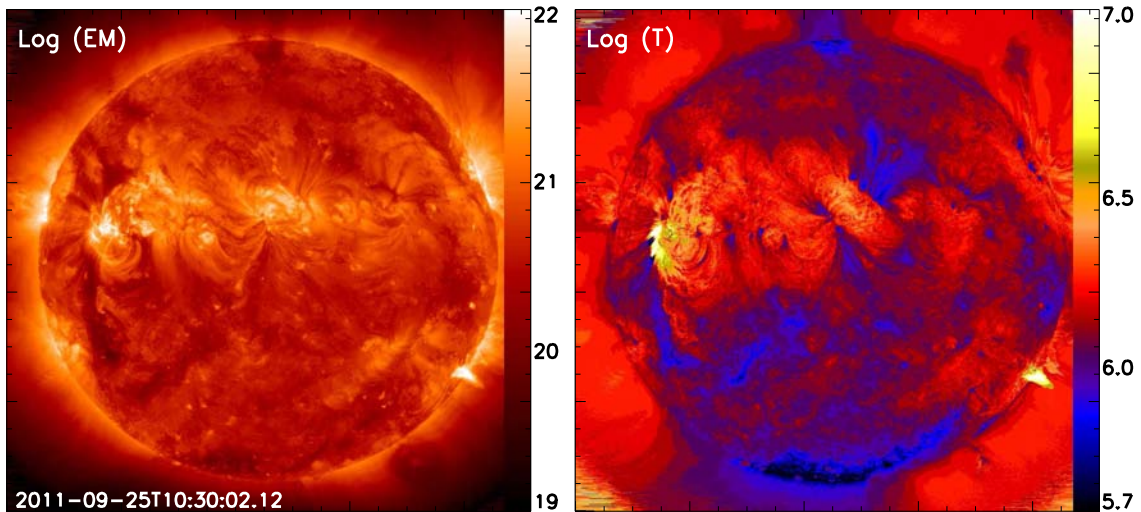


Figure 5.3: *Left panel* shows the peak emission and *Right panel* shows the temperature distribution calculated from the six AIA EUV channels (25 September 2011). The emission and temperature range is from  $\log(\text{EM}) = 19\text{-}22 \text{ cm}^{-5} \text{ K}^{-1}$  and  $\log(T) = 5.7\text{-}7.0$  ( $T \sim 0.5 - 10 \text{ MK}$ ) and the spatial resolution of the map is  $2.4''$ .

$$TEM = \int_{T_1}^{T_2} \Phi(T_e) dT_e \quad (5.6)$$

where  $TEM$  is the total emission measure ( $\text{cm}^{-5}$ )

### 5.1.1 AIA response function

As mentioned above, the contribution function contains the information of atomic physics. It shows the abundance of the electron and hydrogen number density. It can be calculated by using the CHIANTI atomic database (Dere et al. 1997, 2009). The CHIANTI database is mainly used to get the EUV spectra at wavelengths greater than  $1\text{\AA}$  under the coronal assumption - optically thin, ionization equilibrium and plasma in a steady state. The coronal abundances were taken from Feldman and Widing (1993) and Dere et al. (2009). With the use of coronal assumption, AIA temperature response function for six EUV channels can be calculated:

$$K_i(T) = \int_0^{\infty} G(\lambda, T) R_i(\lambda) d\lambda. \quad (5.7)$$

Where  $K_i(T)$  is the temperature response function of an EUV channels that can be calculated by using contribution function  $G(\lambda, T)$  and wavelength response function  $R_i(\lambda)$ . The AIA temperature response curves are shown in Fig. 5.2, in units of  $\text{DN s}^{-1} \text{pixel}^{-1}$ . It shows the sensitivity of each channel as a function of temperature. All the six EUV channels are dominated by the iron emission. The SDO/AIA  $131\text{\AA}$  channel is centered on the two iron lines Fe VIII and Fe XXI formed around  $6 \times 10^5$  K and at  $10^7$  K (see Fig. 5.2). Similarly  $193\text{\AA}$  channel is centered at two iron lines Fe XII and Fe XXIV which is formed around  $1.5 \times 10^5$  and  $1.9 \times 10^7$ . The  $94\text{\AA}$  channel is dominated by the Fe XVIII line and formed around  $6 \times 10^6$  K. The peak formation temperature of  $335\text{\AA}$  channel is  $2.5 \times 10^6$  K and dominant line is Fe XVI. Similarly  $211$  and  $171\text{\AA}$  channels are centered at Fe XIV, Fe IX and formed around  $1.9 \times 10^6$  and  $6.3 \times 10^5$ . For more details see Table 2.3.

The CHIANTI database provides the information about the theoretical values of the plasma properties. It is not possible to get the information about the multi-thermal plasma from CHIANTI atomic database. For this we need to compute the DEM by analysing the emission of all the EUV channels except the  $304\text{\AA}$  channel dominated by He II emission, which is optically thick and formed at lower temperature, therefore not used in DEM analysis (Boerner et al. 2012).

## 5.2 Observations and Data analysis

For the analysis, we have used the six EUV channels of AIA data (1.5 level) with a pixel size of  $0.6''$ . We have used the DEM code<sup>1</sup>, developed by Aschwanden et al. (2013) which is available on SolarSoft<sup>2</sup>. It gives the differential emission measure distributions at every

<sup>1</sup>[http://www.lmsal.com/aschwand/software/aia/aia\\_dem.html](http://www.lmsal.com/aschwand/software/aia/aia_dem.html)

<sup>2</sup>`SSW/packages/mjastereo/idl`

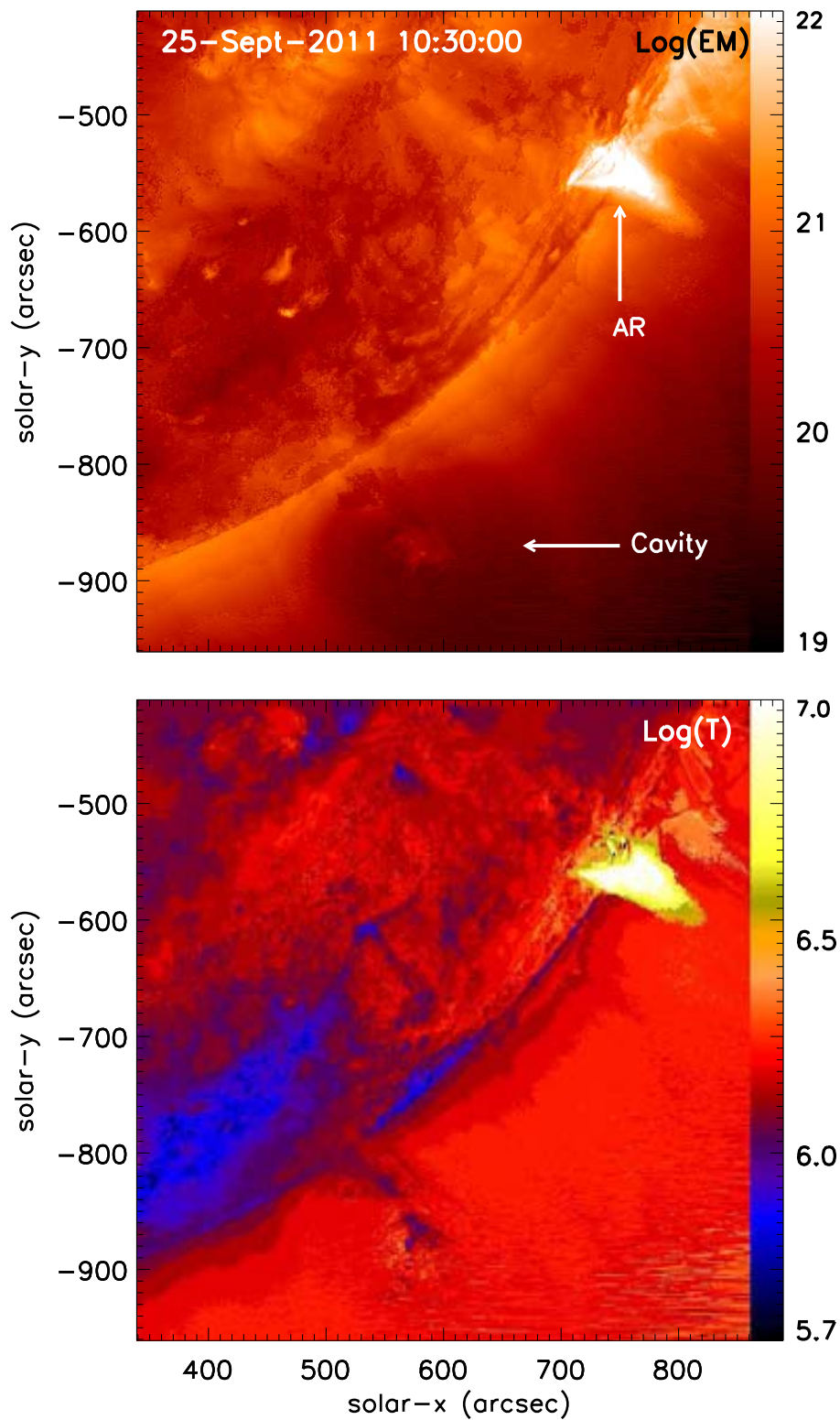


Figure 5.4: The peak emission and temperature map of the active region and the prominence tornado observed on 25 September 2011. The active region (AR) and cavity are indicated with an arrow.

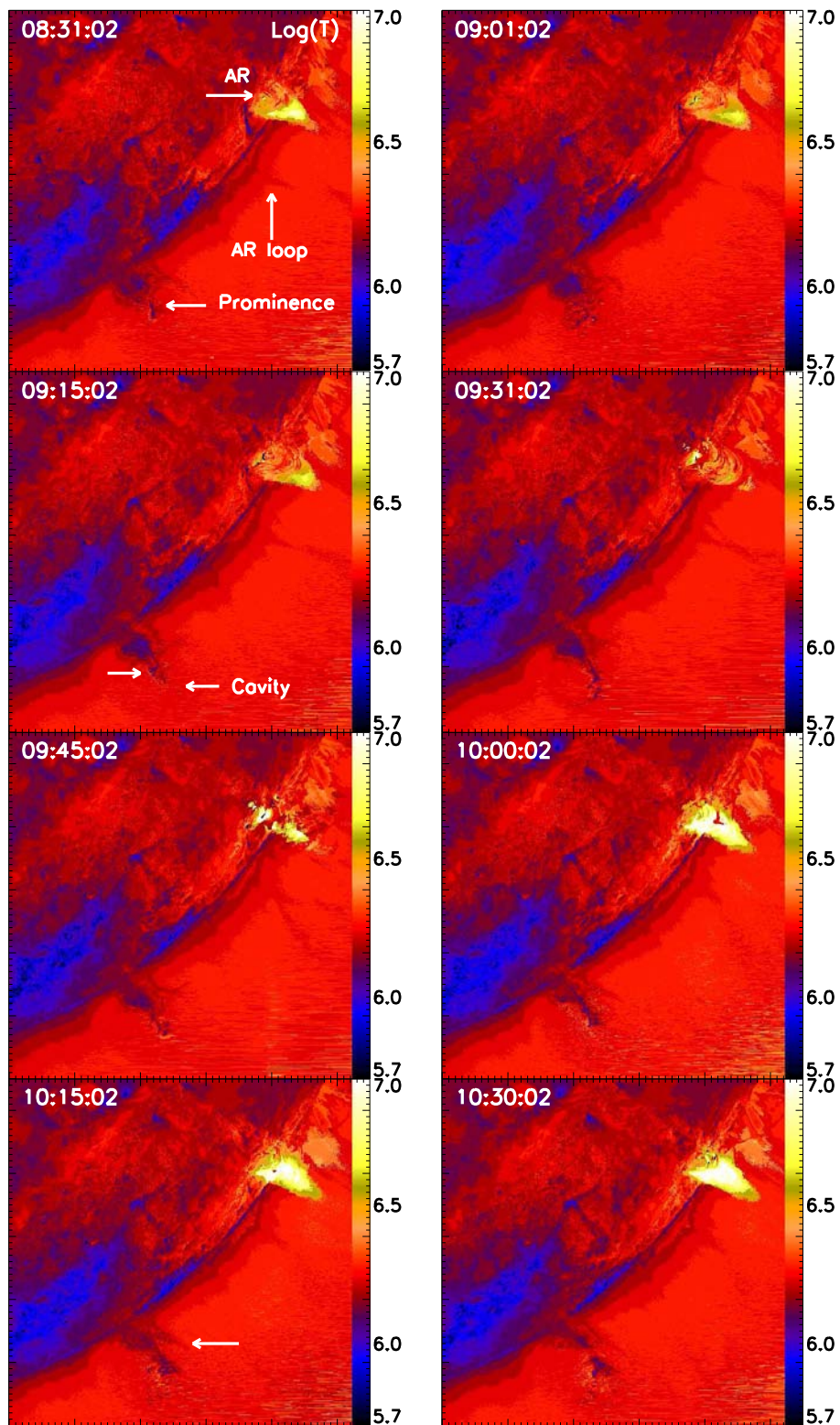


Figure 5.5: Temperature maps show the evolution of prominence-cavity system and active region (AR). Prominence, cavity and AR are indicated with arrows. The x and y axis are same as given in the Fig. 5.4.

pixel of the image and maps of most dominant temperature at peak emission along the line of sight.

For the analysis, we have selected the prominence-tornado and the neighbouring active region from 25 September 2011 (see Chapter 4). This is because we are interested in the thermal structure of the prominence cavity and of the surrounding corona including the active region.

### 5.2.1 DEM parametrization

To calculate the DEM, we select the EUV images from six different channels at  $\sim$  same time (10:30:02) from 25 September 2011. The observed flux or intensity value of the six AIA filters are estimated by fitting the fluxes to (Aschwanden and Acton 2001, Aschwanden 2002):

$$F_\lambda(x, y) = \int \frac{dEM(T, x, y)}{dT} R_\lambda(T) dT, \quad (5.8)$$

Where  $F_\lambda(x, y)$  is the flux (in  $x$  and  $y$  position) in data number per second [ $\text{DN s}^{-1} \text{ pixel}^{-1}$ ], and  $R_\lambda(T)$  is the wavelength response function in units of  $\text{DN cm}^{-5} \text{ s}^{-1}$ .  $dEM/dT$  is the emission measurement in  $\text{cm}^{-5} \text{ K}^{-1}$ . It can be optimized to give the best fit to the observed fluxes, assuming a single Gaussian function with three free parameters - peak emission ( $EM_p$ ), peak temperature ( $T_p$ ) and temperature widths ( $\sigma_T$ ) for each pixel (or in macro-pixel).

$$\frac{dEM(T, x, y)}{dT} = EM_p(x, y) \exp \left[ -\frac{(\log(T) - \log(T_p(x, y)))^2}{2\sigma_T^2(x, y)} \right], \quad (5.9)$$

By using this method, we can get a DEM peak emission measure value ( $EM_p(x, y)$ ) and DEM peak temperature ( $T_p(x, y)$ ) at each pixel for a given line of sight and an estimation of the temperature spread,  $\sigma_T$ . For simplicity, we call the resulting distributions a temperature map and emission map. The total emission measure (TEM) along the line-of-sight can be calculated by taking the integral over the entire temperature range, as shown in Equation 5.6. In this work, we do not computed the TEM.

First, the code calculates the Gaussian DEM model fluxes (see Equation 5.8) from a estimate of  $EM_p$ ,  $T_p$  and  $\sigma_T$ . Then the modelled DEM fluxes are compared to the observed flux values in each pixel position. The best-fit values of  $EM_p$ ,  $T_p$  and  $\sigma_T$  are obtained.

## 5.3 Results and Discussion

Fig. 5.3, shows the full temperature map [ $T_p(x, y)$ ] and emission map [ $EM_p(x, y)$ ] for 25 September 2011 at 10:30 UT. The vertical bar in temperature and emission map represents the temperature range in log scale ( $\log(T) = 5.7 - 7.0$  or  $0.5 - 10$  MK) and the emission in log scale (in units  $\text{cm}^{-5} \text{ K}^{-1}$ ). In temperature map, we can see that the coronal hole in the southern hemisphere represents the coolest temperature of  $\sim 0.5$  MK. The active region shows the highest temperature between  $3.9 - 7.9$  MK. Similarly the emission map shows the less emission for coronal hole ( $\sim 10^{20} \text{ cm}^{-5} \text{ K}^{-1}$ ) and peak emission for an active region ( $\sim 10^{22} \text{ cm}^{-5} \text{ K}^{-1}$ ).

### 5.3.1 DEM for prominence-cavity system

In the above Section 5.3, we show the full-Sun temperature maps which is rebinned with  $4 \times 4$  micro-pixels ( $1024 \times 1024$ ). Then the temperature maps are calculated for the prominence-cavity system and nearby active region. This is the tornado-like prominence which is triggered by the flares from the nearby active region. A detailed analysis of the tornado is shown in the Chapter 4. We apply this technique to the prominence system, to study the temperature structure of the prominence at different times e.g. during activation and before activation. To also see the difference between the various AIA maps and DEM maps, i.e. what additional information we can get from the temperature and emission maps, we have also computed AIA 193/171 and 131/94 intensity ratio images.

#### 5.3.1.1 Peak temperature map of the prominence-system

For the prominence-cavity system, we choose the small field of view,  $340 < x < 900$ ,  $-940 < y < -400$  arcsec. The temperature map for the full resolution of a sub-section is shown in Fig. 5.4. It shows the detailed temperature information for the prominence-cavity system, active region and surrounding active region corona. It does not mean that plasma is isothermal for any pixel position, the map shows the most dominant temperature at peak emission in each pixel along the line-of-sight. We notice the following:

- The core of the active region is the hottest feature with temperature of  $\sim 8 - 10$  MK (in white colour, see bottom image of Fig. 5.4). The outer layers of the active region show the temperature of  $3.9 - 6.3$  MK (in yellow-greenish colour). Our results for an active region are in agreement with those obtained by Aschwanden et al. (2013).
- The prominence shows relatively lower temperature (i.e. cool structure) than the surrounding ( $< 1$  MK). Which is in agreement with the cool structure of the prominences. It should be noted that the lowest limit of temperature accessible by the code is  $5 \times 10^5$  K. Which is higher than the estimated temperature of the prominence. Some structures of the prominence also show little bit high temperature near the rotating top of the prominence.
- An active region loop is also visible in the temperature map, which we mentioned in Chapter 4 in Fig. 4.7. The active region loop is cooler than the active region and the surrounding corona with a temperature of  $\sim 1 - 2$  MK. The temporal evolution of the loop can be seen in Fig. 5.5 and Fig. 5.6 (during the expansion and contraction of the active region loop).
- The region around the prominence, on the solar surface has a low temperature (in blue colour). We also see this as a dark region in 193 Å intensity images (Fig. 5.7). On the solar surface, both cool and hot structures are present.

#### 5.3.1.2 Peak emission measure of the prominence-system

The upper image in Fig. 5.4 shows the peak emission measure at peak temperature (bottom image of Fig. 5.4). It shows the regions where the emission is high and low along the line of sight. It can be clearly noticed that the prominence-cavity has less emission

of  $\sim 10^{20} \text{ cm}^{-5} \text{ K}^{-1}$ . The active region clearly shows the maximum emission in the high temperature core.

We also created sequence of intensity images for comparing the temperature and emission maps with it.

### 5.3.2 Comparison of the temperature maps with intensity images

For investigation of the evolution of prominence before and after the flare time, we calculated the temperature maps at every 15 minutes, see Fig. 5.5. The active region (NOAA 11303), active region loop and prominence are indicated with the arrows. There was a M1.4 class flare from the active region at  $\sim 09:40$  UT. The flare started at 09:20 UT and ended at 09:40 UT. We note that the core of the active region field has temperature of 3-5 MK before the flare and the temperature increases after the flare (see Fig. 5.5). The pre-flare arcade show the temperature in the range of 5-6 MK (Fig. 5.5). During the flare at 09:31 UT, temperature reached above 10 MK (Fig. 5.10 which is not resolved by the DEM (Fig. 5.5). Because in DEM the upper limit of temperature is 10 MK. The 131/94 Å ratio images (Fig. 5.11) give a better illustration of the temperature structure in the arcade.

We also note that the active region arcade expands after the flare, and develops a bright, dynamic post flare arcade with a temperature range of  $\sim 11-12$  MK. The AIA 131 Å intensity images show up the increased emission in the post flare arcade whereas the 94 Å images show relatively less emission in the arcade (Fig. 5.9). The temperature difference between both the channels can be seen in 131/94 Å ratio images (see Fig. 5.11 at 10:00 UT, bright structure shows the hotter active region loops). Usually the arcade starts forming just after the flare and it remains discernable for many hours (McKenzie and Hudson 1999, Innes et al. 2003).

As mentioned above, the active region loop is also visible in the temperature range of  $\sim 1.5 - 2$  MK (see Fig. 5.5 at 08:31 UT, indicated with an arrow). We can see the expansion of the active region loop after the flare (in Fig. 5.5 and Fig. 5.6 at 09:45 UT) and it moves back towards the flare site at 10:30 UT after hitting the cavity boundary.

The cavity is barely visible in the DEM temperature maps, (indicated with an arrow) but we noticed that the cavity has almost similar temperature ( $\sim 1.5$  MK) to an active region loop. We can clearly see in Fig. 5.4 (upper panel) that the cavity is a region of reduced emission. The AIA 171, 193 Å images show the dark cavity surrounding the prominence (see Fig. 5.6 and Fig. 5.7 at 09:15 UT). We also create a ratio image of 193 to 171 Å (see Fig. 5.8) to see difference in the temperature structure of the cavity. The ratio of the two images reflects the changes in the cavity structure. It shows that the inner part of the cavity has relatively less temperature than its outer edge/boundary. The cavity has a bright sharp outer boundary with high temperature, indicated with an arrow in Fig. 5.8 at 09:15 UT.

The main body of the prominence shows the coolest temperature (in blue colour, see Fig. 5.4) of  $< 1$  MK whereas the other parts of the prominence are slightly hotter (in dark red colour) e.g. the plasma which is extending from right hand side of the main body towards the active region (see Fig. 5.5 and Fig. 5.6 at 10:15 UT, indicated with an arrow). In 171 Å intensity images, we can see that bright tornado developed on the top of the prominence after the flare, from 10:00 - 10:30 UT in Fig. 5.6. At the same time, in Fig. 5.5 there is no such difference can be seen in the temperature on the top of the



prominence. A thin bright string is visible with a temperature of  $\sim 2$  MK at 09:15 UT, in Fig. 5.5 at 09:15 UT which could be caused by some reconnection occurring in the field lines. A thin bright string is also visible in the  $171\text{\AA}$  intensity images, e.g. indicated with an arrow at 09:15 UT. The ratio images clearly exhibit the temperature difference between the cool and hot plasma (indicated with the arrows).

After doing the initial study of the DEM by applying it on prominence and active region, we can say that DEM is a useful tool to investigate the thermal structure of coronal features. However, it gives more extensive information on the structures with large temperature ranges e.g. active regions than the prominences. We get all the temperatures of six filters in one map, but for prominences it appears partially helpful because of their small temperature range. In the future we would like to apply this technique on erupting prominences related with flares and CME's where larger temperature ranges are found to be present. The SDO/AIA provides the images in ten different wavelengths but to improve the DEM information we need even more wavelength channels covering a broader temperature range.

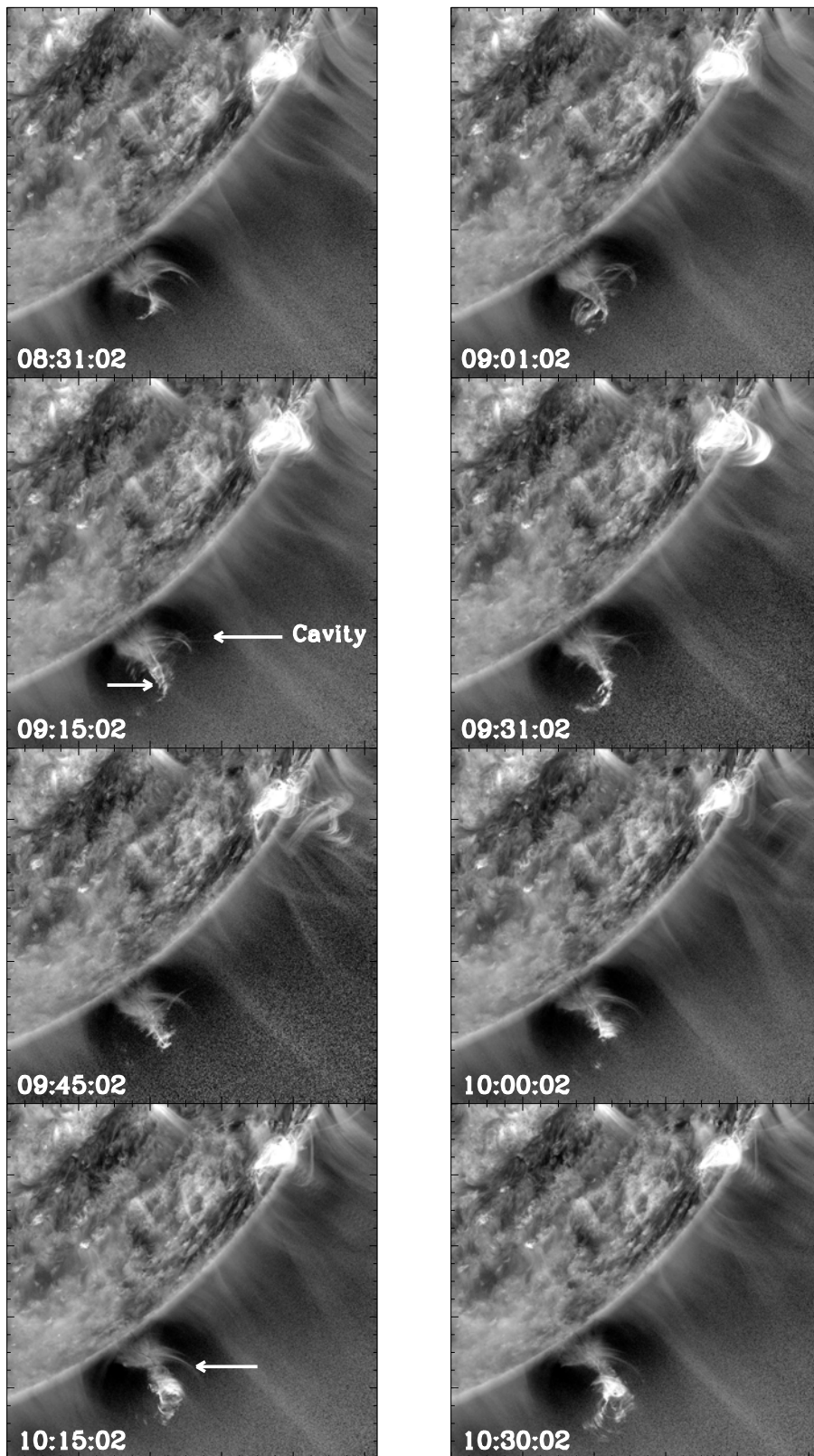


Figure 5.6: The SDO/AIA 171 Å intensity images show the region around prominence and active region at different times. A cavity and bright string is indicated with an arrow at 09:15 UT. An arm-like extension of the prominence plasma towards the active region is marked by an arrow at 10:15 UT. The x and y axis are same as given in the Fig. 5.4..

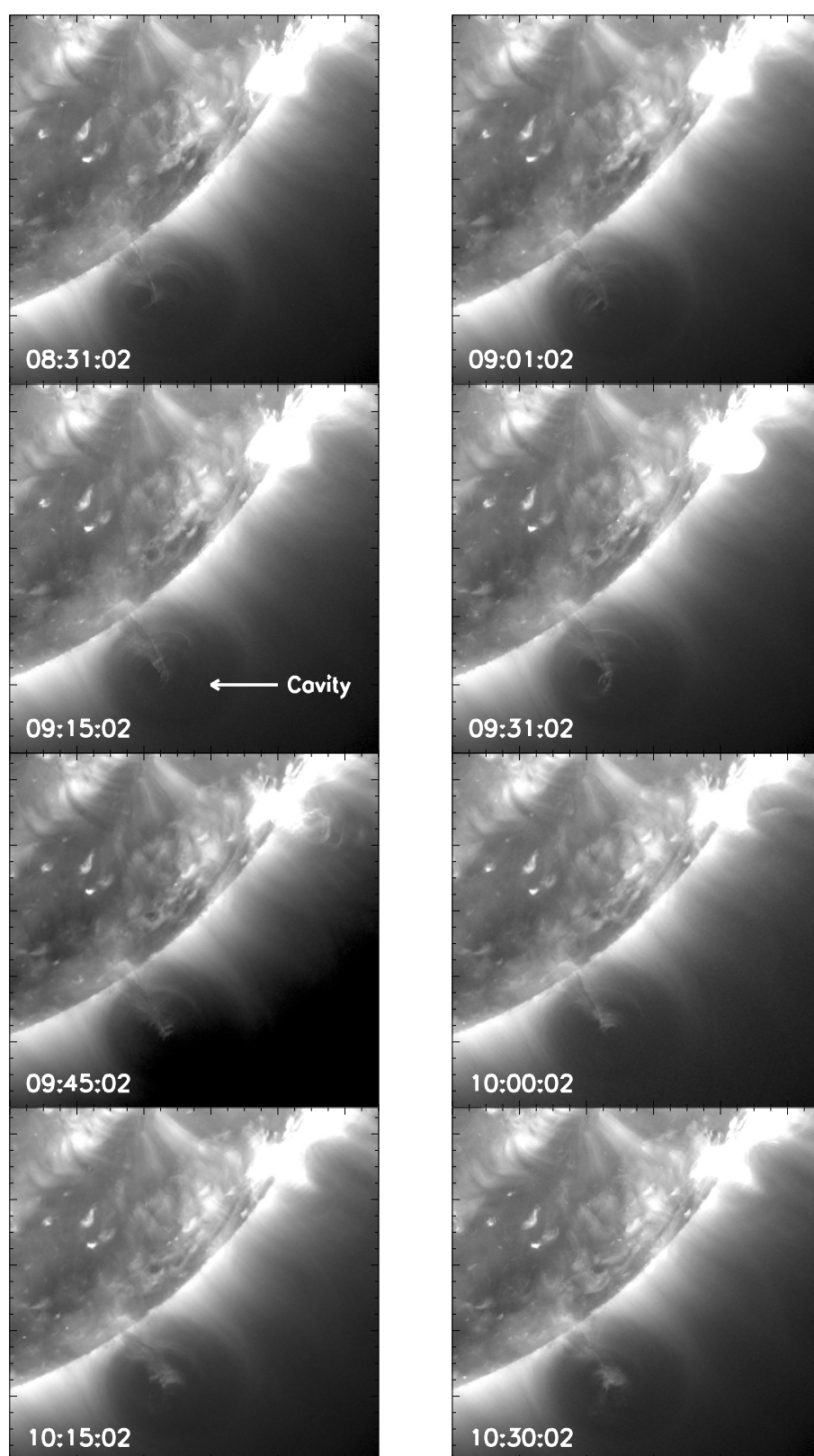


Figure 5.7: The SDO/AIA 193 Å intensity images show the dark cavity (marked with an arrow) surrounding the prominence and the active region. The x and y axis are same as given in the Fig. 5.4.

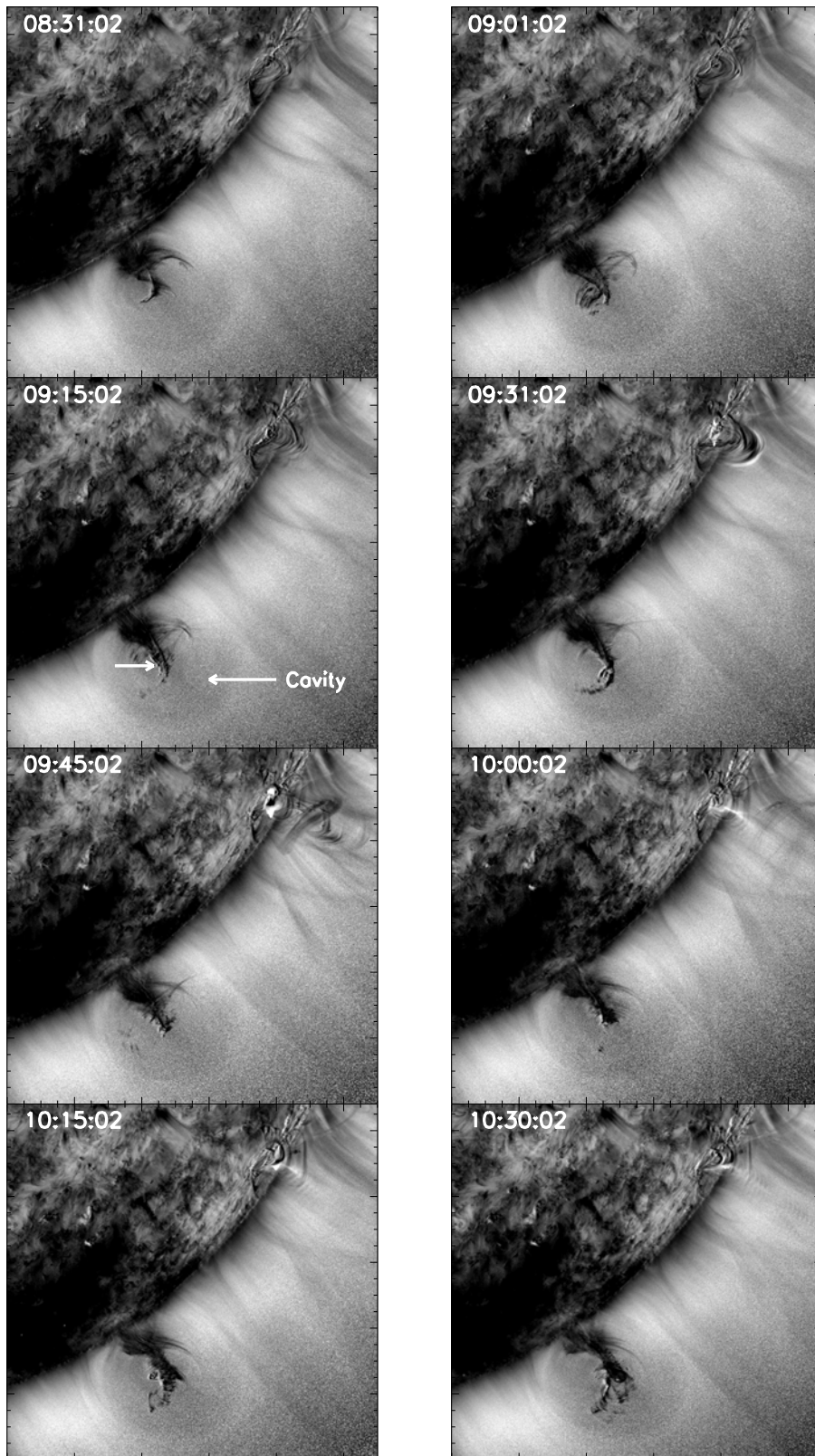


Figure 5.8: The SDO/AIA 193/171 Å ratio images show the region around prominence and active region at different times. The arrow indicated the cavity and bright string at 09:15 UT. The bright outer boundary of the cavity is visible in all images. The x and y axis are same as given in the Fig. 5.4.

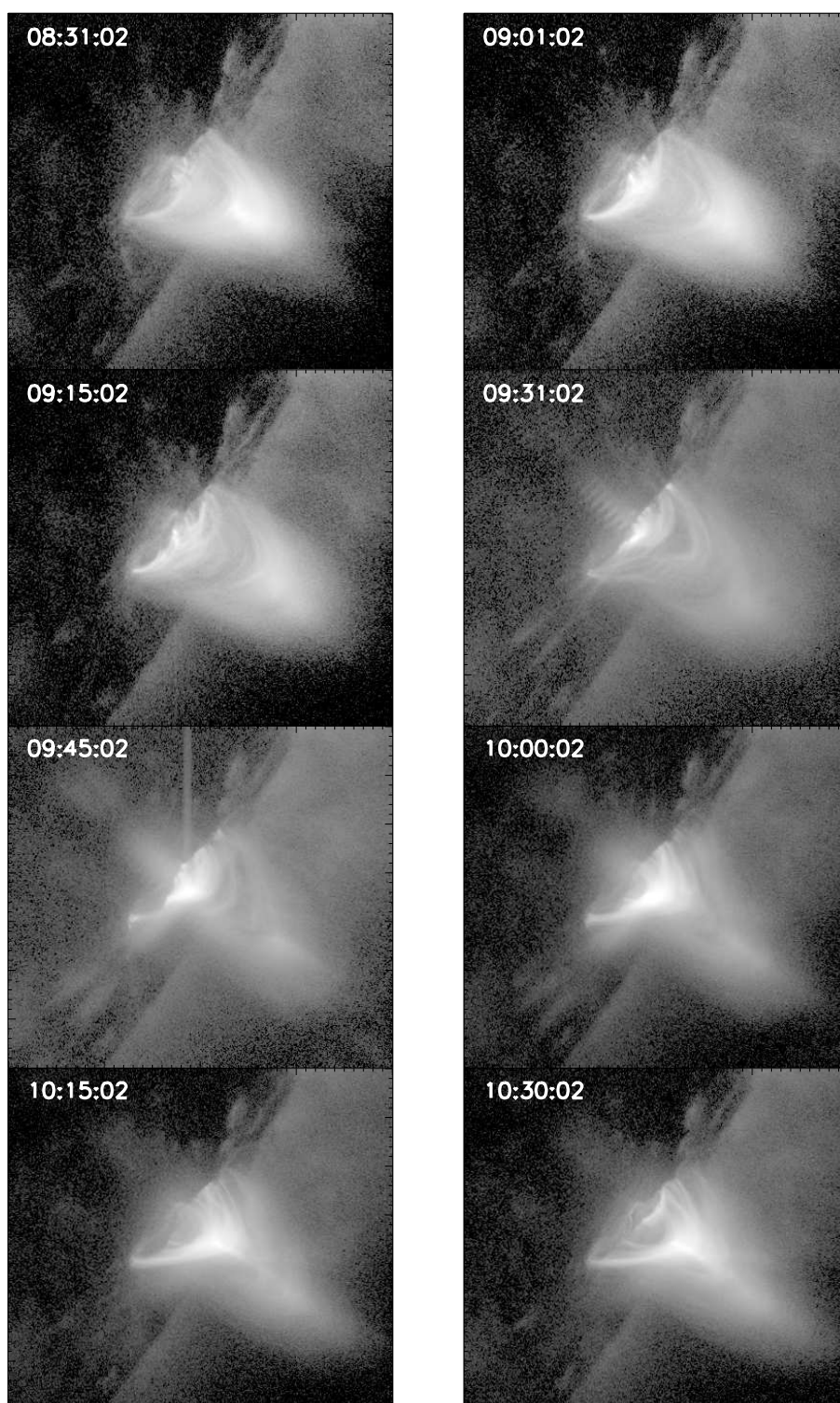


Figure 5.9: The SDO/AIA 94 Å intensity images show the region around active region at different times. These are the close-up images of an active region.

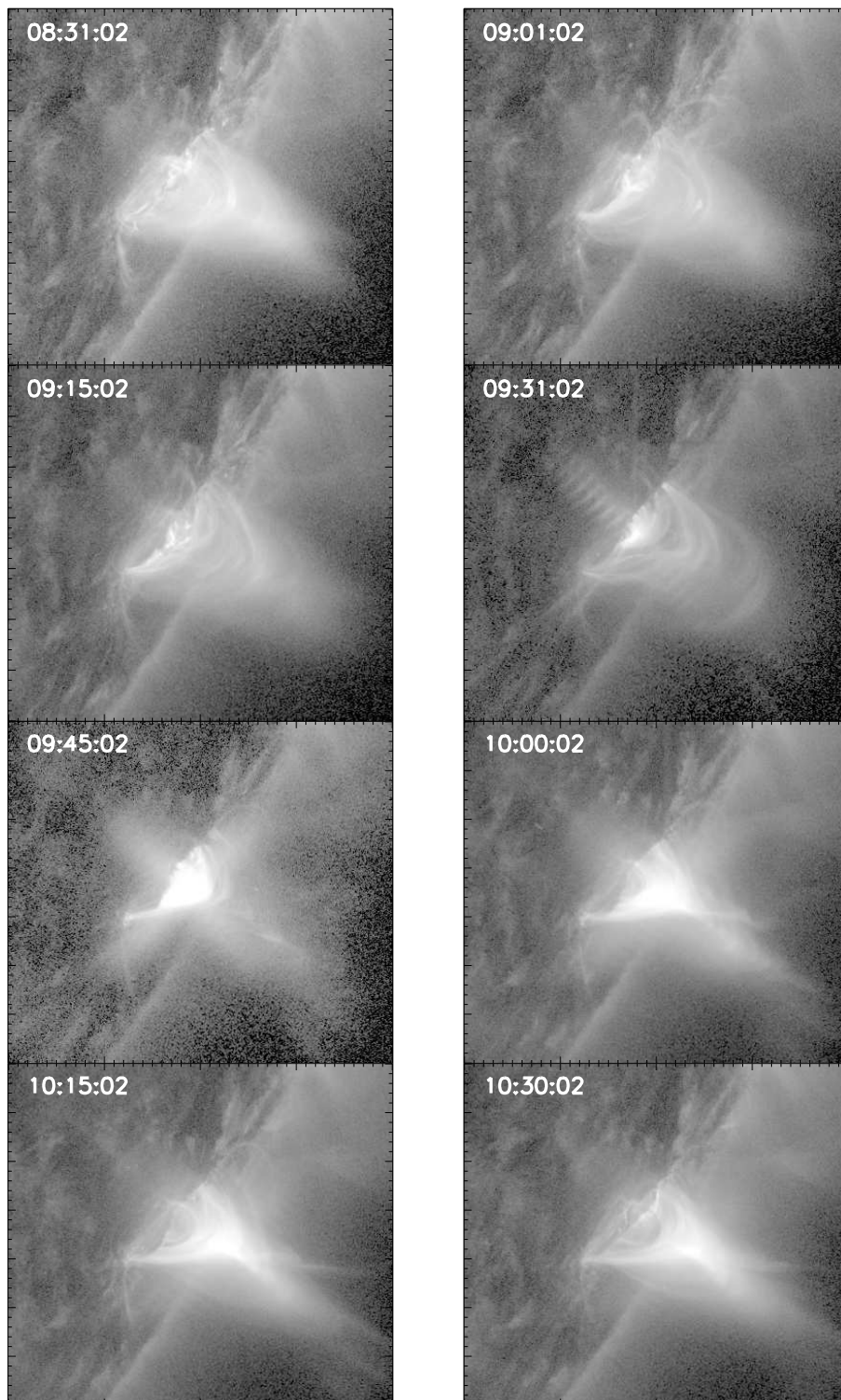


Figure 5.10: The SDO/AIA 131 Å intensity images show the region around active region at different times. These are the close-up images of an active region.

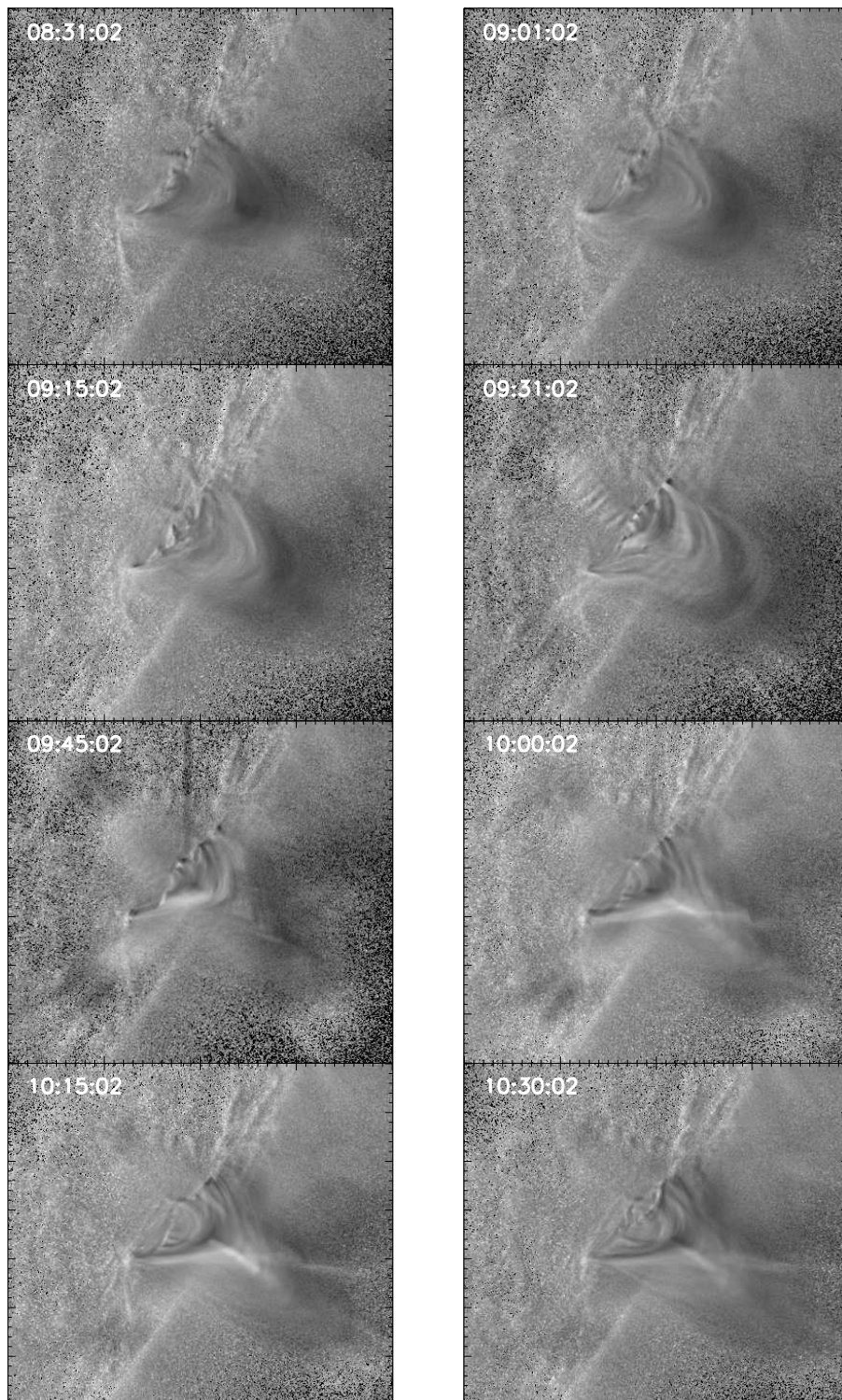


Figure 5.11: The SDO/AIA 131/94 Å ratio images are showing the evolution of the active region site at different times. These are the close-up images of an active region.





## 6 Summary and outlook

In this thesis, the structure and dynamics of two quiescent prominences are investigated. For this purpose, the high temporal cadence data with high spatial resolution from the Solar Dynamic Observatory (SDO), and the Solar Terrestrial Relations Observatory (STEREO) are used. During the study, SDO observed along the Earth-Sun line and the STEREO spacecraft were about  $90^\circ$  apart. The prominences observed by SDO on limb and STEREO-A on disk, simultaneously, were studied. The main aim of the present thesis is to study the structure, dynamics and flow patterns of the plasma in the prominences by combining the observation from two directions (SDO and STEREO). The two different types of quiescent prominences are investigated - a polar crown prominence and a tornado-type prominence.

1. Chapter 3 shows the study of a polar crown prominence, observed by the SDO/AIA on the north-west solar limb and seen as a filament channel by the STEREO-A on the solar disk. The SDO/AIA 304,  $171\text{\AA}$  images are used to study and track the flows in the prominence. The  $193\text{\AA}$  AIA images are used to compare the sites of brightenings and prominence structure with the STEREO-A  $195\text{\AA}$  disk images. First, the three prominence pillars on the STEREO disk images and four sites of persistent brightenings are identified. The dynamics of a small polar crown prominence at such a high latitude ( $60\text{-}70^\circ$ ) is very interesting because off-limb prominence plasma is connected to the different prominence pillars which are hundreds of arc seconds away from each other when observed on-disk. During the two days of observations, it has been noticed that the flows in one of the prominence pillars are triggered by the microflaring at the prominence footpoint. These flows stop abruptly at a sharp concave edge in the corona which indicates the presence of a coronal cavity suggestive of the presence of two different magnetic flux systems. On the intensity disk images, the dark cavity coincided with a dark region in a filament channel. With a STEREO  $195\text{\AA}$  running difference time series across the filament channel, a dark region of cavity shows no variation in it. Thus, it is concluded that the dark region could be a disk signature of a coronal cavity.

One of the prominence pillars shows strong upflows in it for two days. These upflows in the polar crown prominence itself are very interesting because typically quiescent prominences contain downflows. These upflows (of  $15\text{ km s}^{-1}$ ) seem to be driven by the heating at the prominence footpoint, which drive the plasma upwards. The main prominence pillar shows the dominant downflow with an average velocity of  $15.5\text{ km s}^{-1}$ . These downflows seem to be the result of cool, condensed chromospheric plasma that is falling down due to gravity. The observation suggests

that the prominence plasma is moving with the sound speed which is expected to be of the order of  $10 \text{ km s}^{-1}$ .

Our observation of the polar crown prominence is in agreement with the flux linkage model of the polar crown prominences (Martens and Zwaan 2001). To get information about the magnetic structure of the prominence-filament system, line-of-sight magnetograms from GONG and SDO/HMI are used (when the filament channel was on the SDO disk center). To the south west of the filament channel, a strong patch of positive diffused active region flux has been observed. It seems that the presence of the positive flux is the reason of several brightenings caused by magnetic reconnection in the filament channel where negative flux dominates. The brightenings occurred due to flux linkage which also lead to the injection of plasma in the prominence pillar. The observations give detailed information of the complex magnetic geometries in the polar crown prominences and also show how the polar crown prominences create a longer chain of pillars at the poles of the Sun. More detailed information of this work is presented in Chapter 3, see also Panesar et al. (2014a).

2. Chapter 4 shows the investigation of the triggering mechanism of a tornado-like prominence. A prominence was observed by the SDO/AIA on the south-west solar limb and it appeared at disk center in STEREO-A images. The AIA  $171\text{\AA}$  high cadence images are used to study the dynamics of the tornado and EUVI  $195\text{\AA}$  images are used for the analysis of the prominence tornado on the disk. An active region (NOAA 11303) was observed near to the prominence-cavity system. There were three M-class flares from the neighbouring active region and all the three flares created disturbances in the prominence-cavity system. EUV waves were observed after all the flares. The first flare produced an oscillation in the prominence. Tornado-like rotations are initiated after the second flare and the tornado gets accelerated after the third flare. The prominence cavity expands towards the active region site, resulting in the growth of helical field which creates a solar tornado on the top of the prominence. A plausible mechanism for the prominence expansion is the contraction of the active region field after the flare due to the loss of magnetic free energy, also known as the Hudson Effect (Hudson 2000). The cavity expanded due to its superior magnetic pressure to fill the surrounding corona which results in the expansion of the helical field lines and the appearance of the tornado. More detailed information of this work is given in Chapter 4 and in Panesar et al. (2013).
3. Chapter 5 represents the ongoing work on the multi-thermal study of the region around the tornado-like prominence by using differential emission measurement (DEM) (Aschwanden et al. 2013). For this work, the SDO/AIA EUV images have been used. The DEM technique has been applied during the third flare when the tornado-like activity got started. A high temperature of  $\sim 10 \text{ MK}$  has been observed in the post flare active region. The active region loop extends out towards the prominence cavity with a temperature of  $2 \text{ MK}$ . The prominence cavity had a slightly lower temperature  $\sim 1.5 \text{ MK}$ . The prominence plasma could not be prop-

erly analysed by this technique because it was clearly cooler than the minimum temperature accessible i.e.  $< 10^5$  K.

In future, I will apply this technique to the cavities, loops and erupting prominences for getting the multi - thermal stratification before, during and after the eruptions, when large temperature variations are seen where the DEM can suitably be applied.

Furthermore, I plan to study the structure and dynamics of erupting prominences which are known as the indirect indicators of the coronal mass ejections (CMEs). The major source of space weather problem is the physical effect of solar eruptions such as CMEs on the Earth's magnetosphere. The majority of CMEs are associated with the erupting prominences. For the study of the erupting prominences, SDO data will be used together with the STEREO data for constructing the 3-D geometry of the erupting plasma, in similar way as I have already done in this thesis work for quiescent prominences. Some questions should be addressed: for example - what are the critical conditions for the initiation of filament eruptions that can lead to a CME? How the non-equilibrium is reached leading to the eruption?

Moreover, I also plan to study the structure and dynamics of more prominence tornadoes from two different directions (SDO and STEREO). For this I will study those tornadoes observed when SDO and STEREO were at  $90^\circ \pm 20^\circ$  viewing angles to each other, as I have already done in the present thesis.

In addition, it will be interesting to study the prominence structure and flows on the solar disk by using high resolution AIA images and simultaneously from the STEREO limb images. Then the SDO/HMI data can also be used to understand the magnetic configuration of the prominences.



# Bibliography

- Ambrož, P., Schroll, A., 2002, Proper motion of solar filaments, *A&A*, 381, 300–310
- Antiochos, S. K., Klimchuk, J. A., 1991, A model for the formation of solar prominences, *ApJ*, 378, 372–377
- Antiochos, S. K., Dahlburg, R. B., Klimchuk, J. A., 1994, The magnetic field of solar prominences, *ApJ*, 420, L41–L44
- Antiochos, S. K., MacNeice, P. J., Spicer, D. S., Klimchuk, J. A., 1999, The Dynamic Formation of Prominence Condensations, *ApJ*, 512, 985–991, [arXiv:astro-ph/9808199](https://arxiv.org/abs/astro-ph/9808199)
- Antiochos, S. K., MacNeice, P. J., Spicer, D. S., 2000, The Thermal Nonequilibrium of Prominences, *ApJ*, 536, 494–499
- Anzer, U., 1994, Remarks on two-dimensional magnetic arcade models of coronal structures., in *IAU Colloq. 144: Solar Coronal Structures*, (Eds.) V. Rusin, P. Heinzel, J.-C. Vial, pp. 309–314
- Anzer, U., Heinzel, P., 2005, On the Nature of Dark Extreme Ultraviolet Structures Seen by SOHO/EIT and TRACE, *ApJ*, 622, 714–721
- Archontis, V., Török, T., 2008, Eruption of magnetic flux ropes during flux emergence, *A&A*, 492, L35–L38, 0811.1134
- Aschwanden, M. J., 2002, The Differential Emission Measure Distribution in the Multi-loop Corona, *ApJ*, 580, L79–L83
- Aschwanden, M. J., 2004, *Physics of the Solar Corona. An Introduction*, Praxis Publishing Ltd
- Aschwanden, M. J., Acton, L. W., 2001, Temperature Tomography of the Soft X-Ray Corona: Measurements of Electron Densities, Temperatures, and Differential Emission Measure Distributions above the Limb, *ApJ*, 550, 475–492
- Aschwanden, M. J., Schrijver, C. J., Alexander, D., 2001, Modeling of Coronal EUV Loops Observed with TRACE. I. Hydrostatic Solutions with Nonuniform Heating, *ApJ*, 550, 1036–1050

- Aschwanden, M. J., Wülser, J.-P., Nitta, N. V., Lemen, J. R., 2008, First Three-Dimensional Reconstructions of Coronal Loops with the STEREO A and B Spacecraft. I. Geometry, *ApJ*, 679, 827–842
- Aschwanden, M. J., Boerner, P., Schrijver, C. J., Malanushenko, A., 2013, Automated Temperature and Emission Measure Analysis of Coronal Loops and Active Regions Observed with the Atmospheric Imaging Assembly on the Solar Dynamics Observatory (SDO/AIA), *Solar Phys.*, 283, 5–30
- Attie, R., Innes, D. E., Potts, H. E., 2009, Evidence of photospheric vortex flows at supergranular junctions observed by FG/SOT (Hinode), *A&A*, 493, L13–L16, 0811.3445
- Aulanier, G., Demoulin, P., 1998, 3-D magnetic configurations supporting prominences. I. The natural presence of lateral feet, *A&A*, 329, 1125–1137
- Aulanier, G., DeVore, C. R., Antiochos, S. K., 2002, Prominence Magnetic Dips in Three-Dimensional Sheared Arcades, *ApJ*, 567, L97–L101
- Babcock, H. W., 1961, The Topology of the Sun's Magnetic Field and the 22-YEAR Cycle., *ApJ*, 133, 572
- Babcock, H. W., Babcock, H. D., 1955, The Sun's Magnetic Field, 1952-1954., *ApJ*, 121, 349
- Bak-Stęślicka, U., Gibson, S. E., Fan, Y., Bethge, C., Forland, B., Rachmeler, L. A., 2013, The Magnetic Structure of Solar Prominence Cavities: New Observational Signature Revealed by Coronal Magnetometry, *ApJ*, 770, L28, 1304.7388
- Berger, T., Testa, P., Hillier, A., Boerner, P., Low, B. C., Shibata, K., Schrijver, C., Tarbell, T., Title, A., 2011, Magneto-thermal convection in solar prominences, *Nature*, 472, 197–200
- Berger, T. E., Shine, R. A., Slater, G. L., Tarbell, T. D., Title, A. M., Okamoto, T. J., Ichimoto, K., Katsukawa, Y., Suematsu, Y., Tsuneta, S., Lites, B. W., Shimizu, T., 2008, Hinode SOT Observations of Solar Quiescent Prominence Dynamics, *ApJ*, 676, L89–L92
- Berger, T. E., Liu, W., Low, B. C., 2012, SDO/AIA Detection of Solar Prominence Formation within a Coronal Cavity, *ApJ*, 758, L37, 1208.3431
- Boerner, P., Edwards, C., Lemen, J., Rausch, A., Schrijver, C., Shine, R., Shing, L., Stern, R., Tarbell, T., Title, A., Wolfson, C. J., Soufli, R., Spiller, E., Gullikson, E., McKenzie, D., Windt, D., Golub, L., Podgorski, W., Testa, P., Weber, M., 2012, Initial Calibration of the Atmospheric Imaging Assembly (AIA) on the Solar Dynamics Observatory (SDO), *Solar Phys.*, 275, 41–66
- Bruner, M. E., McWhirter, R. W. P., 1988, Radiating properties of solar plasmas, *ApJ*, 326, 1002–1016
- Cartledge, N. P., Titov, V. S., 1996, The Structure of a Prominence Sheet, *Solar Phys.*, 169, 55–67

- Cartledge, N. P., Titov, V. S., Priest, E. R., 1996, A 2-D model for the support of a polar-crown solar prominence, *Solar Phys.*, 166, 287–310
- Chae, J., 2003, The Formation of a Prominence in NOAA Active Region 8668. II. Trace Observations of Jets and Eruptions Associated with Canceling Magnetic Features, *ApJ*, 584, 1084–1094
- Chae, J., Wang, H., Qiu, J., Goode, P. R., Strous, L., Yun, H. S., 2001, The Formation of a Prominence in Active Region NOAA 8668. I. SOHO/MDI Observations of Magnetic Field Evolution, *ApJ*, 560, 476–489
- Chae, J., Moon, Y.-J., Park, Y.-D., 2005, The Magnetic Structure of Filament Barbs, *ApJ*, 626, 574–578
- Chae, J., Ahn, K., Lim, E.-K., Choe, G. S., Sakurai, T., 2008, Persistent Horizontal Flows and Magnetic Support of Vertical Threads in a Quiescent Prominence, *ApJ*, 689, L73–L76
- Chandrasekhar, S., 1961, Hydrodynamic and hydromagnetic stability
- Chandrasekhar, S., Kendall, P. C., 1957, On Force-Free Magnetic Fields., *ApJ*, 126, 457
- Cheimets, P., Caldwell, D. C., Chou, C., Gates, R., Lemen, J., Podgorski, W. A., Wolfson, C. J., Wuelser, J.-P., 2009, SDO-AIA telescope design, in Society of Photo-Optical Instrumentation Engineers (SPIE) Conference Series, vol. 7438 of Society of Photo-Optical Instrumentation Engineers (SPIE) Conference Series
- Couvidat, S., Schou, J., Shine, R. A., Bush, R. I., Miles, J. W., Scherrer, P. H., Rairden, R. L., 2012, Wavelength Dependence of the Helioseismic and Magnetic Imager (HMI) Instrument onboard the Solar Dynamics Observatory (SDO), *Solar Phys.*, 275, 285–325
- Craig, I. J. D., Brown, J. C., 1976, Fundamental limitations of X-ray spectra as diagnostics of plasma temperature structure, *A&A*, 49, 239–250
- Dahlburg, R. B., Antiochos, S. K., Klimchuk, J. A., 1998, Prominence Formation by Localized Heating, *ApJ*, 495, 485
- de Jager, C., 1959, Structure and Dynamics of the Solar Atmosphere., *Handbuch der Physik*, 52, 80
- Del Zanna, G., O’Dwyer, B., Mason, H. E., 2011, SDO AIA and Hinode EIS observations of ”warm” loops, *A&A*, 535, A46
- Delaboudinière, J.-P., Artzner, G. E., Brunaud, J., Gabriel, A. H., Hochedez, J. F., Millier, F., Song, X. Y., Au, B., Dere, K. P., Howard, R. A., Kreplin, R., Michels, D. J., Moses, J. D., Defise, J. M., Jamar, C., Rochus, P., Chauvineau, J. P., Marioge, J. P., Catura, R. C., Lemen, J. R., Shing, L., Stern, R. A., Gurman, J. B., Neupert, W. M., Maucherat, A., Clette, F., Cugnon, P., van Dessel, E. L., 1995, EIT: Extreme-Ultraviolet Imaging Telescope for the SOHO Mission, *Solar Phys.*, 162, 291–312

- Dere, K. P., Landi, E., Mason, H. E., Monsignori Fossi, B. C., Young, P. R., 1997, CHIANTI - an atomic database for emission lines, *A&AS*, 125, 149–173
- Dere, K. P., Landi, E., Young, P. R., Del Zanna, G., Landini, M., Mason, H. E., 2009, CHIANTI - an atomic database for emission lines. IX. Ionization rates, recombination rates, ionization equilibria for the elements hydrogen through zinc and updated atomic data, *A&A*, 498, 915–929
- Deslandres, H., 1909, On the progressive revelation of the entire atmosphere of the Sun, *The Observatory*, 32, 282–287
- DeVore, C. R., Antiochos, S. K., 2000, Dynamical Formation and Stability of Helical Prominence Magnetic Fields, *ApJ*, 539, 954–963
- Dikpati, M., Gilman, P. A., 2009, Flux-Transport Solar Dynamos, *Space Sci. Rev.*, 144, 67–75
- Dudík, J., Aulanier, G., Schmieder, B., Zapiór, M., Heinzel, P., 2012, Magnetic Topology of Bubbles in Quiescent Prominences, *ApJ*, 761, 9
- Engvold, O., 1976, The fine structure of prominences. I - Observations - H-alpha filtergrams, *Solar Phys.*, 49, 283–295
- Engvold, O., 1998, Observations of Filament Structure and Dynamics (Review), in *IAU Colloq. 167: New Perspectives on Solar Prominences*, (Ed.) D. F. Webb, B. Schmieder, & D. M. Rust, vol. 150 of *Astronomical Society of the Pacific Conference Series*, p. 23
- Fan, Y., 2009, Magnetic Fields in the Solar Convection Zone, *Living Reviews in Solar Physics*, 6, 4
- Feldman, U., Widing, K. G., 1993, Elemental abundances in the upper solar atmosphere of quiet and coronal hole regions (Te is approximately equal to  $4.3 \times 10^{-5}$  K), *ApJ*, 414, 381–388
- Forbes, T. G., 2000, A review on the genesis of coronal mass ejections, *Journal of Geophysical Research*, 105, 23 153–23 166
- Foukal, P., 1971a, Morphological Relationships in the Chromospheric H $\alpha$  Fine Structure, *Solar Phys.*, 19, 59–71
- Foukal, P., 1971b, H $\alpha$  Fine Structure and the Chromospheric Field, *Solar Phys.*, 20, 298–309
- Fuller, J., Gibson, S. E., 2009, A Survey of Coronal Cavity Density Profiles, *ApJ*, 700, 1205–1215
- Gaizauskas, V., 1998, Filament Channels: Essential Ingredients for Filament Formation (Review), in *IAU Colloq. 167: New Perspectives on Solar Prominences*, (Eds.) D. F. Webb, B. Schmieder, D. M. Rust, vol. 150 of *Astronomical Society of the Pacific Conference Series*, p. 257



- Gaizauskas, V., 2002, Formation of a Switchback During the Rising Phase of Solar Cycle 21, *Solar Phys.*, 211, 179–188
- Gaizauskas, V., Zirker, J. B., Sweetland, C., Kovacs, A., 1997, Formation of a Solar Filament Channel, *ApJ*, 479, 448
- Gaizauskas, V., Mackay, D. H., Harvey, K. L., 2001, Evolution of Solar Filament Channels Observed during a Major Poleward Surge of Photospheric Magnetic Flux, *ApJ*, 558, 888–902
- Gary, G. A., 2001, Plasma Beta above a Solar Active Region: Rethinking the Paradigm, *Solar Phys.*, 203, 71–86
- Gary, G. A., West, E. A., Rees, D., McKay, J. A., Zukic, M., Herman, P., 2007, Solar CIV vacuum-ultraviolet Fabry-Perot interferometers, *A&A*, 461, 707–722
- Gibson, S. E., Fan, Y., 2006, Coronal prominence structure and dynamics: A magnetic flux rope interpretation, *Journal of Geophysical Research (Space Physics)*, 111, A12103
- Gibson, S. E., Foster, D., Burkepile, J., de Toma, G., Stanger, A., 2006, The Calm before the Storm: The Link between Quiescent Cavities and Coronal Mass Ejections, *ApJ*, 641, 590–605
- Gibson, S. E., Kucera, T. A., Rastawicki, D., Dove, J., de Toma, G., Hao, J., Hill, S., Hudson, H. S., Marqué, C., McIntosh, P. S., Rachmeler, L., Reeves, K. K., Schmieder, B., Schmit, D. J., Seaton, D. B., Sterling, A. C., Tripathi, D., Williams, D. R., Zhang, M., 2010, Three-dimensional Morphology of a Coronal Prominence Cavity, *ApJ*, 724, 1133–1146
- Gilbert, H. R., Holzer, T. E., Burkepile, J. T., 2001, Observational Interpretation of an Active Prominence on 1999 May 1, *ApJ*, 549, 1221–1230
- Gold, T., 1964a, Magnetic Energy Shedding in the Solar Atmosphere, in *The Physics of Solar Flares*, (Ed.) W. N. Hess, p. 389
- Gold, T., 1964b, Magnetic Energy Shedding in the Solar Atmosphere, *NASA Special Publication*, 50, 389
- Gunár, S., Heinzl, P., Schmieder, B., Schwartz, P., Anzer, U., 2007, Properties of prominence fine-structure threads derived from SOHO/SUMER hydrogen Lyman lines, *A&A*, 472, 929–936
- Gunár, S., Heinzl, P., Anzer, U., Schmieder, B., 2008, On Lyman-line asymmetries in quiescent prominences, *A&A*, 490, 307–313
- Habbal, S. R., Druckmüller, M., Morgan, H., Scholl, I., Rušin, V., Daw, A., Johnson, J., Arndt, M., 2010, Total Solar Eclipse Observations of Hot Prominence Shrouds, *ApJ*, 719, 1362–1369

- Halain, J.-P., Berghmans, D., Defise, J.-M., Renotte, E., Thibert, T., Mazy, E., Rochus, P., Nicula, B., de Groof, A., Seaton, D., Schühle, U., 2010, First light of SWAP on-board PROBA2, in Society of Photo-Optical Instrumentation Engineers (SPIE) Conference Series, vol. 7732 of Society of Photo-Optical Instrumentation Engineers (SPIE) Conference Series
- Hale, G. E., Ellerman, F., 1903, The Rumford spectroheliograph of the Yerkes Observatory, Publications of the Yerkes Observatory, 3, 1–
- Hale, G. E., Nicholson, S. B., 1925, The Law of Sun-Spot Polarity, *ApJ*, 62, 270
- Hale, G. E., Ellerman, F., Nicholson, S. B., Joy, A. H., 1919, The Magnetic Polarity of Sun-Spots, *ApJ*, 49, 153
- Handy, B. N., Acton, L. W., Kankelborg, C. C., Wolfson, C. J., Akin, D. J., Bruner, M. E., Carvalho, R., Catura, R. C., Chevalier, R., Duncan, D. W., Edwards, C. G., Feinstein, C. N., Freeland, S. L., Friedlaender, F. M., Hoffmann, C. H., Hurlburt, N. E., Jurcevich, B. K., Katz, N. L., Kelly, G. A., Lemen, J. R., Levay, M., Lindgren, R. W., Mathur, D. P., Meyer, S. B., Morrison, S. J., Morrison, M. D., Nightingale, R. W., Pope, T. P., Rehse, R. A., Schrijver, C. J., Shine, R. A., Shing, L., Strong, K. T., Tarbell, T. D., Title, A. M., Torgerson, D. D., Golub, L., Bookbinder, J. A., Caldwell, D., Cheimets, P. N., Davis, W. N., Deluca, E. E., McMullen, R. A., Warren, H. P., Amato, D., Fisher, R., Maldonado, H., Parkinson, C., 1999, The transition region and coronal explorer, *Solar Phys.*, 187, 229–260
- Hannah, I. G., Kontar, E. P., 2012, Differential emission measures from the regularized inversion of Hinode and SDO data, *A&A*, 539, A146, 1201.2642
- Hannah, I. G., Kontar, E. P., 2013, Multi-thermal dynamics and energetics of a coronal mass ejection in the low solar atmosphere, *A&A*, 553, A10, 1212.5529
- Harvey, J. W., Hill, F., Hubbard, R. P., Kennedy, J. R., Leibacher, J. W., Pintar, J. A., Gilman, P. A., Noyes, R. W., Title, A. M., Toomre, J., Ulrich, R. K., Bhatnagar, A., Kennewell, J. A., Marquette, W., Patron, J., Saa, O., Yasukawa, E., 1996, The Global Oscillation Network Group (GONG) Project, *Science*, 272, 1284–1286
- Heinzel, P., Anzer, U., 2001, Prominence fine structures in a magnetic equilibrium: Two-dimensional models with multilevel radiative transfer, *A&A*, 375, 1082–1090
- Heinzel, P., Anzer, U., 2006, On the Fine Structure of Solar Filaments, *ApJ*, 643, L65–L68
- Heinzel, P., Anzer, U., Schmieder, B., 2003, A Spectroscopic Model of euv Filaments, *Solar Phys.*, 216, 159–171
- Heinzel, P., Schmieder, B., Fárnik, F., Schwartz, P., Labrosse, N., Kotrč, P., Anzer, U., Molodij, G., Berlicki, A., DeLuca, E. E., Golub, L., Watanabe, T., Berger, T., 2008, Hinode, TRACE, SOHO, and Ground-based Observations of a Quiescent Prominence, *ApJ*, 686, 1383–1396

- Hillier, A., van Ballegooijen, A., 2013, On the Support of Solar Prominence Material by the Dips of a Coronal Flux Tube, *ApJ*, 766, 126, 1303.4130
- Hirayama, T., 1985, Modern observations of solar prominences, *Solar Phys.*, 100, 415–434
- Howard, R., Harvey, J. W., 1964, Photospheric Magnetic Fields and Chromospheric Features., *ApJ*, 139, 1328
- Howard, R. A., Moses, J. D., Vourlidas, A., Newmark, J. S., Socker, D. G., Plunkett, S. P., Korendyke, C. M., Cook, J. W., Hurley, A., Davila, J. M., Thompson, W. T., St Cyr, O. C., Mentzell, E., Mehalick, K., Lemen, J. R., Wuelsel, J. P., Duncan, D. W., Tarbell, T. D., Wolfson, C. J., Moore, A., Harrison, R. A., Waltham, N. R., Lang, J., Davis, C. J., Eyles, C. J., Mapson-Menard, H., Simnett, G. M., Halain, J. P., Defise, J. M., Mazy, E., Rochus, P., Mercier, R., Ravet, M. F., Delmotte, F., Auchere, F., Delaboudiniere, J. P., Bothmer, V., Deutsch, W., Wang, D., Rich, N., Cooper, S., Stephens, V., Maahs, G., Baugh, R., McMullin, D., Carter, T., 2008, Sun Earth Connection Coronal and Heliospheric Investigation (SECCHI), *Space Science Reviews*, 136, 67
- Hudson, H. S., 2000, Implosions in Coronal Transients, *ApJ*, 531, L75–L77
- Hudson, H. S., Acton, L. W., Harvey, K. L., McKenzie, D. E., 1999a, A Stable Filament Cavity with a Hot Core, *ApJ*, 513, L83–L86
- Hudson, H. S., Acton, L. W., Harvey, K. L., McKenzie, D. E., 1999b, A Stable Filament Cavity with a Hot Core, *ApJ*, 513, L83–L86
- Hyder, C. L., 1965, The "polar Crown" of Filaments and the Sun's Polar Magnetic Fields., *ApJ*, 141, 272
- Inhester, B., 2006, Stereoscopy basics for the STEREO mission, *ArXiv Astrophysics e-prints*, [arXiv:astro-ph/0612649](https://arxiv.org/abs/astro-ph/0612649)
- Innes, D. E., McKenzie, D. E., Wang, T. J., 2003, SUMER spectral observations of post-flare supra-arcade inflows, *Solar Phys.*, 217, 247
- Janse, Å. M., Low, B. C., 2007, Coronal hydromagnetic implosions, *A&A*, 472, 957–965
- Jette, A., 1970, Force-free magnetic fields in resistive magnetohydrostatics, *Journal of Mathematical Analysis and Applications*, 29, 109 – 122, ISSN 0022-247X
- Karpen, J. T., Antiochos, S. K., Hohensee, M., Klimchuk, J. A., MacNeice, P. J., 2001, Are Magnetic Dips Necessary for Prominence Formation?, *ApJ*, 553, L85–L88
- Karpen, J. T., Antiochos, S. K., Klimchuk, J. A., MacNeice, P. J., 2003, Constraints on the Magnetic Field Geometry in Prominences, *ApJ*, 593, 1187–1194
- Kippenhahn, R., Schlüter, A., 1957, Eine Theorie der solaren Filamente. Mit 7 Textabbildungen, *ZAp*, 43, 36

- Kitiashvili, I. N., Kosovichev, A. G., Lele, S. K., Mansour, N. N., Wray, A. A., 2013, Ubiquitous Solar Eruptions Driven by Magnetized Vortex Tubes, *ApJ*, 770, 37, 1301.0018
- Klimchuk, J. A., Karpen, J. T., Antiochos, S. K., 2010, Can Thermal Nonequilibrium Explain Coronal Loops?, *ApJ*, 714, 1239–1248, 0912.0953
- Kucera, T. A., Andretta, V., Poland, A. I., 1998, Neutral Hydrogen Column Depths in Prominences Using EUV Absorption Features, *Solar Phys.*, 183, 107–121
- Kucera, T. A., Tovar, M., de Pontieu, B., 2003, Prominence Motions Observed at High Cadences in Temperatures from 10 000 to 250 000 K, *Solar Phys.*, 212, 81–97
- Kucera, T. A., Gibson, S. E., Schmit, D. J., Landi, E., Tripathi, D., 2012, Temperature and Extreme-ultraviolet Intensity in a Coronal Prominence Cavity and Streamer, *ApJ*, 757, 73
- Kuijpers, J., 1997, A Solar Prominence Model, *ApJ*, 489, L201, arXiv:astro-ph/9709178
- Kuperus, M., 1996, The Double Inverse Polarity Paradigm|The Sign of Magnetic Fields in Quiescent Prominences, *Solar Phys.*, 169, 349–356
- Kuperus, M., Raadu, M. A., 1974, The Support of Prominences Formed in Neutral Sheets, *A&A*, 31, 189
- Kuperus, M., Tandberg-Hanssen, E., 1967, The Nature of Quiescent Solar Prominences, *Solar Phys.*, 2, 39–48
- Labrosse, N., Heinzel, P., Vial, J.-C., Kucera, T., Parenti, S., Gunár, S., Schmieder, B., Kilper, G., 2010, Physics of Solar Prominences: Spectral Diagnostics and Non-LTE Modelling, *Space Sci. Rev.*, 151, 243–332, 1001.1620
- Leighton, R. B., 1969, A Magneto-Kinematic Model of the Solar Cycle, *ApJ*, 156, 1
- Lemen, J. R., Title, A. M., Akin, D. J., Boerner, P. F., Chou, C., Drake, J. F., Duncan, D. W., Edwards, C. G., Friedlaender, F. M., Heyman, G. F., Hurlburt, N. E., Katz, N. L., Kushner, G. D., Levay, M., Lindgren, R. W., Mathur, D. P., McFeaters, E. L., Mitchell, S., Rehse, R. A., Schrijver, C. J., Springer, L. A., Stern, R. A., Tarbell, T. D., Wuelser, J.-P., Wolfson, C. J., Yanari, C., Bookbinder, J. A., Cheimets, P. N., Caldwell, D., Deluca, E. E., Gates, R., Golub, L., Park, S., Podgorski, W. A., Bush, R. I., Scherrer, P. H., Gumm, M. A., Smith, P., Auken, G., Jerram, P., Pool, P., Soufli, R., Windt, D. L., Beardsley, S., Clapp, M., Lang, J., Waltham, N., 2012, The Atmospheric Imaging Assembly (AIA) on the Solar Dynamics Observatory (SDO), *Solar Phys.*, 275, 17–40
- Leroy, J. L., Bommier, V., Sahal-Brechot, S., 1984, New data on the magnetic structure of quiescent prominences, *A&A*, 131, 33–44
- Li, L., Zhang, J., 2013, The Evolution of Barbs of a Polar Crown Filament Observed by SDO, *Solar Phys.*, 282, 147–174

- Li, X., Morgan, H., Leonard, D., Jeska, L., 2012, A Solar Tornado Observed by AIA/SDO: Rotational Flow and Evolution of Magnetic Helicity in a Prominence and Cavity, *ApJ*, 752, L22, 1205.3819
- Liggett, M., Zirin, H., 1984, Rotation in prominences, *Solar Phys.*, 91, 259–267
- Lin, H., Kuhn, J. R., Coulter, R., 2004, Coronal Magnetic Field Measurements, *ApJ*, 613, L177–L180
- Lin, R. P., Dennis, B. R., Hurford, G. J., Smith, D. M., Zehnder, A., Harvey, P. R., Curtis, D. W., Pankow, D., Turin, P., Bester, M., Csillaghy, A., Lewis, M., Madden, N., van Beek, H. F., Appleby, M., Raudorf, T., McTiernan, J., Ramaty, R., Schmahl, E., Schwartz, R., Krucker, S., Abiad, R., Quinn, T., Berg, P., Hashii, M., Sterling, R., Jackson, R., Pratt, R., Campbell, R. D., Malone, D., Landis, D., Barrington-Leigh, C. P., Slassi-Sennou, S., Cork, C., Clark, D., Amato, D., Orwig, L., Boyle, R., Banks, I. S., Shirey, K., Tolbert, A. K., Zarro, D., Snow, F., Thomsen, K., Henneck, R., McHedlishvili, A., Ming, P., Fivian, M., Jordan, J., Wanner, R., Crubb, J., Preble, J., Matranga, M., Benz, A., Hudson, H., Canfield, R. C., Holman, G. D., Crannell, C., Kosugi, T., Emslie, A. G., Vilmer, N., Brown, J. C., Johns-Krull, C., Aschwanden, M., Metcalf, T., Conway, A., 2002, The Reuven Ramaty High-Energy Solar Spectroscopic Imager (RHESSI), *Solar Phys.*, 210, 3–32
- Lin, R. P., Krucker, S., Hurford, G. J., Smith, D. M., Hudson, H. S., Holman, G. D., Schwartz, R. A., Dennis, B. R., Share, G. H., Murphy, R. J., Emslie, A. G., Johns-Krull, C., Vilmer, N., 2003a, RHESSI Observations of Particle Acceleration and Energy Release in an Intense Solar Gamma-Ray Line Flare, *ApJ*, 595, L69–L76
- Lin, Y., Engvold, O. R., Wiik, J. E., 2003b, Counterstreaming in a Large Polar Crown Filament, *Solar Phys.*, 216, 109–120
- Lin, Y., Engvold, O. R., Wiik, J. E., 2003c, Counterstreaming in a Large Polar Crown Filament, *Solar Phys.*, 216, 109–120
- Lin, Y., Engvold, O., Rouppe van der Voort, L., Wiik, J. E., Berger, T. E., 2005a, Thin Threads of Solar Filaments, *Solar Phys.*, 226, 239–254
- Lin, Y., Wiik, J. E., Engvold, O., Rouppe van der Voort, L., Frank, Z. A., 2005b, Solar Filaments and Photospheric Network, *Solar Phys.*, 227, 283
- Lin, Y., Engvold, O., Rouppe van der Voort, L. H. M., van Noort, M., 2007, Evidence of Traveling Waves in Filament Threads, *Solar Phys.*, 246, 65–72
- Lin, Y., Martin, S. F., Engvold, O., 2008a, Filament Substructures and their Interrelation, in *Subsurface and Atmospheric Influences on Solar Activity*, (Eds.) R. Howe, R. W. Komm, K. S. Balasubramaniam, G. J. D. Petrie, vol. 383 of *Astronomical Society of the Pacific Conference Series*, p. 235
- Lin, Y., Martin, S. F., Engvold, O., Rouppe van der Voort, L. H. M., van Noort, M., 2008b, On small active region filaments, fibrils and surges, *Advances in Space Research*, 42, 803–811

- Lin, Y., Soler, R., Engvold, O., Ballester, J. L., Langangen, Ø., Oliver, R., Rouppe van der Voort, L. H. M., 2009, Swaying Threads of a Solar Filament, *ApJ*, 704, 870–876, 0909.2792
- Lites, B. W., Low, B. C., 1997, Flux Emergence and Prominences: a New Scenario for 3-DIMENSIONAL Field Geometry Based on Observations with the Advanced Stokes Polarimeter, *Solar Phys.*, 174, 91–98
- Litvinenko, Y. E., 1999, Photospheric Magnetic Reconnection and Canceling Magnetic Features on the Sun, *ApJ*, 515, 435–440
- Litvinenko, Y. E., 2000, On the Magnetic Field Orientation and Plasma Flows in Solar Filament Barbs, *Solar Phys.*, 196, 369–375
- Liu, J., Zhou, Z., Wang, Y., Liu, R., Wang, B., Liao, C., Shen, C., Zheng, H., Miao, B., Su, Z., Wang, S., 2012a, Slow Magnetoacoustic Waves Observed above a Quiet-Sun Region in a Dark Cavity, *ApJ*, 758, L26, 1209.3370
- Liu, R., Alexander, D., Gilbert, H. R., 2007, Kink-induced Catastrophe in a Coronal Eruption, *ApJ*, 661, 1260–1271
- Liu, R., Wang, H., Alexander, D., 2009, Implosion in a Coronal Eruption, *ApJ*, 696, 121–135
- Liu, W., Ofman, L., Nitta, N. V., Aschwanden, M. J., Schrijver, C. J., Title, A. M., Tarbell, T. D., 2012b, Quasi-periodic Fast-mode Wave Trains within a Global EUV Wave and Sequential Transverse Oscillations Detected by SDO/AIA, *ApJ*, 753, 52, 1204.5470
- Low, B. C., 1981, Eruptive solar magnetic fields, *ApJ*, 251, 352–363
- Low, B. C., 1982, Nonlinear force-free magnetic fields, *Reviews of Geophysics and Space Physics*, 20, 145–159
- Low, B. C., 1994, Magnetohydrodynamic processes in the solar corona: Flares, coronal mass ejections, and magnetic helicity, *Physics of Plasmas*, 1, 1684–1690
- Low, B. C., 1996, Solar Activity and the Corona, *Solar Phys.*, 167, 217–265
- Low, B. C., Hundhausen, J. R., 1995, Magnetostatic structures of the solar corona. 2: The magnetic topology of quiescent prominences, *ApJ*, 443, 818–836
- Low, B. C., Zhang, M., 2002, The Hydromagnetic Origin of the Two Dynamical Types of Solar Coronal Mass Ejections, *ApJ*, 564, L53–L56
- Low, B. C., Berger, T., Casini, R., Liu, W., 2012a, The Hydromagnetic Interior of a Solar Quiescent Prominence. I. Coupling between Force Balance and Steady Energy Transport, *ApJ*, 755, 34, 1203.1056
- Low, B. C., Liu, W., Berger, T., Casini, R., 2012b, The Hydromagnetic Interior of a Solar Quiescent Prominence. II. Magnetic Discontinuities and Cross-field Mass Transport, *ApJ*, 757, 21

- Lüst, R., Schlüter, A., 1954, Kraftfreie Magnetfelder. Mit 4 Textabbildungen, ZAp, 34, 263
- Mackay, D. H., 2005, Role of Large-scale Magnetic Fields and Material Flows in the Formation of Filaments and Filament Channels, in Large-scale Structures and their Role in Solar Activity, (Eds.) K. Sankarasubramanian, M. Penn, A. Pevtsov, vol. 346 of Astronomical Society of the Pacific Conference Series, p. 177
- Mackay, D. H., Gaizauskas, V., 2003, Helicity as a Component of Filament Formation, Solar Phys., 216, 121–142
- Mackay, D. H., van Ballegooijen, A. A., 2001, A Possible Solar Cycle Dependence to the Hemispheric Pattern of Filament Magnetic Fields?, ApJ, 560, 445–455
- Mackay, D. H., van Ballegooijen, A. A., 2006, Models of the Large-Scale Corona. II. Magnetic Connectivity and Open Flux Variation, ApJ, 642, 1193–1204
- Mackay, D. H., Gaizauskas, V., van Ballegooijen, A. A., 2000, Comparison of Theory and Observations of the Chirality of Filaments within a Dispersing Activity Complex, ApJ, 544, 1122–1134
- Mackay, D. H., Gaizauskas, V., Yeates, A. R., 2008a, Where Do Solar Filaments Form?: Consequences for Theoretical Models, Solar Phys., 248, 51
- Mackay, D. H., Gaizauskas, V., Yeates, A. R., 2008b, Where Do Solar Filaments Form?: Consequences for Theoretical Models, Solar Phys., 248, 51
- Mackay, D. H., Karpen, J. T., Ballester, J. L., Schmieder, B., Aulanier, G., 2010, Physics of Solar Prominences: II Magnetic Structure and Dynamics, Space Sci. Rev., 151, 333–399, 1001.1635
- Magara, T., 2006, Dynamic and Topological Features of Photospheric and Coronal Activities Produced by Flux Emergence in the Sun, ApJ, 653, 1499–1509
- Malherbe, J.-M., 1989, The formation of solar prominences, in Dynamics and Structure of Quiescent Solar Prominences, (Ed.) E. R. Priest, vol. 150 of Astrophysics and Space Science Library, pp. 115–141
- Manchester, IV, W., Gombosi, T., DeZeeuw, D., Fan, Y., 2004, Eruption of a Buoyantly Emerging Magnetic Flux Rope, ApJ, 610, 588–596
- Maricic, D., Vršnak, B., Stanger, A. L., Veronig, A., 2004, Coronal Mass Ejection of 15 May 2001: I. Evolution of Morphological Features of the Eruption, Solar Phys., 225, 337–353
- Mariska, J. T., 1992, The solar transition region, Cambridge Astrophysics Series, New York: Cambridge University Press, |c1992
- Martens, P. C., Zwaan, C., 2001, Origin and Evolution of Filament-Prominence Systems, ApJ, 558, 872–887

- Martin, S. F., 1973a, The Evolution of Prominences and Their Relationship to Active Centers (A Review), *Solar Phys.*, 31, 3–21
- Martin, S. F., 1973b, The Evolution of Prominences and Their Relationship to Active Centers (A Review), *Solar Phys.*, 31, 3–21
- Martin, S. F., 1998a, Conditions for the Formation and Maintenance of Filaments (Invited Review), *Solar Phys.*, 182, 107–137
- Martin, S. F., 1998b, Conditions for the Formation and Maintenance of Filaments (Invited Review), *Solar Phys.*, 182, 107
- Martin, S. F., 2003, Signs of helicity in solar prominences and related features, *Advances in Space Research*, 32, 1883–1893
- Martin, S. F., Marquette, W. H., Bilimoria, R., 1992, The Solar Cycle Pattern in the Direction of the Magnetic Field along the Long Axes of Polar Filaments, in *The Solar Cycle*, (Ed.) K. L. Harvey, vol. 27 of *Astronomical Society of the Pacific Conference Series*, p. 53
- Martin, S. F., Bilimoria, R., Tracadas, P. W., 1994, Magnetic field configurations basic to filament channels and filaments, in *Solar Surface Magnetism*, (Eds.) R. J. Rutten, C. J. Schrijver, p. 303
- Martres, M. J., Michard, R., Soru-Iscovici, 1966, Étude morphologique de la structure magnétique des régions actives en relation avec les phénomènes chromosphériques et les éruptions solaires. II. Localisation des plages brillantes, filaments et éruptions, *Annales d’Astrophysique*, 29, 249
- McAllister, A. H., Mackay, D. H., Martin, S. F., 2002, The Skew of High-Latitude X-ray Arcades in the Declining Phase of Cycle 22, *Solar Phys.*, 211, 155–163
- McIntosh, P. S., 1992, Solar Interior Processes Suggested by Large-Scale Surface Patterns, in *The Solar Cycle*, (Ed.) K. L. Harvey, vol. 27 of *Astronomical Society of the Pacific Conference Series*, p. 14
- McIntosh, P. S., Krieger, A. S., Nolte, J. T., Vaiana, G., 1976, Association of X-ray arches with chromospheric neutral lines, *Solar Phys.*, 49, 57–77
- McKenzie, D. E., Hudson, H. S., 1999, X-Ray Observations of Motions and Structure above a Solar Flare Arcade, *ApJ*, 519, L93–L96
- McTiernan, J. M., Fisher, G. H., Li, P., 1999, The Solar Flare Soft X-Ray Differential Emission Measure and the Neupert Effect at Different Temperatures, *ApJ*, 514, 472–483
- McWhirter, R. W. P., 1984, Report on the UK-SMM Workshop meetings held in Oxford in April 1983, September 1984 and March 1984, *Mem. Soc. Astron. Italiana*, 55, 823
- Minarovjech, M., Rybansky, M., Rusin, V., 1998a, Prominences and the Green Corona Over the Solar Activity Cycle, *Solar Phys.*, 177, 357–364



- Minarovjech, M., Rybansky, M., Rusin, V., 1998b, Prominences and the Green Corona Over the Solar Activity Cycle, *Solar Phys.*, 177, 357–364
- Mok, Y., Drake, J. F., Schnack, D. D., van Hoven, G., 1990, Prominence formation in a coronal loop, *ApJ*, 359, 228–231
- Mouradian, Z., Soru-Escout, I., 1994, A new analysis of the butterfly diagram for solar filaments., *A&A*, 290, 279–284
- Okamoto, T. J., Tsuneta, S., Lites, B. W., Kubo, M., Yokoyama, T., Berger, T. E., Ichimoto, K., Katsukawa, Y., Nagata, S., Shibata, K., Shimizu, T., Shine, R. A., Suematsu, Y., Tarbell, T. D., Title, A. M., 2009, Prominence Formation Associated with an Emerging Helical Flux Rope, *ApJ*, 697, 913–922, 0904.0007
- Panesar, N. K., Innes, D. E., Tiwari, S. K., Low, B. C., 2013, A solar tornado triggered by flares?, *A&A*, 549, A105, 1211.6569
- Panesar, N. K., Innes, D. E., Schmit, D. J., Tiwari, S. K., 2014a, On the Structure and Evolution of a Polar Crown Prominence/Filament System, *Solar Phys.*, 289, 1402.4989
- Panesar, N. K., Innes, D. E., Tiwari, S. K., Low, B. C., 2014b, A solar tornado caused by flares, in *IAU Symposium*, vol. 300 of *IAU Symposium*, pp. 235–238
- Parenti, S., Schmieder, B., Heinzel, P., Golub, L., 2012, On the Nature of Prominence Emission Observed by SDO/AIA, *ApJ*, 754, 66, 1205.5460
- Parker, E. N., 1955a, The Formation of Sunspots from the Solar Toroidal Field., *ApJ*, 121, 491
- Parker, E. N., 1955b, Hydromagnetic Dynamo Models., *ApJ*, 122, 293
- Parker, E. N., 1979a, Sunspots and the physics of magnetic flux tubes. I - The general nature of the sunspot. II - Aerodynamic drag, *ApJ*, 230, 905–923
- Parker, E. N., 1979b, Sunspots and the physics of magnetic flux tubes. II. Aerodynamic drag., *ApJ*, 230, 914–923
- Parker, E. N., 1979c, Cosmical magnetic fields: Their origin and their activity
- Patsourakos, S., Vial, J.-C., 2002, Soho Contribution to Prominence Science, *Solar Phys.*, 208, 253–281
- Pécseli, H., Engvold, O., 2000, Modeling of prominence threads in magnetic fields: Levitation by incompressible MHD waves, *Solar Phys.*, 194, 73–86
- Pesnell, W. D., Thompson, B. J., Chamberlin, P. C., 2012, The Solar Dynamics Observatory (SDO), *Solar Phys.*, 275, 3–15
- Pettit, E., 1919, Studies in prominence characteristics (abstract), *Popular Astronomy*, 27, 669

- Pettit, E., 1925, The forms and motions of the solar prominences, Publications of the Yerkes Observatory, 3, 4
- Pettit, E., 1932, Characteristic Features of Solar Prominences, ApJ, 76, 9
- Pettit, E., 1941, The Rotation of a Tornado Prominence, PASP, 53, 289
- Pettit, E., 1943, The Properties of Solar, Prominences as Related to Type., ApJ, 98, 6
- Pettit, E., 1946, Rotation of Tornado Prominences Determined by Dopler Effect, PASP, 58, 150
- Pettit, E., 1950, The Evidence for Tornado Prominences, PASP, 62, 144
- Phillips, K. J. H., 1992, Guide to the sun
- Pikel’Ner, S. B., 1971, Origin of Quiescent Prominences, Solar Phys., 17, 44–49
- Podgorski, W. A., Cheimets, P. N., Boerner, P., Glenn, P., 2009, SDO-AIA mirror performance, in Society of Photo-Optical Instrumentation Engineers (SPIE) Conference Series, vol. 7438 of Society of Photo-Optical Instrumentation Engineers (SPIE) Conference Series
- Priest, E. R., 1982, Solar magneto-hydrodynamics, Dordrecht, Holland ; Boston : D. Reidel Pub. Co. ; Hingham,
- Priest, E. R., Hood, A. W., Anzer, U., 1989, A twisted flux-tube model for solar prominences. I - General properties, ApJ, 344, 1010
- Priest, E. R., van Ballegooijen, A. A., Mackay, D. H., 1996, A Model for Dextral and Sinistral Prominences, ApJ, 460, 530
- Rachmeler, L. A., Gibson, S. E., Dove, J. B., DeVore, C. R., Fan, Y., 2013, Polarimetric Properties of Flux Ropes and Sheared Arcades in Coronal Prominence Cavities, Solar Phys., 1304.7594
- Rappazzo, A. F., Velli, M., Einaudi, G., 2013, Field Lines Twisting in a Noisy Corona: Implications for Energy Storage and Release, and Initiation of Solar Eruptions, ApJ, 771, 76, 1301.7678
- Régnier, S., Walsh, R. W., Alexander, C. E., 2011, A new look at a polar crown cavity as observed by SDO/AIA. Structure and dynamics, A&A, 533, L1, 1107.3451
- Saito, K., Tandberg-Hanssen, E., 1973, The Arch Systems, Cavities, and Prominences in the Helmet Streamer Observed at the Solar Eclipse, November 12, 1966, Solar Phys., 31, 105–121
- Scherrer, P. H., Bogart, R. S., Bush, R. I., Hoeksema, J. T., Kosovichev, A. G., Schou, J., Rosenberg, W., Springer, L., Tarbell, T. D., Title, A., Wolfson, C. J., Zayer, I., MDI Engineering Team, 1995, The Solar Oscillations Investigation - Michelson Doppler Imager, Solar Phys., 162, 129–188

- Scherrer, P. H., Amezcua, A., Bogart, R. S., 2010, Access to Solar Dynamics Observatory HMI and AIA Data via the Joint Science Operations Center (JSOC), AGU Fall Meeting Abstracts, p. C1867
- Scherrer, P. H., Schou, J., Bush, R. I., Kosovichev, A. G., Bogart, R. S., Hoeksema, J. T., Liu, Y., Duvall, T. L., Zhao, J., Title, A. M., Schrijver, C. J., Tarbell, T. D., Tomczyk, S., 2012, The Helioseismic and Magnetic Imager (HMI) Investigation for the Solar Dynamics Observatory (SDO), *Solar Phys.*, 275, 207–227
- Schmieder, B., Mein, N., Deng, Y., Dumitrache, C., Malherbe, J.-M., Staiger, J., Deluca, E. E., 2004, Magnetic changes observed in the formation of two filaments in a complex active region: TRACE and MSDP observations, *Solar Phys.*, 223, 119–141
- Schmieder, B., Chandra, R., Berlicki, A., Mein, P., 2010, Velocity vectors of a quiescent prominence observed by Hinode/SOT and the MSDP (Meudon), *A&A*, 514, A68
- Schmit, D. J., Gibson, S., 2013, Diagnosing the Prominence-Cavity Connection, *ApJ*, 770, 35, 1304.7595
- Schmit, D. J., Gibson, S. E., 2011, Forward Modeling Cavity Density: A Multi-instrument Diagnostic, *ApJ*, 733, 1
- Schou, J., Scherrer, P. H., Bush, R. I., Wachter, R., Couvidat, S., Rabello-Soares, M. C., Bogart, R. S., Hoeksema, J. T., Liu, Y., Duvall, T. L., Akin, D. J., Allard, B. A., Miles, J. W., Rairden, R., Shine, R. A., Tarbell, T. D., Title, A. M., Wolfson, C. J., Elmore, D. F., Norton, A. A., Tomczyk, S., 2012, Design and Ground Calibration of the Helioseismic and Magnetic Imager (HMI) Instrument on the Solar Dynamics Observatory (SDO), *Solar Phys.*, 275, 229–259
- Schwabe, M., 1844, Sonnenbeobachtungen im Jahre 1843. Von Herrn Hofrath Schwabe in Dessau, *Astronomische Nachrichten*, 21, 233
- Secchi, P. A., 1872, *Die Sonne*, 520, p.520
- Serio, S., Vaiana, G. S., Godoli, G., Motta, S., Pirronello, V., Zappala, R. A., 1978, Configuration and gradual dynamics of prominence-related X-ray coronal cavities, *Solar Phys.*, 59, 65–86
- Serio, S., Peres, G., Vaiana, G. S., Golub, L., Rosner, R., 1981, Closed coronal structures. II - Generalized hydrostatic model, *ApJ*, 243, 288–300
- Severny, A. B., 1950, , *The Observatory*, 73, 33–35
- Severny, A. B., Khoklova, V. L., 1953, , *The Observatory*, 10, 33–35
- Shibata, K., Tajima, T., Steinolfson, R. S., Matsumoto, R., 1989, Two-dimensional magnetohydrodynamic model of emerging magnetic flux in the solar atmosphere, *ApJ*, 345, 584–596

- Shimojo, M., Yokoyama, T., Asai, A., Nakajima, H., Shibasaki, K., 2006, One Solar-Cycle Observations of Prominence Activities Using the Nobeyama Radioheliograph 1992-2004, *PASJ*, 58, 85–92
- Simon, G. W., Leighton, R. B., 1964, Velocity Fields in the Solar Atmosphere. III. Large-Scale Motions, the Chromospheric Network, and Magnetic Fields., *ApJ*, 140, 1120
- Solanki, S. K., 2003, Sunspots: An overview, *A&A Rev.*, 11, 153–286
- Sterling, A. C., Moore, R. L., 2005, Slow-Rise and Fast-Rise Phases of an Erupting Solar Filament, and Flare Emission Onset, *ApJ*, 630, 1148–1159
- Su, Y., van Ballegoijen, A., 2012, Observations and Magnetic Field Modeling of a Solar Polar Crown Prominence, *ApJ*, 757, 168, 1208.1524
- Su, Y., van Ballegoijen, A., 2013, Rotating Motions and Modeling of the Erupting Solar Polar-crown Prominence on 2010 December 6, *ApJ*, 764, 91, 1211.6967
- Su, Y., Wang, T., Veronig, A., Temmer, M., Gan, W., 2012, Solar Magnetized "Tornadoes:" Relation to Filaments, *ApJ*, 756, L41, 1208.0138
- Su, Y. N., Golub, L., van Ballegoijen, A. A., Gros, M., 2006, Analysis of Magnetic Shear in An X17 Solar Flare on October 28, 2003, *Solar Phys.*, 236, 325–349
- Sun, X., Hoeksema, J. T., Liu, Y., Wiegmann, T., Hayashi, K., Chen, Q., Thalmann, J., 2012, Evolution of Magnetic Field and Energy in a Major Eruptive Active Region Based on SDO/HMI Observation, *ApJ*, 748, 77, 1201.3404
- Tandberg-Hanssen, E. (Ed.), 1995, The nature of solar prominences, vol. 199 of *Astrophysics and Space Science Library*
- Thomas, J. H., Weiss, N. O., 2008, *Sunspots and Starspots*, Cambridge University Press
- Thompson, W. T., 2009, 3D triangulation of a Sun-grazing comet, *Icarus*, 200, 351–357
- Tiwari, S. K., 2012, On the Force-free Nature of Photospheric Sunspot Magnetic Fields as Observed from Hinode (SOT/SP), *ApJ*, 744, 65, 1109.3156
- Tomczyk, S., Card, G. L., Darnell, T., Elmore, D. F., Lull, R., Nelson, P. G., Stander, K. V., Burkepile, J., Casini, R., Judge, P. G., 2008, An Instrument to Measure Coronal Emission Line Polarization, *Solar Phys.*, 247, 411–428
- Tripathi, D., Solanki, S. K., Mason, H. E., Webb, D. F., 2007, A bright coronal downflow seen in multi-wavelength observations: evidence of a bifurcating flux-rope?, *A&A*, 472, 633–642, 0802.3616
- Tripathi, D., Gibson, S. E., Qiu, J., Fletcher, L., Liu, R., Gilbert, H., Mason, H. E., 2009, Partially-erupting prominences: a comparison between observations and model-predicted observables, *A&A*, 498, 295–305, 0902.1228
- Vaiana, G. S., Krieger, A. S., Timothy, A. F., 1973, Identification and Analysis of Structures in the Corona from X-Ray Photography, *Solar Phys.*, 32, 81–116

- van Ballegooijen, A. A., 2004, Observations and Modeling of a Filament on the Sun, *ApJ*, 612, 519–529
- van Ballegooijen, A. A., Cranmer, S. R., 2010, Tangled Magnetic Fields in Solar Prominences, *ApJ*, 711, 164–178, 1001.2757
- van Ballegooijen, A. A., Martens, P. C. H., 1989, Formation and eruption of solar prominences, *ApJ*, 343, 971
- Vásquez, A. M., Frazin, R. A., Kamalabadi, F., 2009, 3D Temperatures and Densities of the Solar Corona via Multi-Spacecraft EUV Tomography: Analysis of Prominence Cavities, *Solar Phys.*, 256, 73–85
- Velli, M., Liewer, P., 1999, Alfvén Wave Generation in Photospheric Vortex Filaments, Macrospicules, and "Solar Tornadoes", *Space Science Reviews*, 87, 339–343
- Vrsnak, B., Maričić, D., Stanger, A. L., Veronig, A., 2004, Coronal Mass Ejection of 15 May 2001: II. Coupling of the Cme Acceleration and the Flare Energy Release, *Solar Phys.*, 225, 355–378
- Wachter, R., Schou, J., Rabello-Soares, M. C., Miles, J. W., Duvall, T. L., Bush, R. I., 2012, Image Quality of the Helioseismic and Magnetic Imager (HMI) Onboard the Solar Dynamics Observatory (SDO), *Solar Phys.*, 275, 261–284
- Waldmeier, M., 1957, Die polare Protuberanzenzone. Mit 2 Textabbildungen, *ZAp*, 42, 34
- Waldmeier, M., 1970, The Structure of the Monochromatic Corona in the Surroundings of Prominences, *Solar Phys.*, 15, 167–175
- Waldmeier, M., 1973, A Secondary Polar Zone of Solar Prominences, *Solar Phys.*, 28, 389–398
- Wang, H., Chae, J., Gurman, J. B., Kucera, T. A., 1998, Comparison of Prominences in  $H\alpha$  and He II 304 Å, *Solar Phys.*, 183, 91–96
- Wang, Y.-M., 1999, The Jetlike Nature of HE II  $\lambda$ 304 Prominences, *ApJ*, 520
- Wang, Y.-M., 2001, On the Relationship between He II  $\lambda$ 304 Prominences and the Photospheric Magnetic Field, *ApJ*, 560, 456
- Wang, Y.-M., Muglach, K., 2007, On the Formation of Filament Channels, *ApJ*, 666, 1284–1295
- Webb, D. F., 1998, CMEs and Prominences and Their Evolution over the Solar Cycle (Review), in *IAU Colloq. 167: New Perspectives on Solar Prominences*, (Eds.) D. F. Webb, B. Schmieder, D. M. Rust, vol. 150 of *Astronomical Society of the Pacific Conference Series*, p. 463
- Webb, D. F., Davis, J. M., McIntosh, P. S., 1984, Observations of the reappearance of polar coronal holes and the reversal of the polar magnetic field, *Solar Phys.*, 92, 109–132

- Wedemeyer-Böhm, S., Scullion, E., Steiner, O., Rouppe van der Voort, L., de La Cruz Rodriguez, J., Fedun, V., Erdélyi, R., 2012, Magnetic tornadoes as energy channels into the solar corona, *Nature*, 486, 505–508
- Wiegelmann, T., Sakurai, T., 2012, Solar Force-free Magnetic Fields, *Living Reviews in Solar Physics*, 9, 5, 1208.4693
- Winebarger, A. R., Warren, H., van Ballegooijen, A., DeLuca, E. E., Golub, L., 2002, Steady Flows Detected in Extreme-Ultraviolet Loops, *ApJ*, 567, L89–L92
- Woods, T. N., Hock, R., Eparvier, F., Jones, A. R., Chamberlin, P. C., Klimchuk, J. A., Didkovsky, L., Judge, D., Mariska, J., Warren, H., Schrijver, C. J., Webb, D. F., Bailey, S., Tobiska, W. K., 2011, New Solar Extreme-ultraviolet Irradiance Observations during Flares, *ApJ*, 739, 59
- Wuelser, J.-P., Lemen, J. R., Tarbell, T. D., Wolfson, C. J., Cannon, J. C., Carpenter, B. A., Duncan, D. W., Gradwohl, G. S., Meyer, S. B., Moore, A. S., Navarro, R. L., Pearson, J. D., Rossi, G. R., Springer, L. A., Howard, R. A., Moses, J. D., Newmark, J. S., Delaboudiniere, J.-P., Artzner, G. E., Auchere, F., Bougnet, M., Bouyries, P., Bridou, F., Clotaire, J.-Y., Colas, G., Delmotte, F., Jerome, A., Lamare, M., Mercier, R., Mullet, M., Ravet, M.-F., Song, X., Bothmer, V., Deutsch, W., 2004, EUVI: the STEREO-SECCHI extreme ultraviolet imager, in *Society of Photo-Optical Instrumentation Engineers (SPIE) Conference Series*, (Eds.) S. Fineschi, M. A. Gummin, vol. 5171 of *Society of Photo-Optical Instrumentation Engineers (SPIE) Conference Series*, pp. 111–122
- Wülser, J.-P., Lemen, J. R., Nitta, N., 2007, The STEREO SECCHI/EUVI EUV coronal imager, in *Society of Photo-Optical Instrumentation Engineers (SPIE) Conference Series*, vol. 6689 of *Society of Photo-Optical Instrumentation Engineers (SPIE) Conference Series*
- Yang, S. H., Zhang, J., Jin, C. L., Li, L. P., Duan, H. Y., 2009, Response of the solar atmosphere to magnetic field evolution in a coronal hole region, *A&A*, 501, 745–753, 0904.2684
- Zhang, M., Low, B. C., 2003, Magnetic Flux Emergence into the Solar Corona. III. The Role of Magnetic Helicity Conservation, *ApJ*, 584, 479–496
- Zhang, M., Low, B. C., 2005, The Hydromagnetic Nature of Solar Coronal Mass Ejections, *ARA&A*, 43, 103–137
- Zirin, H., 1966, *The solar atmosphere*
- Zirin, H., 1988, *Astrophysics of the sun*
- Zirker, J. B., 1989, Quiescent prominences, *Solar Phys.*, 119, 341–356
- Zirker, J. B., Cleveland, F. M., 1994, Searching for nanoflares, *Solar Phys.*, 153, 245–254
- Zirker, J. B., Martin, S. F., Harvey, K., Gaizauskas, V., 1997, Global Magnetic Patterns of Chirality, *Solar Phys.*, 175, 27–44

Zwaan, C., 1985, The emergence of magnetic flux, *Solar Phys.*, 100, 397–414

Zwaan, C., 1987, Elements and patterns in the solar magnetic field, *ARA&A*, 25, 83–111





# Publications

## Publications in refereed scientific journals

- **Panesar. N. K.**, Innes. D. E., Tiwari, S. K., and Low, B. C., 'A solar tornado triggered by flares?', 2013, A&A, vol 549A 105.P.
- **Panesar. N. K.**, Innes. D. E., Schmit. D. J., and Tiwari, S. K., 'On the structure and evolution of a polar crown prominence/filament system', 2014, Solar Phys., 289, DOI 10.1007/s11207-014-0504-z.

## Contributed papers in conference proceedings

- **Panesar. N. K.**, Innes. D. E., Tiwari, S. K., and Low, B. C., 'A solar tornado caused by flares', IAU S300, Nature of Prominences and their role in Space Weather, Proceedings of the International Astronomical Union, IAU Symposium, 2014, Volume 300, pp. 235-238



# Acknowledgements

First of all, I would like to express my heartily felt gratefulness to my supervisor, Dr. Davina Innes, for her guidance, encouragements and motivations throughout my PhD work. The scientific discussions with her, developed my knowledge on my research topic. I deeply appreciate her for correcting my manuscripts and thesis, which also improved my scientific writing. Without her support my PhD was not possible. I am sincerely thankful to Prof. Ansgar Reiners, for accepting me as a PhD student. His constructive and insightful comments really motivated me a lot during my work. I am also indebted to Prof. Sami Solanki for providing the working facilities at MPS. I am also grateful to other thesis committee members, Prof. Dr. Manfred Schüssler, Prof. Dr. Stefan Dreizler, Prof. Dr. Joerg Buechner, Prof. Dr. Ulrich R. Christensen, and Prof. Dr. Hardi Peter. Thanks to the computer center staff for helping me in technical problems.

I want to express my gratitude to Prof. B.C. Low for showing his interest in my work. His encouragements and useful discussions have been invaluable in the present work. Additionally, I would like to mention my special thanks to Prof. Darshan Singh, my M.Sc advisor at Punjabi University Patiala, for his kind support. I am extremely thankful to Dr. Sanjiv Tiwari, for fascinating scientific discussions, continuous inspirations and for reading my thesis chapters as well. I thank to my friend Dr. Anusha for her motivations, cheerful chats and for many delicious dinners, trips along with Sandeep. Thanks to Lucia for reading a chapter and for her good supportative company. Thanks to Jayant for fixing my IDL problems, sharing my thesis writing stress and for giving me such a good friendly company from the very beginning of my PhD. I also want to thank my friend Dr. Yeon Joo Lee for her care and cheerful chats. I am also thankful to Dr. Elena Kronberg for spending some nice time with me. Thanks to Nagaraju & family, Jisesh, Megha, and Bharti ji for nice friendly company. I am grateful to my all Indian and other friends at the MPS, as well as the institute's staff members who helped me directly and/or indirectly during my PhD. I am also grateful to the Faculty of Physics of the Georg-August-Universität Göttingen for all supports. I also like to express my warm thanks to Barbara for providing me such a nice, homely living environment and for loving me so much.

My special thanks goes to my sister-like friend Dr. Binita Pathak for her considerations and chats, and Sanjiv for his continuous support. Finally, my deepest gratitude goes to my loving mother, father and brother for their unconditional love, care and support. Without their support and encouragements, it was impossible for me to pursue my interests. My PhD thesis is dedicated to my family.



# Curriculum Vitae

## Personal Details

Name	Navdeep Kaur Panesar
Date of birth	27 September 1984
Place of birth	Ludhiana, India
Nationality	Indian

## Education

1990-2000	Akal Sahai Convent High School, Ludhiana, India
2000-2002	Govt. Girls High School, Ludhiana, India

## Higher Education

2002-2005	B.Sc. in Physics from Panjab University, Chandigarh, India
2005-2007	M.Sc. in Astronomy and Space Physics from Punjabi University, Patiala, India
2008-2009	PG diploma in Space and Atmospheric Sciences from Physical Research Laboratory, Ahmedabad, India
2011-2013	PhD student at the Universität für Göttingen, Germany Max-Planck-Institut für Sonnensystemforschung, Germany

In this dissertation, the structure, dynamics and evolution of two quiescent prominences were studied. Quiescent prominences are large structures and mainly associated with the quiet Sun region. For the analysis, the high spatial and temporal cadence data from the Solar Dynamic Observatory (SDO), and the Solar Terrestrial Relations Observatory (STEREO) were used. The observations from two different directions were combined and the prominence in 3D were studied. In the study of polar crown prominence, the prominence flows on limb were mainly investigated and its association with on-disk brightenings were found. The merging of diffused active region flux in the already formed chain of prominence caused the several brightenings in the filament channel and also injected the plasma upward with an average velocity of 15 km/s. In another study, the triggering mechanism of a quiescent tornado-like prominence was investigated. Flares from the neighboring active region triggered the tornado-like motions on the top of the prominence. Active region field contracts after the flare which results in the expansion of prominence cavity. The prominence helical magnetic field expands and plasma moves along the field lines which appear as a tornado-like activity. These observational investigations led to the understanding of structure and dynamics of quiescent prominences, which could be useful for theoretical prominence models.